UNIVERSITY OF CALIFORNIA, SAN DIEGO

Rapid 3D Bioprinting of Cardiac Tissue Models

A dissertation submitted in partial satisfaction of the
requirements for the degree Doctor of Philosophy

in

Materials Science and Engineering

by

Justin David Liu

Committee in charge:

Professor Shaochen Chen, Chair
Professor Adam Engler
Professor Andrew McCulloch
Professor Farah Sheikh
Professor Liangfang Zhang

2018

The Dissertation of Justin David Liu is approved, and it is acceptable in quality and form for publication on microfilm and electronically

Chair

University of California, San Diego

2018

DEDICATION

In recognition of their endless encouragement, love, and support, this dissertation is dedicated to Albert Liu, Theresa Liu, Angela Liu, and my wife Megan Barron.

EPIGRAPH

By three methods we may learn wisdom: First, by reflection, which is noblest; Second, by imitation, which is easiest; and third by experience, which is the bitterest.

Confucius

TABLE OF CONTENTS

LIST OF SUPPLEMENTAL FILES

Supplementary Video 1: Day 5 Line pattern on glass

Supplementary Video 2: Day 5 Slab pattern on glass

Supplementary Video 3: Day 10_1Hz_Seeded line pattern taken at 5x_scalebar=500µm

Supplementary Video 4: Day 10_1Hz_Seeded line pattern cardiac tissue bending cantilever-10x

Supplementary Video 5: Day 10_1hz_patterned cardiac tissue bending cantilever-10x

Supplementary Video 6: Day 10_1Hz_Slab pattern taken at 5x_scalebar=500µm

Supplementary Video 7: Day 10_1Hz_Line pattern taken at 5x_scalebar=500µm

Supplementary Video 8: Day 10_1Hz_Grid Pattern taken at 5x+scalebar=500µm

Supplementary Video 9: Day 10_1Hz Dispersion pattern taken at 5x_scalebar=500µm

Supplementary Video 10: Day10_1Hz_Random pattern taken at 5xx_scalebar=500µm

Supplementary Video 11: Day 7- hESC-CM in lines

Supplementary Video 12: Day 7- hESC-CM in slab

Supplementary video 13: DIC image of GCaMP-hESC-CM-across scaffold- Scale bar= 500 µm

Supplementary video 14: GCaMP-hESC-CM-across scaffold- Scale bar=500 µm

Supplementary video 15: Day 14_HUVEC-hESC-CM-thick tissue-scalebar=500µm

LIST OF FIGURES

LIST OF TABLES

ACKNOWLEDGEMENTS

I would like to acknowledge Dr. Shaochen Chen for his support as the chair of my committee. His guidance and encouragement have made this dissertation possible.

I would like to acknowledge the past and present members of the Chen lab, who have been a part of my journey and made me a better scientist.

Chapter 2, in part, is currently being prepared for submission for publication of the material. Liu J, Ma X, Dewan S, Lawrence N, Miller K Whang G, You S, Chung P, Chen S. Direct 3D BioPrinting of Cardiac Microtissues Mimicking Native Myocardium. The dissertation author was the primary investigator and primary author of this material.

Chapter 3, in part, is currently being prepared for submission for publication of the material. Liu J, Ma X, Dewan S, Lawrence N, Miller K Whang G, You S, Chung P, Chen S. Direct 3D BioPrinting of Cardiac Microtissues Mimicking Native Myocardium. The dissertation author was the primary investigator and primary author of this material.

Chapter 4, in part, contains material being prepared for submission for the publication of the material. Ma X, Liu J, Dewan S, Lawrence N, Miller K, Chen S. 3D Printed microcantilevers for human cardiac drug screening. The dissertation author was the secondary investigator and secondary author of this material. Chapter 4, in part, also is currently being prepared for submission for publication of the material. Liu J, Liu J, He J, Ma X, Chen Q, Lawrence N, Zhu W, Xu Y, Chen S. Rapid Printing of Human Cardiomyocytes in 3D Hydrogel. The dissertation author was the primary investigator and primary author of this material.

VITA

Education

University of California San Diego 2018
PhD, Materials Science and Engineering

University of California San Diego 2012
MS, Materials Science and Engineering

Northwestern University 2011
BS, Biomedical Engineering

Honors and Awards

Sustainable Power and Energy Center Graduate Summer Fellow Summer 2015
UCSD Materials Science and Engineering Fellowship 2012-2013

Publications

Zhu W., Pyo S.H., Wang P., You S., Yu C., Alido J., **Liu J.**, Leong Y., Chen S. "3D Printing of Bisphenol A-free Polycarbonates." ACS Applied Materials and Interfaces, 2018.

Huang Q., Lee J., Arce F.T., Yoon I., Angsantikul P., **Liu J**., Villanueva J., Thamphiwatana S., Ma X., Zhang L., Chen S.C., Lal R., and Sirbuly D. J., "Nanofiber optic force transducers with sub-piconewton resolution via near-field plasmon-dielectric interactions", Nature Photonics, 11, 352-355, 2017.

Zhu W., Qu X., Zhu J., Ma X., Patel S., **Liu J**., Wang P., Lai C. S., Gou M., Xu Y., Zhang K., Chen S.C. "Direct 3D bioprinting of prevascularized tissue constructs with complex microarchitecture", Biomaterials, Vol. 124, pp. 106-115, 2017.

Marin B.C., **Liu J**., Aklile E., Urbina A.D., Chiang A.S-C., Lawrence N., Chen S.C., Lipomi D.J., "SERS-Enhanced Piezoplasmonic Graphene Composite for Biological and Structural Strain Mapping", *Nanoscale,* Vol. 9, pp.1292-1298, 2017.

Liu J., Hwang H.H., Wang P., Whang G., Chen S. Direct 3D-printing of cell-laden constructs in microfluidic architectures. Lab on a Chip. 16, 1430-1438, 2016.

Ma X., Qu X., Zhu W., Li Y.S., Yi S., Zhang H., **Liu J.**, Ray P., Lai C.S., Zanella F., Feng S.G., Sheikh F., Chien S., Chen S. Deterministically patterned biomimetic human iPSC-derived hepatic model via rapid 3D bioprinting. PNAS. 113 (8). 2206–2211, 2016.

Hribar K., Meggs K., **Liu J.**, Zhu W., Xin Q., Chen S. Three-dimensional direct cell patterning in collagen hydrogels with near-infrared femtosecond laser. Scientific Reports. 5 (17203).1-7, 2015.

Huang T.H., Xin Q., **Liu J.**, Chen S. 3D printing of biomimetic microstructures for cancer cell migration. Biomed Microdevices. 16 (1) 127-132, 2014

ABSTRACT OF THE DISSERTATION

Rapid 3D Bioprinting of Cardiac Tissue Models

By

Justin David Liu

Doctor of Philosophy in Materials Science and Engineering

University of California, San Diego, 2018

Professor Shaochen Chen, Chair

Current drug discovery is impeded by insufficient models that do not accurately recapitulate physiological responses to treatment. Several drugs have recently been taken off the market due to a lack of efficacy or due to unexpected adverse effects, especially cardiovascular, that were not detected during clinical trials. Current models allow cardiomyocytes to self-assemble within cast gels or interact on 2D substrates with limited ability to recapitulate clinical responses to known drugs. In this study, I have utilized a 3D-printing technology named Micro-Continuous Optical Printing (μCOP) that can rapidly and spatially pattern neonatal ventricular mouse cardiomyocytes (NMVCMs)

within photocrosslinkable hydrogels. By embedding cardiomyocytes within a designated microarchitecture, cardiomyocytes preferentially aligned with the designed geometry and displayed phenotypic morphology and cytoskeletal alignment. With this 3D-printing system, I designed and printed an asymmetric mechanical testing platform sensitive enough to measure changes in force and calcium transients. I investigated how various complex microarchitectures may affect force production, exhibiting the potential to utilize this system to investigate future disease models. Finally, I adapted this system towards a humanized model, incorporating human embryonic stem cell cardiomyocytes (hESC-CMs) and human induced pluripotent stem cell-derived cardiomyocytes (hiPSC-CMs) in various platforms for *in vitro* and *in vivo* studies. The 3D-printed tissue constructs presented in this dissertation can ultimately be used for future drug discovery, disease modeling, and potentially to restore organ function.

Chapter 1: Introduction and Background

Abstract

Cardiovascular diseases are the foremost cause of death in the United States [1]. Roughly one billion U.S. dollars are spent researching and developing a new drug, only to fail clinical trials at rates as high as 80% for cardiovascular drugs [2]. Furthermore, some drugs may disproportionately benefit or harm certain genotypes, ethnicities, sexes, and ages, while clinical trials are not necessarily representative of possible users of the drug [3]. Cardiotoxicity is often evaluated in cell cultures missing the native 3D extracellular microenvironment, inducing non-physiological alignment and therefore compromising intercellular communication, profoundly confounding results. Consequently, cardiotoxicity is the primary reason for the retraction of pharmaceuticals from the market [1]. Hence there is significant need for predictive preclinical models, as well as a biomimetic platform for personalized drug screening. Furthermore, the goal of cardiac tissue engineers is to develop models that can help fully understand genetic, biologic, and pathophysiologic changes.

The physiology of the heart

The heart wall is comprised of three layers: the endocardium, myocardium and epicardium [4]. The myocardium is the main layer providing contractile strength during systole. Through the myocardium multiple layers are comprised of extracellular matrix (ECM) and aligned cells. Cardiomyocytes, the major contractile cell within the myocardium, account for 30% of the total number of cells within the myocardium [5]. Cardiomyocytes interact and align themselves with the topographic cues found within the

microarchitecture of the heart extracellular matrix is comprised various proteins like collagens, elastin, fibronectin and laminin. Aligned cardiomyocytes has also shown an improvement of synchronous beating due to improved action potential propagation [6] and contractile force[7]. Significant work has been done to pattern cardiomyocytes on 2D substrates offering high levels of alignment [6,8,9], however, in most cases, 3D engineered heart tissues either have high aspect ratios to allow cells to organize and align [10,11] across scaffolds uniaxially or be in disarray biaxially [12].

Cardiac cell source

Primary human adult cardiomyocytes are an ideal cell source, as most users of cardiac-specific pharmacological agents are adults; however, being terminally differentiated, acquiring these cells would necessitate the routine collection of biopsies of heart tissue from patients, without the potential for regeneration. Alternatively, neonatal mouse and rat cardiomyocytes have been a valuable source to develop *in vitro* models due to their relatively low cost to produce and maintain, their short gestation time, and genetic libraries already developed [13]. Other emerging cell sources are human embryonic stem cell-derived cardiomyocytes (ESC-CMs) [14] and adult human induced pluripotent stem cell-derived cardiomyocytes (iPSC-CMs) [15]. With fewer ethical considerations, human iPSC-CMs are more preferred in studying disease mechanisms and screen potential therapeutic drugs as they contain the unique genetics of the host. Examples of a specific disease that has been recapitulated is dilated cardiomyopathy iPSC-CMs carrying titin mutation displayed disorganized sarcomeres and abnormal calcium handling [16]. Other examples include Long QT syndrome [17]and hypertrophic

cardiomyopathy caused by *MHC7*[18]. Along with cardiomyocytes, there is also the potential to study the interaction of multiple cell types found within the heart, including neurons, fibroblasts, endothelial and smooth muscle cells. As the heart is highly organized to create a functioning cardiac tissue model, the precise control of cell location is required and enabling technologies must be explored.

Current 3D-printing technologies

The three main types of 3D bioprinting technologies include inkjet-based, extrusion-based, and light-assisted printing. Each of the 3D printing approaches has the capability to both print scaffolds for cell seeding and direct cell encapsulation within scaffolds. However, these platforms differ in various aspects including their printing mechanisms, resolution, and print speed. Inkjet-based bioprinting systems are modified from conventional desktop inkjet printers to dispense precise picoliter droplets of biomaterials or cell mixture onto a stage [19,20]. Thermal inkjet printing is more commonly used because of the relatively high cell viability after printing. For current inkjet-based bioprinters, resolutions can be as low as 20 μm [21]. Materials with relatively low viscosity are suitable to minimize the chance of clogging. This material consideration limits the size and rigidity of scaffolds produced using this method. Lower concentration of cells and materials are required which may not be physiologically relevant. Furthermore, slow printing speed and high shear can cause increased cell death, thus limiting the ability to print large, complex tissues.

Extrusion-based bioprinting systems use a continuous flow of biomaterials to produce larger scale tissues. A set of motors or magnetic rails with coordinates set by

computer-aided designs (CAD) position a nozzle or the stage in a specific location along with pressure or flow rates to dispense materials at a given moment. Typically materials are dispensed by pressure or mechanical (plunger or screw) means[22]. Pure biomaterial or cell-laden biomaterials can be printed onto a substrate in a layer-by-layer fashion. Extrusion-based printing benefits from improved materials selection, increased deposition speed, as well as upscaling printing footprint at the cost to resolution. The minimum printed feature resolution is generally over 100 μm. Similar to inkjet printing technology, extrusion-based printing also suffers from shear induced cell death [23,24].

Digital Light Projection bioprinting platforms utilize a digital micro-mirror device (DMD) chip and motorized stage controlled by a computer [25]. The DMD chip consists of around two million micro-mirrors, which allows for precise patterning of light as each micro-mirror can be turned on or off independently. The illumination of UV or other visible light sources of a pattern is reflected onto a pre-polymer solution only when the micro-mirror is turned on [26]. Two bioprinting systems, dynamic optical projection stereolithography (DOPsL) and microscale continuous printing (μCOP), emerged recently as DLP-based bioprinting platforms. DOPsL uses dynamic printing, with the ability of turning mirrors on and off during printing to alter mechanical properties and improve resolution while μCOP highlighting the continuous printing of complex 3D objects. The resolution of DLP-based printers is at the micron-scale, depending on the focal size of the light beam from each of the micro-mirrors. With DLP-based bioprinting, there is no artificial interface between droplets or extruded ribbons as with inkjet printing or extrusion-based printing. This is because an entire plane is projected onto the prepolymer solution all at once and the stage moves while the printing patterns are

continuously changed. While the material selection is confined within photopolymerizable materials, the limitation can be mitigated with the expanding library of photocurable materials or by mixing non-photopolymerizable materials with photopolymerizable materials making a hybrid system.

Two Photon Polymerization bioprinting (TPP) is a type of laser-based direct-writing technique developed from stereolithography, which generates structures by repeatedly and selectively photopolymerizing photo-sensitive monomers with a rastering laser [27]. The printing mechanism of TPP is based on the two-photon absorption phenomenon which allows for resolutions near 100 nm [28], making it ideal for printing nanoscale and microscale features. The tradeoff is footprint and printing speed. TPP typically uses ionic polymerization, limiting materials selection. TPP still provide advantages such as high cell viability and nanometer resolution [26]. However, to set up a TPP system, there is a higher barrier of entry in capital and expertise than the other printing methods.

Biomaterial selection

Biomaterials are widely used as a scaffolding material to develop cardiac tissues, and so must mimic the biochemical and mechanical properties of the native extracellular matrix. In the context of 3D bioprinting, a range of mechanisms have been employed to print both naturally-derived and synthetic hydrogel precursors. Regardless of the biomaterial selected, the biomaterials must be able to quickly form a hydrogel network during the printing process either through chemical or physical crosslinking mechanisms. In light-assisted 3D bioprinting, both fluid and viscous materials are compatible, thus

opening users to materials with a larger range of mechanical properties. However, these printing systems are limited to photocurable biomaterials, as previously mentioned which requires synthetic and natural biomaterials to be functionalized with photocrosslinkable groups such as poly (ethylene glycol-diacrylate) PEGDA, acrylate, or methacrylate, to name a few. In addition, the opacity of the chosen biomaterial is also an important consideration since this will impact the light penetration depth and subsequently effect the resolution and quality of the final structure [29].

Commonly employed natural biomaterials for cardiac tissue engineering include extracellular matrix proteins such as fibrin [30], collagen [31], gelatin [32], and decellularized cardiac matrix [33,34]. Synthetic options include polyacrylamide hydrogels, which allow for independent control of both mechanical and biochemical properties [35]. Acrylamide hydrogels have elastic moduli that can be tuned to mimic the elasticity of both healthy (10-15 kPa) [36] and diseased or infarcted myocardium (>50kPa) [37] and can be modified by the user's choice of extracellular matrix proteins [38] to decouple the effects of stiffness and adhesion sites. However, acrylamide monomers are cytotoxic, thus can only be utilized in 2D cell seeding studies.

Cardiac Tissue Engineering

Most work toward developing these drug discovery/screening platforms and physiological modeling has focused on recreating micro-tissues of the left ventricular myocardium, the site of the most severe cardiac pathologies. These micro-tissues are generally created by seeding cells atop or encapsulating cells within a patterned scaffold that mimics the extracellular matrix to directing and support tissue growth [39]. 2D

examples include precisely patterned topology and/or biochemical cues that can promote the growth of confluent, electrically coupled, and anisotropic tissue to match the structure and function of native myocardium [11,40,41].

The most common engineered cardiac tissue comes in two forms: heart tissue is a cantilever-based [10,42,43] or a thin film-based system creating cardiac patches[44–46]. Cantilever-based systems are usually made for designed to better mimic the myocardium *in vitro*. Usually, they are designed to improve maturity, increase force production, and to analyze drug response. Generally, they require self-organization of cardiac cells mixed with extracellular matrix. In some cases, electrical pacing [47,48] and mechanical stimulation have been used to further mature scaffolds. However, as these scaffolds self-align, the variability between the microstructure and cell-cell interaction create unique tissues every time. Cardiac patches designed with implantation in mind, focus on prevascularization prior to grafting to improve survivability and promote restoration of function of function post-injury [49–51]. However, cells tend to be mixed, or at best kept in separate layers before placing onto an injury. This does not generate a mimetic cardiac tissue and can lead to serious mismatch in conductivity between the graft and the host tissue. A potential solution to improving cell-cell and cell-material interaction, and engineering patches with cells in relative mimetic locations to each other is to use 3D printing.

Current State-of-the-Art 3D-Printed Cardiac Models

Several groups have been pursing 3D-printed cardiac models however, the research into these models are still in the early stages of development. Lind *et al.*

designed microarchitectures that guide the self-assembly of rat-derived cardiac tissues, with embedded noninvasive contractile stress sensors [52]. The system designed and produced via extrusion-based 3D printing with six functional bioinks based on highly conductive, piezoresistive, and biocompatible soft materials. This microphysiological device acquires contraction data due to changes of resistance during contraction, eliminating the need for dedicated microscopy setups. The engineered micro-tissue exhibited inotropic responses to isoproterenol and negative inotropic response to L-type calcium channel blocker, verapamil [52]. Another example of a drug testing platform was created by Zhang *et al.* whom also reported the use of a composite alginate/GelMA bioink mixed with endothelial cells [53]. An aligned, spontaneous, and synchronously contracting tissue was generated which demonstrated dose-dependent reduction in beating rate to doxorubicin [53].

TPP has also been utilized to fabricate filamentous scaffolds of synthetic [54] and natural polymers with micron-scale resolution [51]. Zhen et. al exposed a photoresist and produced 5 and 10 μm diameter filaments. Both healthy and diseased (Long QT syndrome) cardiomyocytes were seeded and observed, and their dose responses to various drugs including caffeine, nifedipine (calcium channel blocker), E4031(potassium channel blocker), and propranolol (beta-blocker) were recorded [54]. More recently, TTP was used produce 15 μm wide times 100 μm tall lines of GelMA hydrogels. The direct write was repeated producing a layer-by-layer scaffold. iPSC-CMs were seeded with endothelial and smooth muscle cells on fibronectin and collagen supported by the polymerized scaffold and were analyzed for calcium transients and conduction velocity across the entire scaffold. The samples were implanted on a myocardial infarction mouse

model, with 11% cell engraftment and significantly improved ejection fraction and fractional shortening at 4 weeks, demonstrating the potential of 3D-printed scaffolds with adult stem cell derived cardiomyocytes to recover cardiac function [51].

As it stands, 3D printing of cardiac tissue is still limited and there is great promise in developing new models to better assess tissue function and disease progression. In this dissertation I will focus on the optimization and utilization of a μCOP system to print naturally-derived gelatin-based hydrogels and focus on direct print of neonatal mouse ventricular cardiomyocytes (NMVCMs) within these hydrogels. Secondly, I will focus on the design and fabrication of a 3D-printed scaffold to measure the forces produced by aligned cardiac tissue. Furthermore, I will look at how complex 3D patterns can alter contraction of direct-print cardiac tissues. Lastly, I will translate the developed 3D-scaffold towards a humanized model, along with designing other 3D-printed models for higher-throughput drug screening, and *in vivo* studies. The work in this dissertation could lead the groundwork to the development of future disease and drug screening models, along with lead to insights in better graft integration by spatially patterning multiple cell types to support functional cardiac tissue.

References:

[1] D. Mozaffarian, E.J. Benjamin, A.S. Go, D.K. Arnett, M.J. Blaha, M. Cushman, S. de Ferranti, J.-P. Després, H.J. Fullerton, V.J. Howard, M.D. Huffman, S.E. Judd, B.M. Kissela, D.T. Lackland, J.H. Lichtman, L.D. Lisabeth, S. Liu, R.H. Mackey, D.B. Matchar, D.K. McGuire, E.R. Mohler, C.S. Moy, P. Muntner, M.E. Mussolino, K. Nasir, R.W. Neumar, G. Nichol, L. Palaniappan, D.K. Pandey, M.J. Reeves, C.J. Rodriguez, P.D. Sorlie, J. Stein, A. Towfighi, T.N. Turan, S.S. Virani, J.Z. Willey, D. Woo, R.W. Yeh, M.B. Turner, American Heart Association Statistics Committee and Stroke Statistics Subcommittee, Heart disease and stroke statistics--2015 update: a report from the American Heart Association., Circulation. 131 (2015) e29-322.

[2] A.A. Ciociola, L.B. Cohen, P. Kulkarni, the F.-R.M.C. of the A.C. of Gastroenterology, How drugs are developed and approved by the FDA: current process and future directions, Am J Gastroenterol. 109 (2014) 620–623.

[3] J. Ribas, H. Sadeghi, A. Manbachi, J. Leijten, K. Brinegar, Y.S. Zhang, L. Ferreira, A. Khademhosseini, Cardiovascular organ-on-a-chip platforms for drug discovery and development, Appl. Vitr. Toxicol. 2 (2016) 82–96.

[4] ed. Lilly, Leonard S., Pathophysiology of Heart Disease: A Collaborative Project of Medical Students and Faculty., Wolters Kluwer/Lippincott Williams & Wilkins, 2011.

[5] M. Mollova, K. Bersell, S. Walsh, J. Savla, L.T. Das, S.-Y. Park, L.E. Silberstein, C.G. Dos Remedios, D. Graham, S. Colan, B. Kühn, Cardiomyocyte proliferation contributes to heart growth in young humans., Proc. Natl. Acad. Sci. U. S. A. 110 (2013) 1446–51.

[6] D.-H. Kim, E.A. Lipke, P. Kim, R. Cheong, S. Thompson, M. Delannoy, K.-Y. Suh, L. Tung, A. Levchenko, Nanoscale cues regulate the structure and function of macroscopic cardiac tissue constructs, Proc. Natl. Acad. Sci. 107 (2010) 565–570.

[7] A.W. Feinberg, P.W. Alford, H. Jin, C.M. Ripplinger, A.A. Werdich, S.P. Sheehy, A. Grosberg, K.K. Parker, Controlling the contractile strength of engineered cardiac muscle by hierarchal tissue architecture, Biomaterials. 33 (2012) 5732–5741.

[8] A. Atmanli, I.J. Domian, Generation of aligned functional myocardial tissue through microcontact printing., J. Vis. Exp. (2013) e50288.

[9] A. Agarwal, Y. Farouz, A.P. Nesmith, L.F. Deravi, M.L. McCain, K.K. Parker, Micropatterning Alginate Substrates for In Vitro Cardiovascular Muscle on a Chip, Adv. Funct. Mater. 23 (2013) 3738–3746.

[10] M.N. Hirt, J. Boeddinghaus, A. Mitchell, S. Schaaf, C. Börnchen, C. Müller, H. Schulz, N. Hubner, J. Stenzig, A. Stoehr, C. Neuber, A. Eder, P.K. Luther, A. Hansen, T. Eschenhagen, Functional improvement and maturation of rat and human engineered heart tissue by chronic electrical stimulation, J. Mol. Cell. Cardiol. 74 (2014) 151–161.

[11] A. Grosberg, P.W. Alford, M.L. McCain, K.K. Parker, Ensembles of engineered cardiac tissues for physiological and pharmacological study: Heart on a chip, Lab Chip. 11 (2011) 4165.

[12] A.C.C. van Spreeuwel, N.A.M. Bax, A.J. Bastiaens, J. Foolen, S. Loerakker, M. Borochin, D.W.J. van der Schaft, C.S. Chen, F.P.T. Baaijens, C.V.C. Bouten, The

influence of matrix (an)isotropy on cardiomyocyte contraction in engineered cardiac microtissues, Integr. Biol. 6 (2014) 422–429.

[13] N. Milani-Nejad, P.M.L. Janssen, Small and Large Animal Models in Cardiac Contraction Research: Advantages and Disadvantages, (n.d.).

[14] H. Song, S.K. Chung, Y. Xu, Modeling Disease in Human ESCs Using an Efficient BAC-Based Homologous Recombination System, Cell Stem Cell. 6 (2010) 80–89.

[15] S.D. Lundy, J.A. Gantz, C.M. Pagan, D. Filice, M.A. Laflamme, Pluripotent stem cell derived cardiomyocytes for cardiac repair, Curr. Treat. Options Cardiovasc. Med. 16 (2014) 319.

[16] J.T. Hinson, A. Chopra, N. Nafissi, W.J. Polacheck, C.C. Benson, S. Swist, J. Gorham, L. Yang, S. Schafer, C.C. Sheng, A. Haghighi, J. Homsy, N. Hubner, G. Church, S.A. Cook, W.A. Linke, C.S. Chen, J.G. Seidman, C.E. Seidman, Titin mutations in iPS cells define sarcomere insufficiency as a cause of dilated cardiomyopathy, Science (80-.). 349 (2015) 982–986.

[17] K. Sallam, Y. Li, P.T. Sager, S.R. Houser, J.C. Wu, Finding the rhythm of sudden cardiac death: new opportunities using induced pluripotent stem cell-derived cardiomyocytes., Circ. Res. 116 (2015) 1989–2004.

[18] F. Lan, A.S. Lee, P. Liang, V. Sanchez-Freire, P.K. Nguyen, L. Wang, L. Han, M. Yen, Y. Wang, N. Sun, O.J. Abilez, S. Hu, A.D. Ebert, E.G. Navarrete, C.S. Simmons, M. Wheeler, B. Pruitt, R. Lewis, Y. Yamaguchi, E.A. Ashley, D.M. Bers, R.C. Robbins, M.T. Longaker, J.C. Wu, Abnormal calcium handling properties underlie familial hypertrophic cardiomyopathy pathology in patient-specific induced pluripotent stem cells., Cell Stem Cell. 12 (2013) 101–13.

[19] K. Hölzl, S. Lin, L. Tytgat, S. Van Vlierberghe, L. Gu, A. Ovsianikov, Bioink properties before, during and after 3D bioprinting, Biofabrication. 8 (2016) 32002.

[20] R.F. Pereira, P.J. Bártolo, 3D bioprinting of photocrosslinkable hydrogel constructs, J. Appl. Polym. Sci. 132 (2015).

[21] H.-W. Kang, S.J. Lee, I.K. Ko, C. Kengla, J.J. Yoo, A. Atala, A 3D bioprinting system to produce human-scale tissue constructs with structural integrity, Nat. Biotechnol. 34 (2016) 312–319.

[22] S. V Murphy, A. Atala, 3D bioprinting of tissues and organs., Nat. Biotechnol. 32 (2014) 773–785.

[23] F. You, B.F. Eames, X. Chen, Application of extrusion-based hydrogel bioprinting for cartilage tissue engineering, Int. J. Mol. Sci. 18 (2017) 1597.

[24] I.T. Ozbolat, M. Hospodiuk, Current advances and future perspectives in extrusion-based bioprinting, Biomaterials. 76 (2016) 321–343.

[25] K.C. Hribar, P. Soman, J. Warner, P. Chung, S. Chen, Light-assisted direct-write of 3D functional biomaterials, Lab Chip. 14 (2014) 268–275.

[26] W. Zhu, X. Ma, M. Gou, D. Mei, K. Zhang, S. Chen, 3D printing of functional biomaterials for tissue engineering, Curr. Opin. Biotechnol. 40 (2016) 103–112.

[27] B.H. Cumpston, S.P. Ananthavel, S. Barlow, D.L. Dyer, J.E. Ehrlich, L.L. Erskine, A.A. Heikal, S.M. Kuebler, I.-Y.S. Lee, D. McCord-Maughon, J. Qin, H. Röckel, M. Rumi, X.-L. Wu, S.R. Marder, J.W. Perry, Two-photon polymerization initiators for three-dimensional optical data storage and microfabrication, Nature. 398 (1999) 51–54.

[28] R.L. Truby, J.A. Lewis, Printing soft matter in three dimensions, Nature. 540 (2016) 371–378.

[29] W. Zhu, J. Li, Y.J. Leong, I. Rozen, X. Qu, R. Dong, Z. Wu, W. Gao, P.H. Chung, J. Wang, S. Chen, 3D-Printed Artificial Microfish, Adv. Mater. 27 (2015) 4411–4417.

[30] K.Y. Ye, K.E. Sullivan, L.D. Black, Encapsulation of cardiomyocytes in a fibrin hydrogel for cardiac tissue engineering, J. Vis. Exp. (2011) 3251.

[31] W.R. Legant, A. Pathak, M.T. Yang, V.S. Deshpande, R.M. McMeeking, C.S. Chen, Microfabricated tissue gauges to measure and manipulate forces from 3D microtissues, Proc. Natl. Acad. Sci. 106 (2009) 10097–10102.

[32] M.L. McCain, A. Agarwal, H.W. Nesmith, A.P. Nesmith, K.K. Parker, Micromolded gelatin hydrogels for extended culture of engineered cardiac tissues, Biomaterials. 35 (2014) 5462–5471.

[33] J.M. Singelyn, J.A. DeQuach, S.B. Seif-Naraghi, R.B. Littlefield, P.J. Schup-Magoffin, K.L. Christman, Naturally derived myocardial matrix as an injectable scaffold for cardiac tissue engineering, Biomaterials. 30 (2009) 5409–5416.

[34] F. Pati, J. Jang, D.-H. Ha, S. Won Kim, J.-W. Rhie, J.-H. Shim, D.-H. Kim, D.-W. Cho, Printing three-dimensional tissue analogues with decellularized extracellular matrix bioink, Nat. Commun. 5 (2014) 3935.

[35] V. Gribova, T. Crouzier, C. Picart, A material's point of view on recent developments of polymeric biomaterials: control of mechanical and biochemical properties, J. Mater. Chem. 21 (2011) 14354–14366.

[36] A.J.S. Ribeiro, Y.-S. Ang, J.-D. Fu, R.N. Rivas, T.M.A. Mohamed, G.C. Higgs, D. Srivastava, B.L. Pruitt, Contractility of single cardiomyocytes differentiated from pluripotent stem cells depends on physiological shape and substrate stiffness, Proc.

Natl. Acad. Sci. 112 (2015) 12705–12710.

[37] A.J. Engler, C. Carag-Krieger, C.P. Johnson, M. Raab, H.-Y. Tang, D.W. Speicher, J.W. Sanger, J.M. Sanger, D.E. Discher, Embryonic cardiomyocytes beat best on a matrix with heart-like elasticity: scar-like rigidity inhibits beating, J. Cell Sci. 121 (2008) 3794–3802.

[38] R. Chaudhuri, M. Ramachandran, P. Moharil, M. Harumalani, A.K. Jaiswal, Biomaterials and cells for cardiac tissue engineering: Current choices, Mater. Sci. Eng. C. 79 (2017) 950–957.

[39] M.N. Hirt, A. Hansen, T. Eschenhagen, Cardiac tissue engineering : State of the art, Circ. Res. 114 (2014) 354–367.

[40] C. Rao, T. Prodromakis, L. Kolker, U.A.R. Chaudhry, T. Trantidou, A. Sridhar, C. Weekes, P. Camelliti, S.E. Harding, A. Darzi, M.H. Yacoub, T. Athanasiou, C.M. Terracciano, The effect of microgrooved culture substrates on calcium cycling of cardiac myocytes derived from human induced pluripotent stem cells, Biomaterials. 34 (2013) 2399–2411.

[41] M.R. Salick, B.N. Napiwocki, J. Sha, G.T. Knight, S.A. Chindhy, T.J. Kamp, R.S. Ashton, W.C. Crone, Micropattern Width Dependent Sarcomere Development in Human ESC-Derived Cardiomyocytes, Biomaterials. 35 (2014) 4454–4464.

[42] T. Boudou, W.R. Legant, A. Mu, M.A. Borochin, N. Thavandiran, M. Radisic, P.W. Zandstra, J.A. Epstein, K.B. Margulies, C.S. Chen, A Microfabricated Platform to Measure and Manipulate the Mechanics of Engineered Cardiac Microtissues, Tissue Eng. Part A. 18 (2012) 910–919.

[43] A. Grosberg, A.P. Nesmith, J.A. Goss, M.D. Brigham, M.L. McCain, K.K. Parker, Muscle on a chip: In vitro contractility assays for smooth and striated muscle, J. Pharmacol. Toxicol. Methods. 65 (2012) 126–135.

[44] S. Pok, O.M. Benavides, P. Hallal, J.G. Jacot, Use of Myocardial Matrix in a Chitosan-Based Full-Thickness Heart Patch, Tissue Eng. Part A. 20 (2014) 1877–1887.

[45] J. Jang, H.J. Park, S.W. Kim, H. Kim, J.Y. Park, S.J. Na, H.J. Kim, M.N. Park, S.H. Choi, S.H. Park, S.W. Kim, S.M. Kwon, P.J. Kim, D.W. Cho, 3D printed complex tissue construct using stem cell-laden decellularized extracellular matrix bioinks for cardiac repair, Biomaterials. 112 (2017) 264–274.

[46] D. Zhang, I.Y. Shadrin, J. Lam, H.-Q. Xian, H.R. Snodgrass, N. Bursac, Tissue-engineered cardiac patch for advanced functional maturation of human ESC-derived cardiomyocytes., Biomaterials. 34 (2013) 5813–20.

[47] S.S. Nunes, J.W. Miklas, J. Liu, R. Aschar-Sobbi, Y. Xiao, B. Zhang, J. Jiang, S. Massé, M. Gagliardi, A. Hsieh, N. Thavandiran, M.A. Laflamme, K. Nanthakumar, G.J. Gross, P.H. Backx, G. Keller, M. Radisic, Biowire: a platform for maturation of human pluripotent stem cell–derived cardiomyocytes, Nat. Methods. 10 (2013) 781–787.

[48] N. Tandon, C. Cannizzaro, P.-H.G. Chao, R. Maidhof, A. Marsano, H. Ting, H. Au, M. Radisic, G. Vunjak-Novakovic, Electrical stimulation systems for cardiac tissue engineering, (n.d.).

[49] Q. Xiong, K.L. Hill, Q. Li, P. Suntharalingam, A. Mansoor, X. Wang, M.N. Jameel, P. Zhang, C. Swingen, D.S. Kaufman, J. Zhang, A fibrin patch-based enhanced delivery of human embryonic stem cell-derived vascular cell transplantation in a porcine model of postinfarction left ventricular remodeling., Stem Cells. 29 (2011) 367–75.

[50] H. Masumoto, T. Ikuno, M. Takeda, H. Fukushima, A. Marui, S. Katayama, T. Shimizu, T. Ikeda, T. Okano, R. Sakata, J.K. Yamashita, Human iPS cell-engineered cardiac tissue sheets with cardiomyocytes and vascular cells for cardiac regeneration, Sci. Rep. 4 (2014).

[51] L. Gao, M.E. Kupfer, J.P. Jung, L. Yang, P. Zhang, Y. Da Sie, Q. Tran, V. Ajeti, B.T. Freeman, V.G. Fast, P.J. Campagnola, B.M. Ogle, J. Zhang, Myocardial tissue engineering with cells derived from human-induced pluripotent stem cells and a native-like, high-resolution, 3-dimensionally printed scaffold, Circ. Res. 120 (2017) 1318–1325.

[52] J.U. Lind, T.A. Busbee, A.D. Valentine, F.S. Pasqualini, H. Yuan, M. Yadid, S. Park, A. Kotikian, A.P. Nesmith, P.H. Campbell, J.J. Vlassak, J.A. Lewis, K.K. Parker, Instrumented cardiac microphysiological devices via multimaterial three-dimensional printing., Nat. Mater. 16 (2016) 303–308.

[53] Y.S. Zhang, A. Arneri, S. Bersini, S.R. Shin, K. Zhu, Z. Goli-Malekabadi, J. Aleman, C. Colosi, F. Busignani, V. Dell'Erba, C. Bishop, T. Shupe, D. Demarchi, M. Moretti, M. Rasponi, M.R. Dokmeci, A. Atala, A. Khademhosseini, Bioprinting 3D microfibrous scaffolds for engineering endothelialized myocardium and heart-on-a-chip, Biomaterials. 110 (2016) 45–59.

[54] Z. Ma, S. Koo, M.A. Finnegan, P. Loskill, N. Huebsch, N.C. Marks, B.R. Conklin, C.P. Grigoropoulos, K.E. Healy, Three-dimensional filamentous human diseased cardiac tissue model, Biomaterials. 35 (2014) 1367–1377.

Chapter 2: Fabrication of a 3D tissue analog using cell-laden photocrosslinkable hydrogels

Abstract

Engineering physiologically relevant three-dimensional (3D) tissues remains a major challenge. Cellular alignment in 3D can be achieved by controlling scaffold microstructure and by physically encapsulating cells near these geometric cues (see Chapter 1). Here we present a novel method of cell encapsulation in 3D-printed methacrylated gelatin (GelMA) scaffolds patterned via Micro-Continuous Optical Printing (μCOP) to induce aligned cardiac tissue. Using this method, printing parameters for acellular scaffolds were optimized including exposure time, photoinitiator concentration, GelMA concentration, and pattern dimensions to maximize viability and function. Neonatal mouse ventricular cardiomyocytes were successfully encapsulated within a user-defined pattern, preferentially aligning to the designated geometry and displaying a rod-like morphology. Additionally, this preferential alignment increases cell contractility and construct deformation parallel to the patterned axis when compared to an unpatterned geometry. Thus, the presented system may be used to produce a 3D physiologically relevant *in vitro* test model of organized cardiac tissue with great potential for use in drug screening and cardiac disease models.

Introduction

Previously, tissue engineering approaches have attempted to recapitulate native microstructures *in vitro* utilizing traditional microfabrication techniques designing micro-

to-nano-sized features such as grooves, printed biochemical cues, or aligned nanofibers and then seeding cardiomyocytes onto these substrates[6,8,55,56]. This approach results in substantial control of alignment of cardiomyocytes since cells align along cues produced by topographical patterning. Nonetheless, surface patterns or grooves are limited to inducing cellular alignment in 2D and do not adequately recapitulate the native architecture of the heart [57].

Microcontinous optical printing (μCOP) is an emerging technology developed by Dr. Shaochen Chen. The μCOP system uses a digital micromirror device (DMD), a digital light projecting system of two million mirrors that has an arbitrary on or off state. When turned on using a digital pattern, only light hitting those mirrors is reflected from an ultraviolet (365 nm) light source, through a set of focusing optics, to increase the resolution of the desired pattern. Immediately after the print starts, the stage moves the sample and the system pairs the movement of the stage to changes in the mask[58–61]. As the light hits the prepolymer solution, photoinitiators within the solution initiate crosslinking of acrylated biomaterials. Since the μCOP system pairs very well with aqueous solution, cells can easily be incorporated within the prepolymer solution prior to printing in order to encapsulate and spatially pattern cells. [59,62]

Previous work has focused on the encapsulation of stem cells, endothelial, and hepatocytes using this system [59,63,64]. In this chapter, I describe the use of the μCOP system along with the scaffold design considerations, printing parameters, and solution considerations required for encapsulation of 10T1/2 mouse mesenchymal stem cells for preliminary studies and the encapsulation of neonatal mouse ventricular cardiomyocytes

(NMVCMs). Along with basic characterization, like cell viability, cellular alignment and cell displacement during contraction was assessed.

Results

Pattern Design using μCOP

The μCOP system uses a DMD which is controlled by a set of digital patterns produced by converting Portable Network Graphics (PNG) or bitmap (BMP) files into 1's and 0's to control the on and off state of the mirror. By designating a pattern with grayscale (0-255) values or specific red, green, or blue (RGB, 0-255, 0-255, 0-255) and converting it to the data file using a lab-based MATLAB script, I can designate when any of the mirrors can be turned on or off with respect to the stage position. Projection stereolithography (PSL) and μCOP use a UV light source, a digital micromirror device, a set of projection optics and a stage (Figure 1a). In the case of PSL (Figure 1b), a set of three masks are created and uploaded. The user illuminates one pattern at a time, moving the stage, and replacing the solution after each subsequent print. One consideration of this printing method is that with each print, the solution should be flushed with sufficient new prepolymer solution, or rinsed and solution replaced, as some prepolymer solution may form oligomers, however not fully polymerized to precipitate and form a solid object. Figure 1c, shows how μCOP only needs a single design, where I can designate the grayscale value to be on=1 or off=0. In this example, each color is explicitly denoted: 230 (light gray) =1 0 0; 115 (medium gray)= 1 1 0; 0 (black) = 1 1 1. This is then translated to a 3D matrix, with each number corresponding to a spatial position on the DMD:

First layer: $\begin{bmatrix} 1 & 1 & 1 \\ 1 & 1 & 1 \end{bmatrix}$ Second layer: $\begin{bmatrix} 1 & 1 & 0 \\ 1 & 0 & 0 \end{bmatrix}$ Third Layer: $\begin{bmatrix} 1 & 0 & 0 \\ 0 & 0 & 0 \end{bmatrix}$

where the stage moves continuously at a set velocity to change each pattern at a specific z-position.

Similarly, an RGB image may be used to assign each color (figure 2a). In this example a single image was used to produce two digital complementary patterns of either checkerboard, concentric circles, hexagons and hexagonal perimeters, or parallel lines. In this example, a solution of 20% Poly(ethelyne glycol) Diacrylate (PEGDA)/0.2% LAP/0.01% fluorescein isothiocyanate (FITC,) was exposed to the first pattern. A fluorescent image of the first pattern is shown in figure 2b. Afterwards, the remaining prepolymer solution is flushed with Dulbecco's Phosphate-Buffered Saline (DPBS) and replaced with 20% PEGDA/0.2% LAP/0.01% tetramethylrhodamine (TRITC) and the subsequent pattern was exposed (figure 2c).

Effect of GelMA and LAP concentration on exposure time.

Several concentrations of GelMA: 5, 7.5, 10, and 15% (wt/vol) with 0.2% LAP was exposed with a test pattern (figure 3a) consisting of either checkerboard, circles, parallel or 45^{o} lines. This test pattern is especially difficult to print as there are several features at various scales, and thus there are many potential uses, including determining the focal plane if alterations are made to the μCOP system and aiding in optimizing exposure times based on feature size, location, and complexity. Samples were printed and evaluated and designated as optimized per concentration based off these criteria: at least three quarters of the line patterns being resolved from the center, all five circle printed, the edges of the smallest square exist and the 45^{o} lines have little to no sinusoidal shape.

A representative brightfield image is shown in figure 3b. When altering GelMA concentration exposure time, τ, show a power law dependence (figure 3c):

$$\tau \propto \left(\frac{C}{100}\right)^{-1.3} \tag{2.1}$$

where C is concentration. Similarly, changes in exposure time by increasing initiator, I, follows a power law dependence (figure 3d):

$$\tau \propto \left(\frac{I}{100}\right)^{-0.5} \tag{2.2}$$

Effect of GelMA concentration on compressive modulus

To compare the mechanical properties of the different GelMA concentrations, 2 mm tall by 1 mm samples were printed and allowed to incubate for 24 hours before mechanical testing commenced. GelMA cylinders ranging from 5%, 7.5%, 10%, and 15% were compressed using a CellScale Microsquisher. The compressive modulus ranged from 1.14 ± 0.08 kPa for 5% GelMA, 4.71 ± 0.14 kPa for 7.5% GelMA, 13.1 ± 0.71 kPa for 10% GelMA, and finally 44.6 ± 2.41 kPa for 15% GelMa cylinders (figure 3d, SEM, n=6).

Pattern proximity and pattern footprint alter printing parameters

Along with optimizing exposure time based on material composition, exposure time must also be optimized based off pattern geometry. To illustrate this effect, a set of parallel lines based on pixel dimensions of 10, 20, 40, 80, and 160 pixels wide were designed in Photoshop™ and drawn with increased spacing to reduce crosstalk between lines when exposing the solution. A printing parameter commonly used to determine the quality of the print is μm to pixel ratio. 7.5% GelMA/0.2% LAP lines were printed using

0.2 mg/mL FITC dextran. 10, 20, and 40 pixel samples were exposed for 16 seconds; however, 80 and 160 pixel samples had to be measured with 12 second exposures. The average μm per pixel ratio was measured to be 6.3± 0.2, 7.6 ± 0.2, 5.1 ± 0.01, 5± 0.04, and 4.9 ± 0.07 μm per pixel (SEM, n=3) for 10, 20, 40, 80, and 160 pixel lines, respectively (figure 4b). Increasing the time would over-polymerize the sample and cause the sample to tear when trying to remove the sample from the PDMS layer. Similarly, a set of 10 pixel wide lines were drawn, increasing the interline distance from 5, 10, and 50 pixels were printed using μCOP, exposing each sample for 16 seconds. The μm to pixel ratio were 3.88 ± 0.01, 4.62 ± 0.23, and 6.3± 0.2 (SEM, n=3) for 5, 10, and 50 pixel spacings, respectively (Figure 4c).

Effects of LAP and free radical absorber concentration on cell viability of direct printed cells

As this dissertation focuses on the encapsulation of cells within patterns, various compositions of prepolymer solution, photoinitiator, LAP, and additives to improve printing resolution, namely a free radical absorber, 2,2,6,6-tetramethyl-1-piperidinyloxy (TEMPO) were tested. 10T1/2 murine mesenchymal stem cells were encapsulated in a 7.5% GelMA with varying LAP concentrations from 0.1% to 1%. Representative Calcein AM/Ethidium I live/dead day 3 stained samples are shown in figure 5a. The viability of encapsulated 10T1/2s decreased from 79± 6% for samples printed with 0.1% LAP, to 68± 4% for 0.2% LAP, and 53± 5% for 0.5% LAP, before significantly decreasing to 30± 3% for samples printed with 1% LAP (figure 5b).

The addition of the free radical absorber, TEMPO, can be used to improve resolution by stopping crosslinking or by absorbing free radicals (figure 6a). Representative live/dead images of control 7.5% GelMA 0.1% LAP slabs and slabs with the addition of 0.005% TEMPO and 0.05% TEMPO can be observed in figure 6b. The addition of TEMPO, even in low concentration (0.005%), decreases the viability to 69± 4%, and significantly lowers viability of 59± 6% for 0.01% TEMPO, 43 ± 6% for 0.02% TEMPO, 33 ± 9% for .04%, and 24 ± 3% for 0.05% TEMPO (figure 6c).

Encapsulation of Neonatal Murine Cardiomyocytes in GelMA hydrogels

NMVCMs were successfully encapsulated in 5% GelMA hydrogels in a 3 x 3 mm slab pattern and within a parallel line pattern with line widths of 50 μm and spacing of 50 μm on glass coverslips from 5 million to 40 million cells/mL. At low concentrations (5 and 10 million cells/mL) samples did not require increased exposure time to polymerize. However, at 20, 30, and 40 million cells/mL, exposure times were increased by 50% to ensure an intact and robust pattern. Samples were printed with a 125 μm PDMS barrier to prevent scaffolds from sticking and tearing from the glass slide. Slab samples were printed with 10 million cells/mL to determine the effect of GelMA concentration on NMVCM viability. Cardiomyocytes observed on day 3, had similar viability of 60 ± 3% and 61 ± 5% for 5% and 7.5% GelmMa, respectively and 42 ± 5% for 15% GelMA (figure 7). Brightfield images of slab and patterned scaffolds are shown in figure 8a. Individual cell beats are observed as early as day 1 after printing, with NMVCMs beginning to hypertrophy by day 3. Samples can be observed beating synchronously by day 3 (Figure?). Video capture of cardiomyocytes that are patterned in an isotropic slab

and parallel lines, show synchronicity of spontaneous beating of patterned cells (supplementary video 1) compared to slab cells (supplementary video 2).

When compared to NMVCMs seeded on glass, cardiomyocytes do not portray phenotypic expression of α-actinin unless they are seeded on top of other cells (figure 8b), whereas cells seeded on 5% GelMA slab exhibit striated α-actinin fibers. This highlights the compatibility of 5% GelMA with NMVCMs. NMVCMs encapsulated in 5% GelMA also stain positive for α-actinin, for both slab and parallel lines across the entire printed scaffold (figure 8c). NMVCMs encapsulated in slab show a more equally distribution of sarcomere angles, with no preference in direction when compared to NMVCMs in lines (figure 8d). Emphasizing the ability to align NMVCMs in patterned gels using the μCOP system, NMVCMs encapsulated in an individual line pattern and will align to the pattern and their sarcomeres will preferentially align perpendicular to the direction of the pattern (figure 8e).

To further optimize the material selection for printing, NMVCMs were printed separated from each other, allowing them to only interact with the GelMA material. NMVCMs were successfully printed in individual line patterns of varying GelMA concentrations from 5, 7.5, and 15% (figure 9a). Sarcomeres of cardiomyocytes encapsulated within 5% and 7.5% GelMA lines were measured, as α-actinin expression was minimal across 15% GelMA lines. For NMVCMs encapsulated in 5% GelMA, the average sarcomere length was 1.83 ± 0.05 μm, whereas the average sarcomere length of NMVCMS encapsulated in 7.5% GelMA was 1.72 ± 0.04 μm. (Figure 9b, SEM n=3). Lastly, NMVCMs were encapsulated in 5, 7.5, and 15% GelMA lines at 5 million cells/mL to determine the contractile function of individual cells in these materials. An

individual NMVCM in 5% GelMA had a maximum displacement of 9.6 μm, while an NMVCM in 7.5% GelMA had a maximum displacement of 5.3 μm and in15% GelMA at 4.5 μm. Thus, 5% GelMA will be used in future chapters 4 and 5 as the main material for encapsulating cardiomyocytes.

Discussion

3D-printing technologies have become an emerging tool for recreational, commercial, and research purposes. μCOP was a brand-new technology developed in our lab and the focus of my work has been the expansion of printing methodologies with this system and towards cardiac tissue engineering. The use of grayscale and color images has greatly increased the capabilities of light-based 3D printers, improving the flexibility of pattern design, and is utilized to improve the printing resolution of 3D scaffolds printed in subsequent chapters. By having specific control of when the mirrors are on or off, and optimizing the composition of the prepolymer solutions, I can prevent diffusion-based polymerization beyond the volume illuminated by the μCOP system. Furthermore, the development of color-based digital pattern design in our lab has greatly improved the speed in which users can design and align multiple material prints. Although rudimentary, the design of 2D patterns that will be projected in 3D space is still relevant even with the increased use of CAD-based models in scaffold design. With the development of new materials and compositions for various tissue engineering applications, varying designs is easier in 2D than varying in 3D. This is highlighted in the optimization of printing various concentrations of GelMA, LAP photoinitator, and pattern design.

The exposure times for varying concentrations of GelMA follows a power law dependence as opposed to a linear dependence since as concentrations increase, intermolecular interactions of gelatin helices become more likely. This can lead to an increased proximity of methacrylate groups per unit volume, increasing the probability of a crosslinking event[65]. Similarly, the compressive modulus also follows a power law dependence, aligning well with previously published work[66,67] whereas photoinitiator (LAP) concentration follows an ideal rate of polymerization[68]. In this work, I have only characterized a high degree of substitution (DS) GelMA due to the sensitivity of acrylation at neutral pH and have focused on high-fidelity printing. A recently published report has shown the effects of buffer concentration, gelatin concentration, initial pH, methacrylic anhydride concentration, reaction temperature, and reaction time on the DS of GelMA[69] and should be referenced to specifically tailor the DS of GelMA for future studies.

In general, GelMA has been used in systems where the dimensions are typically fixed i.e. micromolding[70,71], within microfluidic devices[72,73], or via extrusion-based 3D printing[66,74]; thus, considerations to changes in print dimensions are not a concern. As μCOP and the patterns printed from this system are unique to each user, the overall pattern design must be carefully considered and optimized when designing a print. Using a single parameter (μm/pixel ratio) is not sufficient in designing scaffolds, and thus using CAD-based software to design digital patterns for printing is difficult. I have determined basic parameters to be considered when designing patterns- namely the proximity of printed areas to one another and how their relative sizes affect the printing μm/pixel ratio. As the pattern size increases the μm/pixel ratio decreases. However, by 40

pixels, this trend tapers off and the μm to pixel ratio stays near 5 μm/pixel. Since free radical polymerization is diffusion-based, the distance free radicals can travel before crosslinking or becoming annihilated should be similar. Thus, the decrease in μm/pixel ratio can be attributed to the lower amount of area surrounding the exposed pattern compared to when the pattern gets larger. One confounding issue is that as the size of the pattern increased, the exposure time had to be reduced from 16 seconds to 12 seconds for the largest patterns 80 pixels and 160 pixels. In both instances, the pattern would rip off, even with a hydrophobic PDMS boundary; however, this trend is observable even with the smaller patterns. Thus, "overpolymerization" is also a concern when attempting to fabricate 3D-printed structures. Another issue affecting printing is the proximity of the patterns to each other. Patterns very close to each other decreased the overall μm/pixel ratio but the changes in the printing ratio may plateau due to the fact that free radical polymerization is diffusion-limited. The amount of competition for free radical generators may attribute to the lower ratio. Further investigation into these two essential parameters is warranted to create a predictive model on the quality of future prints, especially to ensure successful printing at high resolutions and scaffold reproducibility. Furthermore, both parameters may contribute to changes in mechanical properties of neighboring patterns in a print and should be investigated further.

There is a growing amount of evidence that 3D culture may better resemble native tissue[64,75–77]. Thus, with direct patterning of cells within hydrogels, it is important to determine the effects of prepolymer solution composition, i.e. gel concentration, photoinitiator, free radical absorber, on cell viability. Not unsurprisingly, the cell viability of 10T/12 cells decreased as photoinitiator increased. As the UV exposure decreased at

higher concentrations, this increase in cell death can be more greatly attributed to free radical generation than UV damage. Along these lines, it has been found previously that methacrylate groups have a cytoprotective effect as they will utilize the free radicals generated during polymerization.[78] Thus, low LAP concentration and longer exposure time will be sufficient for the future work within this dissertation. The effect of adding TEMPO to culture has been shown to induce apoptosis at concentrations as low as 1 mM via caspase-mediated signaling pathway.[79] As a result, TEMPO will not be added in future studies.

Moving towards encapsulating cardiomyocytes in hydrogels, exposure time for gels must be increased by 50% at high concentrations (20-40million cells/mL) compared to acellular scaffolds. This is because cells are not transparent and can scatter light, which disrupts the crosslinking of the GelMA hydrogel. 60% viability is not ideal; however, samples were printed at a lower concentration to help better visualize live and dead cells for quantification by preventing aggregation. Thus, the overall lower porosity and higher stiffness of the gel, reducing access to nutrients, along with the rigorous decellularization and disassociation process, may be a contribution factors to low viability.

When NMVCMs were encapsulated in GelMA, both line and slab pattern exhibited improved sarcomere expression than when compared to cells grown on glass. This is due to a mismatch in mechanical stiffness of glass substrate (1 MPa) to what cardiomyocytes prefer (10-12kPa)[36,37]. A significant amount of work has been made to design 3D models; however, many rely on reorganization of cardiomyocytes in collagen or ECM gels, having only macroscopic control of the aligned tissue[75,80–82]. Direct encapsulation of cardiomyocytes in line patterns greatly improved sarcomeric

alignment when compared to those given no direction (figure 8d). Alignment of seeded cardiomyocytes via anisotropic patterning is well understood [6,9] and the aforementioned studies corroborate the effect of encapsulating NMVCMs in 3D patterns to improve alignment.

NMVCMs encapsulated in 5% GelMA expressed longer sarcomeres than those encapsulated in 7.5% GelMA lines. Although treatment with 40 mM 2, 3 butedione monoxime (BDM), a known myosin ATPase inhibitor[83], should have relaxed sarcomeres, an increased passive stress from noncardiomyocytes may be responsible for the observed decrease in sarcomere length for the NMVCMs encapsulated in 7.5% GelMA. Very few NMVCMs expressed ∝-actinin printed in 15% GelMA (figure 9b), which is partially attributed to the increase in cell death, but more likely due to the almost 10-fold increase in gel stiffness compared to 7.5% GelMA (figure 3e). Lastly, from preliminary studies with low cell concentrations, NMVCMs printed in 5% GelMA had twice the measurable displacement compared to cells printed in 7.5% and 15% GelMA lines. To extract discernable changes in force within an *in vitro* model i.e. increase force measuring resolution, I want to choose a material that maximizes displacement of patterned NMVCM tissue.

As a result, the research described in this chapter has led to a design choice of a prepolymer system using a 10% GelMA, 0.2% LAP solution mixed 1:1 with NMVCMs in dark media for a final concentration of 5% GelMA, 0.1% LAP to maximize cell viability. 50 µm line patterns improved cardiac alignment of sarcomeres and increased displacement, and spacing greater than 50 µm apart prevents mechanical and electrical stimulation between lines, preventing synchronicity over larger printed tissues. Printing

lines with 50 µm spacing is also a requirement for the millimeter scale tissue. The work described in this chapter focuses on the preliminary research required to optimize pattern design and application of µCOP bioprinting technology to cardiac tissue engineering and opens the door to developing future drug screening models with functional outputs using NMVCMs and human embryonic or induced pluripotent stem cell-derived cardiomyocytes described in the subsequent chapters of this dissertation.

Methods

Gelatin modification and solution preparation to produce photocrosslinkable hydrogels

Gelatin methacrylate (GelMA) was synthesized using previously described methods [67]. Briefly,10g of gelatin (gel strength 300), was dissolved in 100 mL of DPBS at 60ºC. 8 mL of methacrylic anhydride was added dropwise while stirring. After three hours of modification, the GelMA solution was diluted with 100 mL of DPBS and transferred into 15 kDa dialysis tubing and dialyzed for one week at 45ºC to remove unreacted methacrylic anhydride, salts, and shorter hydrolyzed chains of gelatin. Typically, 30-35 mLs of GelMA solution was added to a 50ml conical flask and was placed in the -80 ºC freezer. The 50 mL conicals were laid on their sides, propped at an angle to increase the surface area of the frozen gel and improve the rate of freeze-drying. GelMA was freeze dried and kept at -80ºC until a stock solution was prepared. The GelMA solid would appear as a porous, white foam. Each conical contained GelMA foam which would weigh around 500 mg, at a final concentration of roughly 14 mg/mL after dialysis.

To prepare a gelatin methacrylate solution, DPBS was initially warmed to 37ºC in a water bath to aid in dissolving of the GelMA foam. The foam, resembling the shape of the conical, was quickly placed on the scale to determine the mass. The GelMA foam was diced using a razor to increase surface area, reduce dissolving time, and to ensure that all GelMA was dissolved. It was quickly returned to the 50-mL conical to prevent absorption of water from the air as it is anhydrous and hydroscopic in its dried form. Strict adherence to the protocol is required to improve the consistency of calculated concentrations between batches of stock solution.

Once the DPBS was at 37ºC, it was added to one of multiple conicals. The GelMA was dissolved, however since the solid is very porous, a significant amount of bubbles were trapped in the solution. The solution required reheating prior to adding more solid. Generally, stock solutions were made at 200 mg/ml or 20% (wt/vol) as the highest concentration solution was 15% (wt/vol). Intermittent vortexing and heating was required until all solids were dissolved. To ensure all the solid GelMA was dissolved, the conical was spun at 210g for 30 seconds to remove the microbubbles from solution, leaving any undissolved solid material between a cloudy solution and bubble and air interface. If there still was undissolved GelMA, the previous steps of vortexing and centrifugation is required. Finally, the solution was sterile-filtered using a vacuum-driven 0.2 µm Steriflip filter (Millipore), and was heated via a retail 1875-watt hair drier on the lowest setting. After filtering, the GelMA stock solution appeared transparent and slightly beige in color. Typically, a GelMA stock solution required between one to two hours for preparation, depending on the quantity produced.

GelMA prepolymer solutions were prepared at least one day prior to use. To aid in producing consistent test solutions, GelMA stock solution was added to measured preheated DPBS and photoinitiator solution. The pipette tip was placed low within the DPBS and pressed slowly to prevent mixing. As the density of 20% GelMA is much greater than DPBS, the stock solution would fall to the bottom. Once the pipette was fully depressed, the pipette tip was raised to the meniscus of the solution and unmixed DPBS was used to rinse the pipette tip. Diluted solutions that were prepped were stored in a 4^{o}C fridge and are stable for at least one year. GelMA solutions were mixed from 2.5-15 (wt/vol) GelMA. After refrigeration, GelMA requires heating to melt and maintain the solution to liquid state. Solutions used the same day as preparation require longer exposure times than solutions that have been allowed to equilibrate overnight at 37^{o}C.

The photoinitiator lithium Phenyl-2,4,6-trimethylbenzoylphosphinate (LAP) was synthesized in-house following a previously described method [84]. 3.2 g (0.018 mol) of 2,4,6-trimethylbenzoyl chloride was added dropwise to an equimolar amount (3.0g) of continuously stirred dimethyl phenylphosphonite. The reaction mixture was stirred for 18 hours at room temperature under argon. The mixture was then heated to 50^{o}C and a four-fold excess of lithium bromide (6.1g) was added in 100 mL of 2-butanone. After 10 minutes a solid precipitate formed. The mixture was cooled to room temperature and allowed to rest for four hours. The precipitate was washed and filtered three times with 2-butanone to remove unreacted lithium bromide and excess solvent was removed by vacuum pump.

Measuring Compressive Modulus of GelMA hydrogels

1 mm diameter x 2 mm height cylindrical pillars were printed on a methacrylated

coverslip using the μCOP system. GelMA was added between two 2 mm PDMS spacers and two circular patterns spaced 2 mm apart were printed. Exposure times were adapted from the previous experiments per GelMA concentration. Samples were incubated in DPBS at 37°C and 5% CO_2 for 24 hours before measurements were made. Samples were removed and placed into a DPBS bath on the CellScale Microsquisher instrument. A 60 mm tungsten beam of known diameter was attached to the system and the final length was measured. A 3 mm steel plate was superglued to the edge and allowed to cure. The tungsten beam was then placed on the system. Using the high precision stage, the beam and plate were oriented towards the midpoint of the sample and the sample was compressed for 100 μm over 30 second at an acquisition rate of 5 Hz. The force was calculated using a simplified Euler-Beam theory equation [85]:

$$\omega = \frac{F \times L^3}{3 \times E \times I} \tag{2.3}$$

Where F=force, ω=displacement, L=length of the beam, E=modulus, and I (beam moment of inertia) is:

$$I(cylinder) = \frac{\pi \times r^4}{4} \tag{2.4}$$

Where r= radius of the beam. The linear portion of the stress-strain curve was analyzed for the compression modulus.

Analysis of line pattern prints

A premixed solution of 7.5% GelMA 0.2% LAP with 0.02% TRITC-Dextran was made and an exposure time of 16 seconds was utilized since overpolymerization did not

occur and underpolymerization was minimal for 10 pixel lines (little to no sinusoid visualized). Fluorescent images were taken at the base of the structures and a line profile was drawn across the middle of the scaffold. The line edges were determined by the max peak heights of the derivative of the fluorescence profile and averaged.

10T1/2 Cell culture

10T1/2s were purchased from ATCC, thawed, and plated on a 75 cm^2 tissue culture flask in 10 mL of Dulbecco's Modified Eagle Media (DMEM) and 10% (v/v) fetal bovine serum. Media was changed every 48 hours and cells were passaged around 80% confluency. Samples printed in this section were between passages 6-8.

Viability Assay of Encapsulated Samples

A staining solution of 2 µM Calcein AM and 4 µM ethidium homodimer in DPBS was made. Media was aspirated, and the staining solution was immediately applied. The stain was incubated for 30 minutes at room temperature. Samples were washed 3 times with DPBS for 5 minutes each and samples were imaged under fluorescence microscopy. Samples were randomized and hand counted.

Immunofluorescence Staining and Imaging for the Assessment of NMVC morphology

Constructs with encapsulated NMVCs were fixed in 4% (v/v) paraformaldehyde in DPBS for 15 minutes at room temperature and subsequently blocked and permeabilized by 2% bovine serum albumin (BSA) solution with 0.1% Triton X-100 for one hour at room temperature. Samples were incubated with primary antibodies against

α-actinin and connexin-43 overnight at 4^{o}C. Secondary antibody and nuclear counterstain were incubated at room temperature for 1 hour in the dark. Confocal immunofluorescence images were acquired with 40X, 0.8 NA water-immersion objective lens attached to an Olympus FV1000 microscope to compare the cell morphology, and nuclear and sarcomere alignment in NMVCs. Directionality of sarcomeres and nuclei were analyzed using ImageJ Fourier components of the directionality plugin.

Contributions:

Chapter 2, in part, is currently being prepared for submission for publication of the material. Liu J, Ma X, Dewan S, Lawrence N, Miller K Whang G, You S, Chung P, Chen S. Direct 3D BioPrinting of Cardiac Microtissues Mimicking Native Myocardium. The dissertation author was the primary investigator and primary author of this material.

Figures

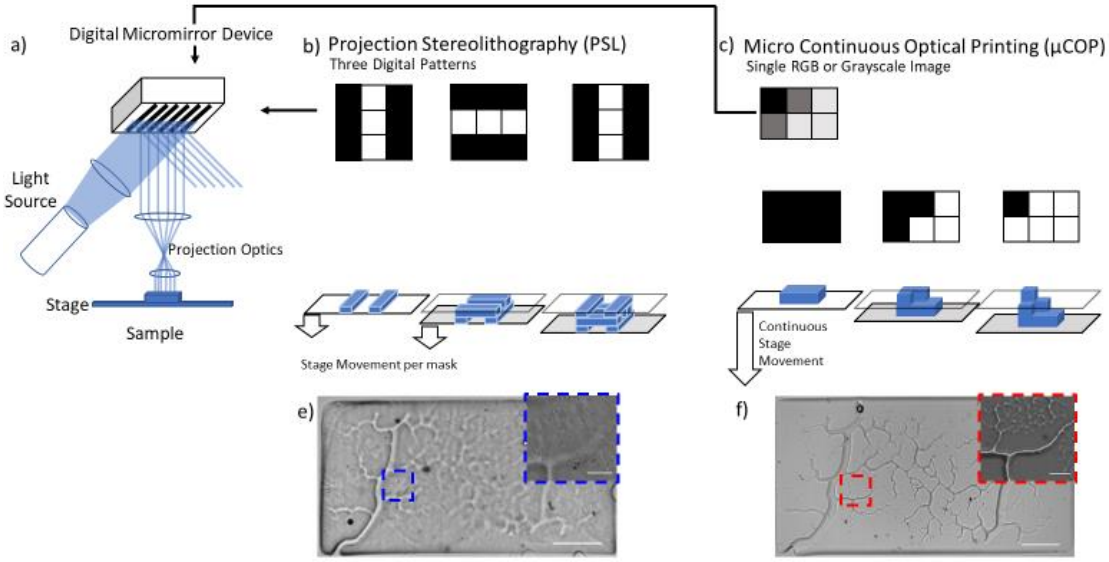

Figure 2.1: Comparison of Light-Based Projection 3D printers. a) Schematic of a DMD device, including a light source, DMD, and a set of projection optics to focus the digital pattern onto a substrate. b) Comparison of pattern design and stage movement for Projection Stereolithography (PSL) and c) Micro-Continuous Optical Printing (µCOP) and DIC images showing e) PSL printing of a complex vascular structure and f) µCOP printing of the same vascular structure (scale bar= 500 µm, inlay scale bar=100 µm)

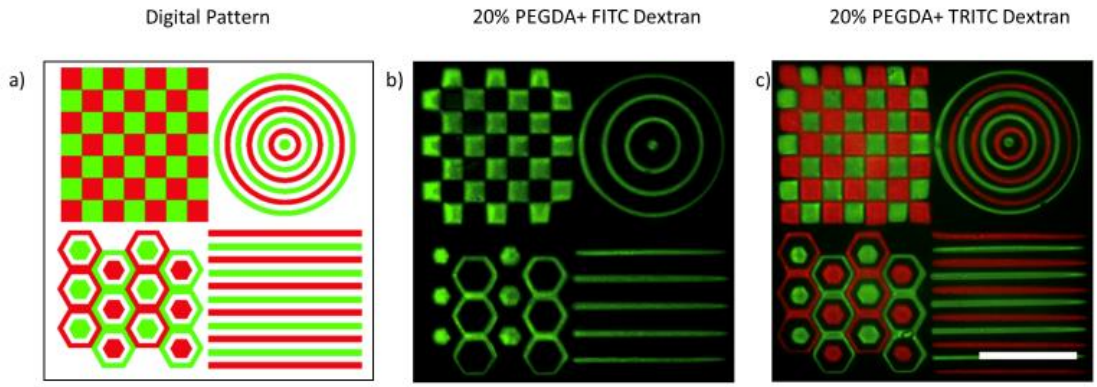

Figure 2.2: µCOP enables the printing of multiple materials in specific positions. a) A digital pattern designating two masks (green and red) that will be printed sequentially. b) The first patterned printed with 20% PEGDA and 0.2% LAP with 0.1 mg/mL FITC-Dextran c) The mask is changed and exposing the alternate pattern onto 20% PEGDA 0.2% LAP with 0.1 mg/mL TRITC-Dextran. Scale bar is 500 µm.

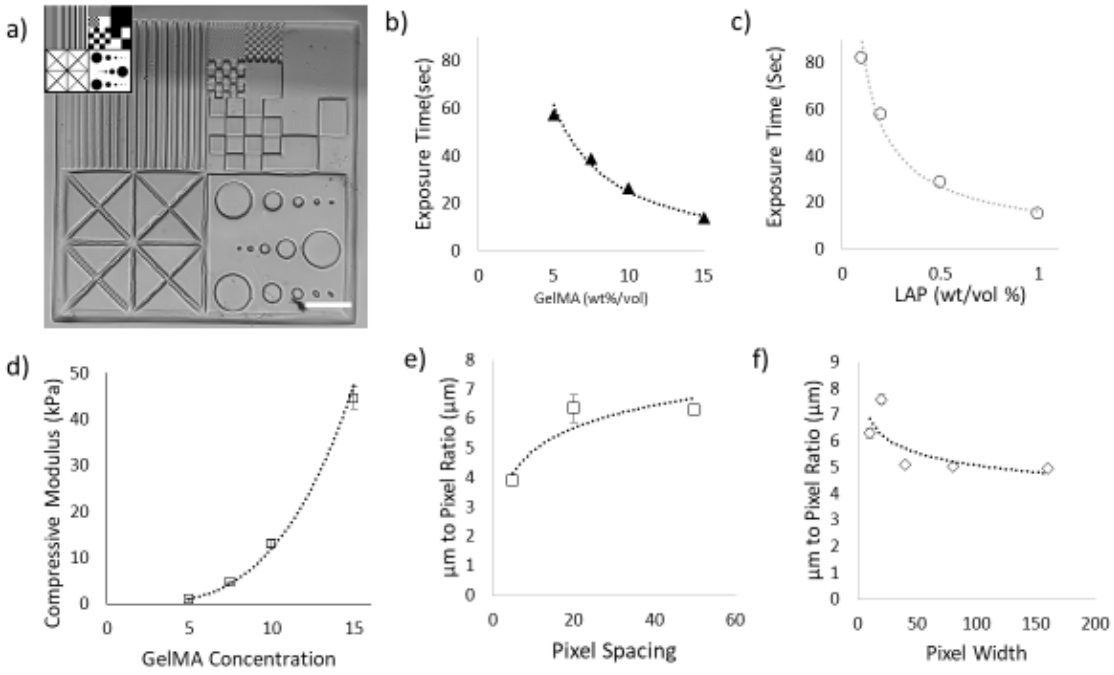

Figure 2.3: Printing parameter optimization. a) Representative image of a printed test pattern (digital pattern in inlay) b) Exposure time of printed scaffolds based on GelMA concentration c) Exposure time of printed scaffolds based on LAP concentration d) Compressive modulus of increasing GelMA concentration (SEM, N=6). e) µm to pixel ratio based off of pattern spacing (SEM, N=3) and f) pattern width (SEM, N=3).

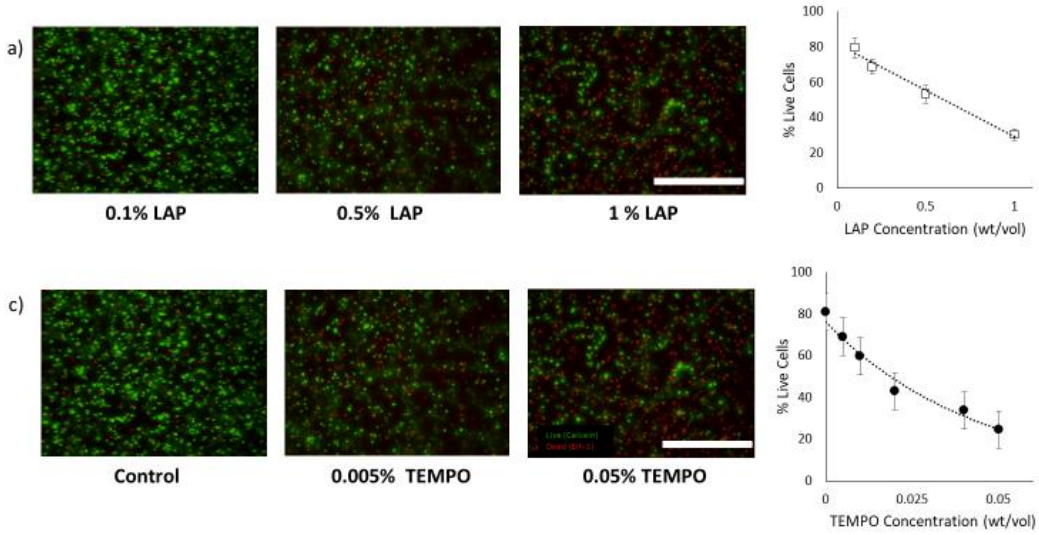

Figure 2.4: Viability of 10T1/2 mesenchymal stem cells encapsulated in 7.5% GelMA. a) representative images of encapsulated cells using various concentrations of LAP stained with calcein AM (live) and ethidium I (dead) and b) the average percentage of live cells quantified (SEM, N=3). c) Representative live/dead stains of 10T1/2s encapsulated in 7.5% GelMA 0.1% LAP with additions of TEMPO and d) the average percentage of live cells (SEM, N=3). All scale bars are 500 µm.

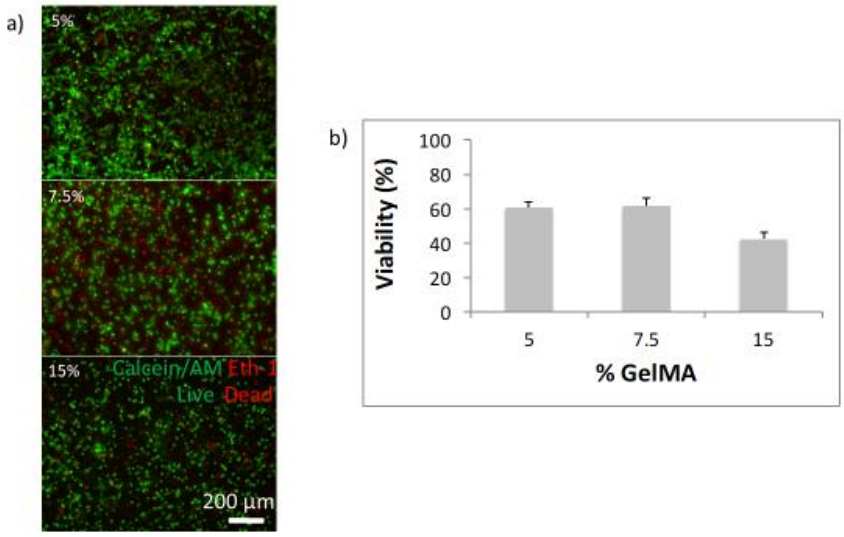

Figure 2.5: Viability of NMVCMs encapsulated in various concentrations of GelMA. a) Representative fluorescent images of NMVCMs stained with calcein AM and Ethidium I. Viabilitiy decreases with increased GelMA concentration (SEM, N=3). Scale bar is 200 µm.

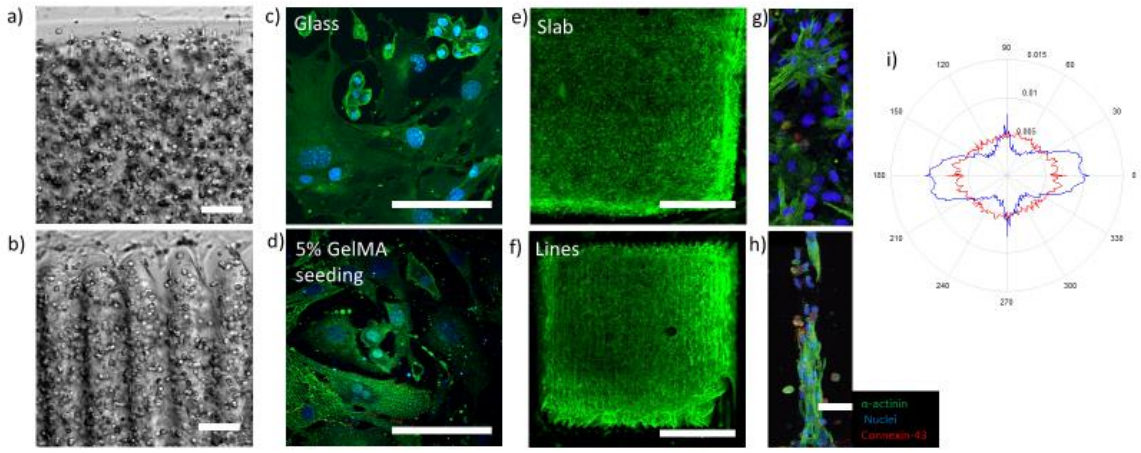

Figure 2.6: Patterning NMVCMs in GelMA hydrogels. a) DIC image of NMVCMs encapsulated in slab and b) line pattern (Scale bar is 50 µm). c) Confocal images counterstained for nuclei (blue) and α-actinin (green) and connexin-43 (red) of NMVCMs c) seeded on glass and d) on 5% GelMA (scale bar is 100 µm). NMVCMs encapsulated in a e) slab pattern and f) line pattern counterstained for α-actinin (green), scale bar is 1 mm. High magnification images of NMVCMs encapsulated in g) slab and h) a single 50 µm line, counterstained for nuclei (blue) and α-actinin (green) and connexin-43 (red) (scale bar is 25 µm). j) Polar graph of aligned sarcomeres for NMVCMs encapsulated in slab (red) and NMVCMs encapsulated in a single line (blue).

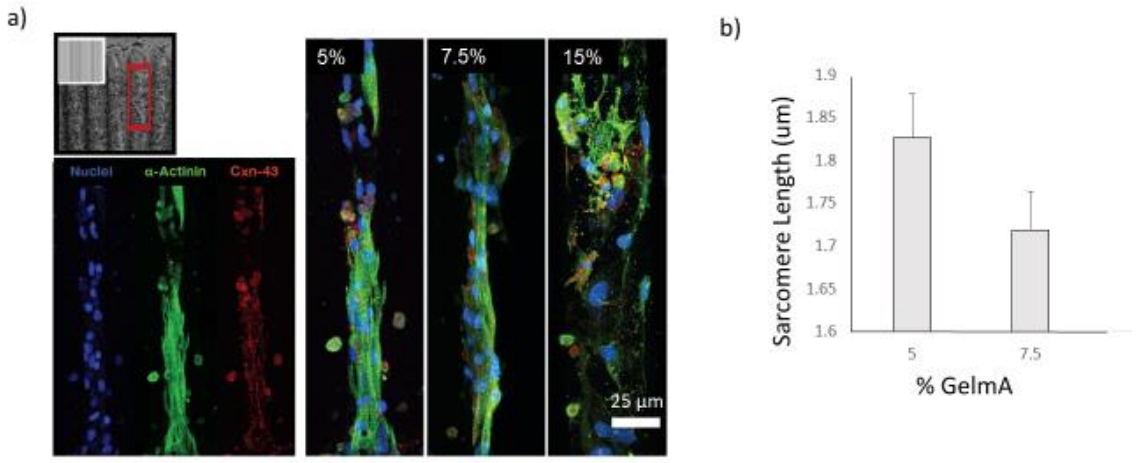

Figure 2.7: GelMA concentration alters sarcomere length. a) NMVCMs encapsulated in 5, 7.5, and 15% GelMA counter stained for nuclei (blue) α-actinin (green), connexin 43 (red). b) Average sarcomere lengths were measured to be 1.83 ± 0.05 µm, whereas the average sarcomere length of NMVCMs encapsulated in 7.5% GelMA was 1.72 ± 0.04 µm (SEM, N=3).

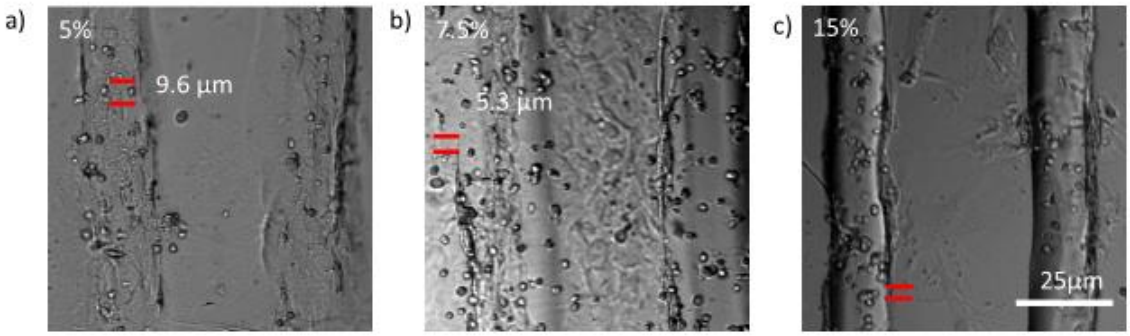

Figure 2.8: Displacement of NMVCMs encapsulated in GelMA. Measured displacement NMVCMs encapsulated in a) 5% GelMA, b) 7.5% GelMA, and c)15% GelMA. Red lines indicate the displacement over time.

References:

[1] D.-H. Kim, E.A. Lipke, P. Kim, R. Cheong, S. Thompson, M. Delannoy, K.-Y. Suh, L. Tung, A. Levchenko, Nanoscale cues regulate the structure and function of macroscopic cardiac tissue constructs, Proc. Natl. Acad. Sci. 107 (2010) 565–570.

[2] M. Wanjare, L. Hou, K.H. Nakayama, J.J. Kim, N.P. Mezak, O.J. Abilez, E. Tzatzalos, J.C. Wu, N.F. Huang, Anisotropic microfibrous scaffolds enhance the organization and function of cardiomyocytes derived from induced pluripotent stem cells, Biomater. Sci. 5 (2017) 1567–1578.

[3] P.W. Alford, A.W. Feinberg, S.P. Sheehy, K.K. Parker, Biohybrid thin films for measuring contractility in engineered cardiovascular muscle, 2010.

[4] A. Atmanli, I.J. Domian, Generation of aligned functional myocardial tissue through microcontact printing., J. Vis. Exp. (2013) e50288.

[5] C. Zuppinger, 3D culture for cardiac cells, Biochim. Biophys. Acta - Mol. Cell Res. 1863 (2016) 1873–1881.

[6] K.C. Hribar, D. Finlay, X. Ma, X. Qu, M.G. Ondeck, P.H. Chung, F. Zanella, A.J. Engler, F. Sheikh, K. Vuori, S.C. Chen, Nonlinear 3D projection printing of concave hydrogel microstructures for long-term multicellular spheroid and embryoid body culture, Lab Chip. 15 (2015) 2412–2418.

[7] W. Zhu, X. Qu, J. Zhu, X. Ma, S. Patel, J. Liu, P. Wang, C.S.E. Lai, M. Gou, Y. Xu, K. Zhang, S. Chen, Direct 3D bioprinting of prevascularized tissue constructs with complex microarchitecture, Biomaterials. 124 (2017) 106–115.

[8] J. Liu, H.H. Hwang, P. Wang, G. Whang, S. Chen, Direct 3D-printing of cell-laden constructs in microfluidic architectures, Lab Chip. 16 (2016) 1430–1438.

[9] K. Kim, W. Zhu, X. Qu, C. Aaronson, W.R. McCall, S. Chen, D.J. Sirbuly, 3D Optical Printing of Piezoelectric Nanoparticle–Polymer Composite Materials, ACS Nano. 8 (2014) 9799–9806.

[10] C. Cha, P. Soman, W. Zhu, M. Nikkhah, G. Camci-Unal, S. Chen, A. Khademhosseini, Structural reinforcement of cell-laden hydrogels with microfabricated three dimensional scaffolds, Biomater. Sci. 2 (2014) 703–709.

[11] P. Soman, P.H. Chung, A.P. Zhang, S. Chen, Digital microfabrication of user-defined 3D microstructures in cell-laden hydrogels, Biotechnol. Bioeng. 110 (2013) 3038–3047.

[12] X. Ma, X. Qu, W. Zhu, Y.-S. Li, S. Yuan, H. Zhang, J. Liu, P. Wang, C.S.E. Lai, F. Zanella, G.-S. Feng, F. Sheikh, S. Chien, S. Chen, Deterministically patterned biomimetic human iPSC-derived hepatic model via rapid 3D bioprinting, Proc. Natl. Acad. Sci. 113 (2016) 2206–2211.

[13] A.I. Van Den Bulcke, B. Bogdanov, N. De Rooze, E.H. Schacht, M. Cornelissen, H. Berghmans, Structural and Rheological Properties of Methacrylamide Modified Gelatin Hydrogels, Biomacromolecules. 1 (2000) 31–38.

[14] W. Schuurman, P.A. Levett, M.W. Pot, P.R. van Weeren, W.J.A. Dhert, D.W. Hutmacher, F.P.W. Melchels, T.J. Klein, J. Malda, Gelatin-Methacrylamide Hydrogels as Potential Biomaterials for Fabrication of Tissue-Engineered Cartilage Constructs, Macromol. Biosci. 13 (2013) 551–561.

[15] J.W. Nichol, S.T. Koshy, H. Bae, C.M. Hwang, S. Yamanlar, A. Khademhosseini, Cell-laden microengineered gelatin methacrylate hydrogels, Biomaterials. 31 (2010) 5536–5544.

[16] L.A. Rodriguz, Ferdinand, Cohen, Claude, Ober Christopher K, Archer, Principles of Polymer System, 2003.

[17] H. Shirahama, B.H. Lee, L.P. Tan, N.-J. Cho, Precise Tuning of Facile One-Pot Gelatin Methacryloyl (GelMA) Synthesis, Nat. Publ. Gr. (2016).

[18] G. Eng, B.W. Lee, H. Parsa, C.D. Chin, J. Schneider, G. Linkov, S.K. Sia, G. Vunjak-Novakovic, Assembly of complex cell microenvironments using geometrically docked hydrogel shapes, Proc. Natl. Acad. Sci. 110 (2013) 4551–4556.

[19] H. Aubin, J.W. Nichol, C.B. Hutson, H. Bae, A.L. Sieminski, D.M. Cropek, P. Akhyari, A. Khademhosseini, Directed 3D cell alignment and elongation in microengineered hydrogels, Biomaterials. 31 (2010) 6941–6951.

[20] H.-Y. Hsieh, G. Camci-Unal, T.-W. Huang, R. Liao, T.-J. Chen, A. Paul, F.-G. Tseng, A. Khademhosseini, Gradient static-strain stimulation in a microfluidic chip for 3D cellular alignment., Lab Chip. 14 (2014) 482–93.

[21] A. Hasan, A. Paul, A. Memic, A. Khademhosseini, A multilayered microfluidic blood vessel-like structure, Biomed. Microdevices. 17 (2015) 88.

[22] T. Billiet, E. Gevaert, T. De Schryver, M. Cornelissen, P. Dubruel, The 3D printing of gelatin methacrylamide cell-laden tissue-engineered constructs with high cell viability, Biomaterials. 35 (2014) 49–62.

[23] J.T. Hinson, A. Chopra, N. Nafissi, W.J. Polacheck, C.C. Benson, S. Swist, J. Gorham, L. Yang, S. Schafer, C.C. Sheng, A. Haghighi, J. Homsy, N. Hubner, G. Church, S.A. Cook, W.A. Linke, C.S. Chen, J.G. Seidman, C.E. Seidman, Titin mutations in iPS cells define sarcomere insufficiency as a cause of dilated cardiomyopathy, Science (80-.). 349 (2015) 982–986.

[24] C.S. Chen, Forum 3D Biomimetic Cultures: The Next Platform for Cell Biology, Mol. Biol. Gene Mol. Biol. Cell, Garl. Sci. Nat. Med. Clevers, H. Cell. 3 (2016) 1570–1576.

[25] B.M. Baker, C.S. Chen, Deconstructing the third dimension – how 3D culture microenvironments alter cellular cues, J. Cell Sci. 125 (2012) 3015–3024.

[26] L. Calvillo, R. Latini, J. Kajstura, A. Leri, P. Anversa, P. Ghezzi, M. Salio, A. Cerami, M. Brines, Recombinant human erythropoietin protects the myocardium from ischemia-reperfusion injury and promotes beneficial remodeling, Proc. Natl. Acad. Sci. 100 (2003) 4802–6.

[27] S. Suy, J.B. Mitchell, A. Samuni, S. Mueller, U. Kasid, Nitroxide tempo, a small molecule, induces apoptosis in prostate carcinoma cells and suppresses tumor growth in athymic mice, Cancer. 103 (2005) 1302–1313.

[28] A.J. Engler, C. Carag-Krieger, C.P. Johnson, M. Raab, H.-Y. Tang, D.W. Speicher, J.W. Sanger, J.M. Sanger, D.E. Discher, Embryonic cardiomyocytes beat best on a matrix with heart-like elasticity: scar-like rigidity inhibits beating, J. Cell Sci. 121 (2008) 3794–3802.

[29] A.J.S. Ribeiro, Y.-S. Ang, J.-D. Fu, R.N. Rivas, T.M.A. Mohamed, G.C. Higgs, D. Srivastava, B.L. Pruitt, Contractility of single cardiomyocytes differentiated from pluripotent stem cells depends on physiological shape and substrate stiffness, Proc. Natl. Acad. Sci. 112 (2015) 12705–12710.

[30] G. Kensah, A.R. Lara, J. Dahlmann, R. Zweigerdt, K. Schwanke, J. Hegermann, D. Skvorc, A. Gawol, A. Azizian, S. Wagner, L.S. Maier, A. Krause, G. Dräger, M. Ochs, A. Haverich, I. Gruh, U. Martin, Murine and human pluripotent stem cell-derived cardiac bodies form contractile myocardial tissue in vitro, Eur. Heart J. 34 (2013) 1134–1146.

[31] D. Zhang, I.Y. Shadrin, J. Lam, H.-Q.Q. Xian, H.R. Snodgrass, N. Bursac, Tissue-engineered cardiac patch for advanced functional maturation of human ESC-derived cardiomyocytes, Biomaterials. 34 (2013) 5813–5820.

[32] S.S. Nunes, J.W. Miklas, J. Liu, R. Aschar-Sobbi, Y. Xiao, B. Zhang, J. Jiang, S. Massé, M. Gagliardi, A. Hsieh, N. Thavandiran, M. a Laflamme, K. Nanthakumar, G.J. Gross, P.H. Backx, G. Keller, M. Radisic, Biowire: a platform for maturation of human pluripotent stem cell-derived cardiomyocytes, Nat. Methods. 10 (2013) 781–787.

[33] A. Agarwal, Y. Farouz, A.P. Nesmith, L.F. Deravi, M.L. McCain, K.K. Parker, Micropatterning Alginate Substrates for In Vitro Cardiovascular Muscle on a Chip, Adv. Funct. Mater. 23 (2013) 3738–3746.

[34] J. Borlak, C. Zwadlo, The myosin ATPase inhibitor 2,3-butanedione monoxime dictates transcriptional activation of ion channels and Ca(2+)-handling proteins, Mol Pharmacol. 66 (2004) 708–717.

[35] B.D. Fairbanks, M.P. Schwartz, C.N. Bowman, K.S. Anseth, Photoinitiated polymerization of PEG-diacrylate with lithium phenyl-2, 4, 6-

trimethylbenzoylphosphinate: polymerization rate and cytocompatibility, Biomaterials. 30 (2009) 6702–6707.

[36] E. Carrera, G. Giunta, M. Petrolo, Beam Structures, John Wiley & Sons, Ltd, Chichester, UK, 2011.

Chapter 3: Direct 3D BioPrinting of Cardiac Microtissues Mimicking Native Myocardium

Abstract

The heart possesses a complex three-dimensional (3D) organization; however, cardiac alignment in three dimensions has not been extensively used to study cardiomyocyte alignment. Consequently, engineering physiologically relevant 3D tissues remains a major challenge. Cellular alignment in 3D can be achieved by controlling scaffold microstructure and physically encapsulating cells near these geometric cues. Here I present a novel method of cell encapsulation in 3D methacrylated gelatin (GelMA) scaffolds patterned via Micro- Continuous Optical Printing (μCOP) that can rapidly and spatially pattern neonatal mouse ventricular cardiomyocytes (NMVCMs) within photocrosslinkable hydrogels. Embedded cardiomyocytes preferentially align with the designated microarchitecture and display phenotypic morphology and cytoskeletal alignment. Utilizing the μCOP system, an asymmetric, multi-material, cantilever-based scaffold was directly printed, allowing the force produced by the microtissue to translate onto a single pillar. To demonstrate the versatility of μCOP, NMVCMs were encapsulated in parallel lines, slab, grid, bow-tie, and randomly patterned gels and the effect of patterning on tissue displacement and synchronicity were investigated. Finally, force and calcium transients of the microtissue were measured at day 10 and 30, including treatment with isoproterenol to determine the sensitivity and maturity of the model. The presented system may be used to produce a 3D physiologically relevant *in*

vitro test model of organized cardiac tissue with great potential for use in drug screening and cardiac disease models.

Introduction:

The pumping action of the heart arises from the contraction of cardiomyocytes arranged in anisotropic layers of distinct orientations [86]. Previously, tissue engineering approaches have attempted to recapitulate native microstructures *in vitro* by creating nano- to microscale features such as grooves, patterned biochemical cues, or aligned nanofibers with traditional microfabrication techniques by seeding cardiomyocytes onto these patterned substrates. [6,54,56,87] These approaches allow for substantial control of alignment of cardiomyocytes according to mechanical cues produced by topographical patterning. Nonetheless, surface patterns or grooves can only induce cellular alignment in two dimensions (2D) and thus models created with these approaches have limited physiological relevance.

Several groups have reported various methods of producing 3D cardiac tissues for mechanical[9,11,12,42,88] or electrical interrogation[89,90]. Most require a cell seeding approach into prefabricated scaffolds which can yield inconsistencies in cell distribution due to cell aggregation, especially within wells and channels, potentially confounding results. This variability can be greatly reduced by directly patterning cells within the 3D environment. Furthermore, cellular responses, including cell morphology, cell-cell communication, and cell-material interaction for cells encapsulated into a 3D microarchitecture can be starkly different [64,91–93]. Thus, it is important to have a high degree of control over 3D microarchitecture. 3D printing has become an emerging tool

within the field of tissue engineering, allowing groups to design biomimetic scaffolds to better recapitulate native tissue [22,94]. Unlike standard extrusion-based 3D-printing that requires 1D raster-scanning of a 3D object, μCOP projects a 2D image into a volume of prepolymer solution, pairing stage movement with changes in digital masks, providing greater z-resolution and greatly increasing the speed of printing [60,95,96]. The user-defined patterns are loaded onto the digital micro-mirror device (DMD) chip, designating mirrors as on or off. Mirrors that are on reflect UV light, which is subsequently focused by the projection optics onto the prepolymer solution, immediately initiating polymerization to produce a 3D structure replicating the designated pattern.

In this study, I will present a novel method of using μCOP to produce a scalable 3D *in vitro* model mimicking the left ventricular myocardial microarchitecture and function. Utilizing the μCOP system, I have designed an asymmetric, customizable force measuring system with direct patterning of encapsulated cardiomyocytes. NNMVCMs progressively align with the designed microarchitecture and form a synchronous contracting tissue and force output is calculated based on the deflection of the 3D-printed force gauge. To highlight our system's ability to make complex patterns and sense their effects, various user-designed patterns, including a slab, grid, dispersion, and a randomized pattern, were also printed. Furthermore, I demonstrate that the 3D microtissues can be maintained long-term, produce high forces, and respond to drug at low concentration. The highly customizable 3D cardiac tissue is a potential tool for future disease modeling and drug discovery.

Results

Direct 3D-printing of cardiac micro-tissue using micro-continuous optical printing.

Using the μCOP system (figure 1a), a multimaterial print consisting of 1) 2%HA/2%PEGDA base layer, 2) 15% GelMA cantilevers, and 3) a parallel line pattern comprised of 5% GelMA was produced (figure 1b). A schematic of the printed scaffold is shown in figure 3c and a 3D reconstruction of α-actinin stained NMVCMs encapsulated between the scaffold can be seen in figure 1d. The final product is an elevated and patterned cardiac tissue with initial dimensions of 1.9 ± 0.02 x 0.91 ± 0.03 x 0.21 ± 0.02 mm (figure 1f, Length(L) x Width (W) x Height(H), n=6) and a cantilever that can be displaced with dimensions of 1.1 ± 0.03 x 0.23 ± 0.008 x 0.51±0.03 mm (figure 1e, n=19).

Displacement of seeded vs encapsulated 3D micro-tissues

NMVCMs were successfully cultured atop the 5% GelMA patterns with NMVCMs aligning to the designated parallel line pattern. As a comparison, NMVCMs were encapsulated using μCOP. Representative bright field images of seeded and encapsulated samples cultured for 10 days are seen in Figure 2a). Confocal microscopy z-projections were taken across the seeded scaffolds and stained for α-actinin (green, figure 2a). The seeded scaffolds have a sparser distribution of cells expressing α-actinin as compared to the encapsulated scaffold. Inlays show a compaction of cells for encapsulated samples as compared to seeded samples as crosstalk between lines can occur. Samples were stimulated using platinum electrodes and a Grass pulse generator (70 V, 10 ms delay) at 1, 2, and 4 Hz. Time lapse images of the microtissues were taken

at 5x and 10x magnification using a Leica inverted microscope at 20 frames per second (FPS). Using a custom MATLAB script, pillar displacement was determined by monitoring the change in position of a peak across a grayscale profile of the pillar between diastolic and systolic state over time (figure 2b). Representative traces of both seeded and encapsulated samples are shown in figure 2c. The maximum displacement from the relaxed position of seeded samples was calculated to be 12.0 ± 1.3 μm, 11.3 ± 1.2 μm, and 11.2 ± 1.6 μm at 1, 2, and 4 Hz stimulation (Supplementary video 3 and 4). The maximum displacement of encapsulated samples was 2 times as great at 24.9 ± 2.2 μm, 25.0 ± 2.2 μm, and 24.4 ± 2.2 μm at 1, 2, and 4 Hz, respectively (figure 2d, supplementary video 5, SEM, n=5, $p<0.005$). The length of relaxation of encapsulated samples were also significant larger, from 10.1 ± 0.9 μm, 9.9 ± 0.9 μm, and 6.8 ± 0.8 μm at 1, 2, and 4 Hz μm for seeded samples, as compared to encapsulated samples, relaxing for 24.2 ± 2.0, 23.0 ± 2.1, and 12.3± 1.4 μm at stimulation frequencies of 1, 2, and 4 Hz.

Encapsulating cardiomyocytes in complex geometries using μCOP.

Along with patterned lines, I investigated the capabilities of the μCOP system to print four additional patterns to determine how these patterns may affect the cardiomyocytes' ability to remodel according to these patterns. The four patterns considered were a slab, grid, dispersion, and a randomly connected set of lines (figure 3a. Differential interference contrast (DIC) images of each pattern type is shown in figure 3b. Videos of each pattern are shown in supplementary videos 6-10. Confocal images taken of each pattern on Day 10, were stained for α-actinin at 40x (figure 3c) and merged to show the distribution of sarcomeres. For both the slab and grid patterns the alignment of

cardiomyocytes is disrupted along the major axis of the scaffold. NMVCMs encapsulated within the dispersion pattern converged at the midpoint. Finally, encapsulated cells align to the random designated pattern. The varied pattern tissues were printed between the cantilevers and the displacement of the pillar was tracked. As seen in Table 1, the displacements of the various patterns, the line pattern is the only one to significantly improve the displacement of the cantilever. A one-way ANOVA was conducted to compare the effect of the patterns on displacement. An analysis of variance showed that the effect of the line pattern on displacement was significant compared to the other patterns ($F(4,24)=56.5$ $p<0.0000005$).

Table 3.1 Pillar Displacement in µm of various patterns

	Slab	Lines (encapsulated)	Grid	Dispersion	Random
1 Hz	2.10 ± 0.19	24.9 ± 2.2*	6.8 ± 1.3	6.1 ± 0.8	4.3 ± 0.8
2 Hz	1.91 ± 0.24	25.0 ± 2.2*	6.7 ± 1.3	5.9 ± 0.6	4.6± 0.8
4 Hz	2.21 ± 0.16	24.4 ± 2.2*	5.8 ± 0.8	5.6 ± 0.1	4.6 ± 0.6

Encapsulation of cardiomyocytes across 3D scaffold improves alignment.

By encapsulating NMVCMs into a line pattern, the NMVCMs can grow near the specified geometry. Confocal images were taken of samples of isotropic slab (left) and line pattern on glass (middle), and lines (right) printed across the 3D-printed scaffold at day 10 (figure 4a). The Fourier components of each the actinin filaments of each scaffold were analyzed (n=4 for each print). The slab pattern unsurprisingly had an even distribution across angles. The lines printed on glass showed an increase in frequency of

fibers between 85 and 105 degrees (one-tailed t-test, $p<0.05$) however, samples printed on the 3D scaffold showed a significant change in directionality of sarcomeres of all directions except 0-5, 60-70, 110-115, and 175-180^o (two-tailed t-test, $p<0.05$). To further characterize the scaffolds, samples were cultured for 30 days and the degree of compaction at the midpoint of the scaffold was measured at day 1, 10, and 30 (figure 4c). Originally, samples were 873±49 μm wide on day 1. At day 10, they contracted to 528 ± 154 μm and eventually by day 30 they contracted to 290 ± 88μm (figure 4d, n=14). Finally, sarcomere lengths across day 10 line patterns on glass, day 10 scaffolds, and scaffolds cultured for 30 days were measured (figure 4e). The average sarcomere lengths for day 10 line patterns printed on glass was 2.2 ± 0.02 μm, for day 10 3D scaffold was also 2.19 ± 0.05 μm and for day 30 samples, the average sarcomere length was significantly different to both day 10 samples at 2.34 ± 0.03 μm (figure 4f, SEM, n=4, $p<0.05$).

Calcium response of cardiac microtissues.

An increase in fluorescence was observed during systole as compared to diastole (Figure 5a). The average fluorescence was extracted from each frame. Characteristic calcium spikes were observed with normalized fluorescence ($\Delta F/F_o$). The NMVCM-encapsulated structure was treated with 100 nM isoproterenol (ISO) and incubated for 5 minutes at room temperature. After treatment with isoproterenol, the appearance of ectopic beats at 0.5 Hz were observed for day 10 and day 30 samples after treatment. Although, instances of ectopic beats were observed at low frequencies, one of five samples experienced an increase in the stimulation frequency it could catch from 4 to 5

Hz. Whereas for 3 day samples, all three samples experienced an increase in frequencies it could catch (7 to 8 Hz, 4 to 6 Hz, and 8 to 9 Hz) For day 10 samples the total peak fluorescence only increased significantly for samples stimulated at 0.5 Hz by 55 ± 29%, however the change in fluorescence at higher frequency, i.e. 4hz also increased after ISO treatment by 46 ± 22% ($p<0.05$, n=5). The maximum depolarization rate increased by 53 ± 25% and 42 ± 19% for 0.5 and 1 Hz ($p<0.05$, n=5) and the maximum rate of repolarization increased by 93 ± 43%, 74 ± 28%, and 56 ± 33% for 0.5, 1, and 2 Hz ($p<0.05$, n=5). For day 30 samples, the max fluorescence significantly increased for 1 Hz, 2 Hz, and 3 Hz by 30 ± 11, 24 ± 4, and 37 ± 9%, along with rate of depolarization for 2 and 3 Hz ($p < 0.01$, n=3).

μCOP allows for rapid tailoring of scaffolds for force measurement.

The system was designed to have two pillars, a cantilever and a support, where the force produced from the tissue will only deflect the cantilever. 500, 200, and 100 μm wide pillars (figure 6a) were bent using a 0.3046, 0.2048, and 0.1024 mm diameter tungsten wire, respectively, pressed 375 μm from the base, midway through where the tissue would be printed (figure 6b). The spring constant of each freestanding pillar 0.084 ± 0.005, 2.10 ± 0.15, 13.8 ± 1.7 μN/μm (n=13, 20, 8), respectively, after 24 hours incubation at 37ºC. Scaffolds were incubated at 37ºC for 10 and 30 days, with measured forces of 0.17 ± 0.03, 1.93 ± 0.13, 11.7 ± 0.7 μN/μm (n=8, 12, 12) on day 10, and 0.15 ± 0.07, 2.26 ± 0.16, 10.9 ± 0.6 μN/μm (n=9, 10, 14) on day 30. After empirically optimizing dimensions for the 3D cardiac tissue to display sufficient deflection, the 200 μm pillar was selected for future scaffolds. To attempt to replicate the full system, 2%

HA/2%PEGDA slab, both major and minor 15% GelMA pillars, and 5% GelMA lines were printed. Similarly, complete acellular scaffolds were tested using the Microsquisher under conditions stated previously. The addition of the HA/PEGDA base and 5% GelMA line did very little to change the spring constant of the minor pillar. The spring constant $K_{scaffold}$ was 4 ± 0.5, 2.8 ± 0.2 and 2.6 ± 0.2 μN/μm (n=6, 10, 9) on day 1, 10, and 30 for 200 μm-width cantilevers. Finally, scaffolds with cells encapsulated printed in 5% GelMA lines were measured on day 10 and day 30, having been treated in a bath of Tyrode's solution without calcium but with glucose and 2,3 butedione monoxime (BDM) to relax the scaffold. Scaffolds were pressed at the center plane of the tissue. The addition of cells nearly doubled the modulus of the scaffolds from 85 ± 9 kPa (acellular) to 148 ± 17 kPa (cellular) on day 10 and 74 ± 8 kPa (acellular) to 114 ± 26 kPa (cellular) on day 30 (figure 6e). These cellular moduli can be used for the forces generated by the aligned cardiac tissues. The calculated force for the parallel line pattern is 109.4 ± 9 μN and the tension was calculated to be 1.15 ± 0.22 mN/mm^2 (SEM, n=5)

Discussion.

Production of a proper cardiac tissue model has been a research subject for many groups [9,31,36,47,81], however there is still a need to produce a long-lasting model. The cardiac microtissue I have designed, that is pre-patterned with encapsulated with NMVCMs, shows both improved alignment and a known response to ionotropic drug. I used GelMA, a collagen-based photopolymerizable material, shown previously to be a favorable material for micropatterning tissue constructs and promoting cardiomyocyte attachment and spreading,[71]and LAP, a minimally toxic photoinitiator [84]. The μCOP

method allows one to rapidly iterate, without the need for a physical mask or mold, and design unique systems that can be tailored for various parameters, including but not limited to complex spatial patterning, tissue and geometries, multiple materials, and mechanical stiffness. Originally the 2% HA/2% PEGDA was originally chosen for two reasons: 1) As a negatively charged material [97] to prevent cell interaction, leading to cells not specifically printed to wash away, 2) As a sacrificial layer to be enzymatically degraded by hyaluronidase before measuring the displacement of pillars. Unfortunately, in doing so, the force generated by the cardiac tissue would rip off the cantilever. Potentially increasing the mechanical stiffness of the cantilever may alleviate this issue and could be revisited.

By directly encapsulating cells within a pattern, cells can elongate near physical ques to improve alignment when compared to an isotropic slab. By directly printing the tissue sample within the predefined mechanical tester, the samples lay within the same area and z-position, making it easier to measure and calculate force production. When comparing 2D and 3D samples, a greater number of cells were used per sample to seed than to encapsulate. Unfortunately, equal distribution of cells over the entire scaffold leads to many being seeded on the glass and well floor and unincorporated in the tissue, although many mainly fall within the patterned grooves. Although compaction does occur, there are still patches of gel unoccupied by cells on day 10. This may suggest the necessity of a secondary seeding to ensure complete coverage of the samples. However, by day 3, samples required media exchange daily as opposed to every 48 hrs. Thus, seeding at an even higher number of cells per well to ensure proper coverage can lead to practical challenges maintaining the samples over time. This leaves much to be desired

for a seeding methodology of this scaffold. However, when comparing the seeded scaffolds with the various scaffold designs that are discussed in figure 3, the alignment of NMVCMs on a simple pattern of parallel lines produced greater average displacements of the cantilever when compared to slab, dispersion, and random patterns. Thus, corroborating the concept that alignment of NMVCMs is paramount to the contractile properties of the scaffold.

Current 2D culture, especially on tissue culture plastic, is not sufficient to properly Whereas most groups require the self- alignment of cardiomyocytes encapsulated in extracellular matrix around stiff cantilevers [42,47,81,88] and 3D printing studies have been limited to log pile structures [34,51], this the first instance of seeing the effects of directly patterning various 3D microstructure and demonstrating the effects 3D patterns on cellular alignment and tissue displacement. Unsurprisingly, the slab pattern displaced the least. The pattern as previously shown in chapter 2 prevents cells from aligning, however, more importantly the amount of material that the cells must compress increases. Similarly, the disruption caused by the grid pattern prevented alignment of NMVCMs and caused isotropic compression of the scaffold when beating. However, when normalizing for the volume of printed tissue (mm displacement/mm^3), assuming the same thickness, the dispersion pattern also showed an increase in displacement compared to slab ($F(4,24)=44.4$, $p<0.005$) and random patterning ($F(4,24)=44.4$, $p<0.05$), however the displacement was still lower than the line pattern ($F(4,24)=44.4$, $p<0.00005$). The concept of prepatterning cells in specific geometries may be of significant interest in developing disease models where current models cannot recapitulate disease phenotypes that consist of myocyte disarray i.e. hypertrophic

cardiomyopathy [98]. Across all patterns, there was very little change in displacement with increased stimulation frequency suggesting a force-frequency of zero. One way to further investigate this is to potentially use a higher magnification objective (10x to 20x). At the current acquisition, the pixel to μm ratio is nearly 1 μm/ pixel. Increased resolution and increased acquisition time may be able to discern the force-frequency relationship of the printed scaffold in the future.

As described in the previous structure, printing of NMVCMs in patterned substrates improved alignment of cardiomyocytes. In this chapter, I looked at sarcomere alignment at the tissue level, and whereas in the previous chapter, alignment greatly improved between 90 ±15 degrees, tissues printed on glass vs slab, the frequency of alignment near ± 15 degrees only increases by 3%, whereas printed tissues on scaffolds increases by 12%. Qualitatively, one can discern a stronger alignment than expressed in these distributions. As these are averaged over entire z-stacks, the occurrence of noise in the form of sarcomeres near the perimeter of the cell may contribute to a dispersion of angles. Following a positive relation, increase in sarcomere lengths should increase forces generated [99] with maximal force generated at sarcomere lengths at 2.3 μm from isolated rat trabeculae. When comparing other mouse cardiac models, the sarcomere length at day 10 (2.2 μm) and day 30 (2.35 μm) is much larger (mean<2 μm) [12,46,100]. This discrepancy could be due to tracking sarcomeres at a relaxed state using BDM.

Further work is required to fully characterize the calcium handling of 3D-printed scaffolds. Finding imaging areas with minimal motion artifacts was difficult and in some cases choosing areas with significant motion was unavoidable. I had originally attempted

to mechanically decouple samples using BDM and was able to acquire calcium transients data, however, when changing the solution with fresh BDM and 100 nM ISO, the samples would begin to displace, affecting the sample pairing. Another point of interest that made acquisition difficult is that after treatment of ISO, the passive tension of the tissue would increase, and the imaging plane would shift. Therefore, to potentially avoid variations due to motion, transferring calcium imaging from a confocal microscope to a lower magnification objective on a standard inverted fluorescence microscope may aid in capturing fluorescence across the whole tissue, minimizing the effects of motion. However, given these shortcomings, an ionotropic effect was measured 0.5 Hz for day 10 and for 2 and 3 Hz for day 30 samples. An increase in samples for day 30 may elicit a statistically significant increase as both 0.5 and 1 Hz stimulations are $p<0.055$. A chronotropic effect was observed when treated with ISO in the form of ectopic beats at low frequencies, suggesting an increase in the resting heart rate for both day 10 and day 30 samples, while day 30 samples showed an increase in achievable stimulation catching up to 9 Hz (from 8 Hz). Beyond treatment with ISO, the effects of other drugs could be investigated.

These scaffolds were extensively characterized to determine the relationship of pillar size, addition of the full scaffold, along with cells to the stiffness of the printed cantilever. Thus, the mechanical properties can be used to estimate the forces generated per 3D printed NMVCM tissue. The calculated force 109.4 ± 9 μN and the tension was 1.15 mN/mm^2. It is difficult to find scaffolds within similar scale scaffolds, however study of similar scale showed a force generated of 16 μN [12]. However, tension normalized by cross-sectional area may be a better metric. Previous studies have

produced 0.5, 0.8, and 0.1 mN/mm^2 tension for rat neonatal CMs [10,42,44]. With its high tension, the proposed aligned 3D-printed cardiac tissue is a strong model as a potential drug screening model. Furthermore, the initial investigation of printing complex microarchitectures is a promising tool in studying and producing cardiac disease modeling. The long culture capabilities (>30 days) may allow for the potential to see how cardiomyopathies may manifest in early development, and how cell-cell, cell-microarchitecture, and electrical coupling affects tissue function and how certain drugs may affect tissue function long-term.

Methods

Pre-polymer Synthesis

Photoinitiator lithium phenyl-2,4,6-trimethylbenzoylphosphinate (LAP) was synthesized according to the previously published methods [84]. Gelatin methacrylate (GelMA) and Hyaluronic acid glycidyl methacrylate (HAGM) were synthesized according to previously published procedures [67,101,102].

Prepolymer Solution Preparation

Solutions are measured as wt/vol percentages, unless specified. A 4% LAP stock solution was dissolved in Dubelco's Phosphate Buffered Saline (DPBS) and filtered using a 0.22 µm filter. Lyophilized GelMA and HAGM foams were reconstituted with DPBS to produce stock solutions of 20% and 4%, respectively. Both solutions were warmed and sterile filtered using a 0.22 µm filter. Stock solutions were diluted with PBS

to make 15%, 10%, 7.5%, and 5% GelMA solutions with 0.2% LAP and 2% HA/2% (v/v) PEGDA with 0.2% LAP.

Neonatal Cardiomyocyte Isolation and culture

Neonatal mouse cardiomyocytes (NMVCs) were isolated from the hearts of neonates of CD-1 wild-type mice (Charles River Labs). In brief, hearts were surgically removed from 1-day-old pups and digested in Hank's Balanced Salt Solution (Gibco) with 0.046% Trypsin (Affymetrix) at 4 °C overnight. Blood cells were removed from hearts by type II Collagenase (Worthington) after shaking at 37 °C for two minutes. A heterogeneous cell population containing cardiomyocytes and fibroblasts was isolated after further digestion using type II Collagenase (Worthington) at 37 °C for seven minutes. Fibroblasts were removed by pre-plating for 1.5 hours on 75 cm2 plastic tissue culture flasks (Corning) in a humidified incubator at 37 °C with 5% CO_2. Isolated cardiomyocytes were resuspended in dark medium formulated by 75% Dubelco's Modified Eagle Medium (DMEM) and 25% M199 medium containing 10 mM 4-(2-hydroxyethyl)-1-piperazineethanesulfonic acid (HEPES), 10% horse serum (hyclone), 5% fetal bovine serum (Gibco), and 1% 100x Penicilin/Streptomycin/L-Glutamine solution. Media was replaced daily and on day 3, onward, a 10 µM mM solution of arabinosylcytosine (Ara-C), an antiproliferative drug to prevent noncardiomyocyte overgrowth.

3D-Printed Force Gauges and Cell Encapsulation

Utilizing the µCOP system, an array of micron-scale features was built in various biopolymers using UV polymerization in a layer-by-layer fashion as previously

described.[60] The main components of the fabrication system are a UV light source (Omnicure 2000), a digital light processing (DLP) chip (Discovery 4000, Texas Instrument), and computer controlled x-y-z stages (Newport 426/433 series). A 365 nm bandpass filter with a source output of 6 W/cm2 was utilized. User-defined bitmap patterns were transferred to the DLP chip and the modulated images were projected onto a photocurable pre-polymer solution through a UV- grade optical lens (Edmunds Optics). Areas illuminated by UV light crosslinked immediately, whereas dark regions remained uncrosslinked, forming the scaffold in a specific polymerization plane designated by the mask. These patterns were irradiated for 45 s at a projected UV intensity of 11 mW/ cm^2.

Initially, a solution of 2% HAGM, 2% (v/v) PEGDA, 0.2% LAP was injected between a methacrylated coverslip held by two 500 μm polydimethylsiloxane (PDMS) spacers. The solution was exposed to the first mask corresponding to a 2mm x 3mm x 250 μm base layer (Figure 1a-b, i). The remaining solution was washed in DPBS and replaced with 15% GelMA, 0.2% LAP solution. The solution was then exposed for 18 seconds by the pillar pattern (Figure 1a-b, ii), straddling the HA/PEGDA slab. The 15% GelMA solution was washed with warm DPBS and a 10% GelMA, 0.2% LAP solution was mixed 1:1 with a 50 million cells/ml suspension in DM to achieve a final concentration of 5% GelMA, 0.1 LAP, and 25 million cells/ml which was subsequently injected between the pillars. The cell solution was then exposed by the final line pattern (Figure 3a) for 45 seconds. The slab is a simple single exposure of a 1x1 x 2 mm area between the two pillars. The grid pattern uses the same line parallel line pattern with the addition of perpendicular lines of equal width and spacing. The dispersion pattern was designed to pass each line through the midpoint, while the random pattern connected each

line randomly using a randomizing script. Two additional lines were drawn on the first and last line to ensure the volume of cells would be similar to the line pattern. The average angle of the patterned lines -4^{o} from the major axis.

Samples were incubated in dark media at 37^{o}C and 5% CO_2 for two days, with media replaced on day 1. On day 3, samples were incubated in dark media with 10 µM Ara-C, replacing media every other day.

Calcium Imaging

To observe transient calcium, samples were first washed three times for 5 minutes at room temperature with 1.4 mM $CaCl_2$ in Tyrode's solution. Fluo-4 was loaded into cells using Tyrode's with 0.1% pluronic-127 and incubated for 30 minutes at 37^{o}C. Samples were washed three times for 5 minutes at room temperature and left in a solution of Tyrode's with 500 nm ascorbic acid to prevent phototoxicity. Samples were imaged with a Leica SP5 confocal microscope at 40x magnification utilizing the resonant scanner, at 128 x 128 pixel imaging area. Samples were stimulated with a 488 nm laser and observed at 84 frames a second. Samples were stimulated with a Grass stimulator using settings mentioned prior. The average fluorescence was extracted from each frame into a 1D fluorescence trace. Microtissues were washed three times in Tyrode's solution with 1.4mM $CaCl_2$. Fluo-4 (Life Technologies) was suspended in DMSO and added into Tyrode's solution with 0.1% (v/v) Pluronic 127 to a final working concentration of 5 µM. Constructs were incubated at 37^{o}C and 5% CO_2 for 30 minutes. Samples were washed three times for 5 minutes in Tyrode's solution with 1.4mM $CaCl_2$ and 500 nM L-ascorbic acid. Constructs were imaged using a Leica SP5 confocal microscope using a 40x water-

immersion lens, acquiring a 128x128 image at 84 frames/second. The tissues were paced by platinum wires 1 cm apart from 0.5-4 Hz using a Grass pulse generator (70 V, 10 ms delay).

Mechanical Testing

Isotropic cylinders, 1 mm Diameter x 2 mm tall, were polymerized utilizing the uCOP system and were allowed to swell at 37ºC for 1, 10 and 31 days. Compression testing was performed using a Cellscale Microsquisher. Experiment parameters include a rate of applied force to 100 uN over 1 minute. Force was calculated using a beam equation [85]:

$$D = \frac{F \times L^3}{3 \times \mathrm{E} \times I} \quad (1)$$

where D is the displacement, F is the force, L is the length of beam, E is the modulus. I_{cylinder} is given by:

$$I_{cylinder} = \frac{\pi \times r^4}{4} \quad (2)$$

where r is the radius of the beam.

Compression modulus was determined within the linear region of the stress-strain curve across 5-15% GelMA and 2% HA/2% PEGDA.

Immunofluorescence Staining and Imaging for the Assessment of NMVC morphology

Constructs with encapsulated NMVCs were fixed in 4% (v/v) paraformaldehyde in dPBS for 15 minutes at room temperature and subsequently blocked and permeabilized by 2% bovine serum albumin solution with 0.1% Triton X-100 for 1 hour at room temperature. Samples were incubated with primary antibodies against alpha-actinin, connexin-43, and/or vimentin overnight at 4^{o}C. Secondary antibody incubation, rhodamine-phalloidin, and nuclear counterstain were incubated subsequently at room temperature for 1 in dark. Confocal immunofluorescence images were acquired with 40X, 0.8 NA water-immersion objective lens attached to an Leica SP5 microscope to compare the cell morphology, and nuclear and sarcomere alignment in NMVCs. Directionality of sarcomeres and nuclei were analyzed using ImageJ Fourier components [103]. Assessment of proliferation between Ara-C treated and controls was determined by counting cell nuclei of positively stained NMVCs and non-NMVCs.

Force Measurements

To determine the force produced by the 3D-printed microtissues, three levels of printing were measured using the Cellscale Microsquisher: the 15% GelMA freestanding pillars, the tri-component scaffold without cells (acellular), and the tri-component scaffold with encapsulated NMVCs. The freestanding and acellular scaffolds were incubated at 37^{o}C 5% CO_2 in DPBS with 1% antibiotic 1% antimycotic. Samples were measured on day 1, 10, and 30, and placed on their sides and submerged in a dPBS bath at room temperature. Samples were pressed using a tungsten beam, measuring the point

of applied force from the base. Samples were displaced 20 μm and the force measured using equations 1 and 2 to calculate the sample modulus utilizing[85]:

$$\omega = \frac{F}{6\Upsilon I}(3Lx^2 - x^3) \ (3)$$

where ω is the displacement, F is the force, γ is the Young's Modulus, I is the 2nd moment of inertia (cuboid), L is the height, and x is the height of force application, where h=length and b =width.

$$I_{cuboid} = \frac{hb^3}{12} \ (4)$$

Lastly, NMVC encapsulated samples were submerged in a bath of Tyrode's solution without calcium and 40 mM 2,3 butedione monoxime (BDM) to relax the 3D-printed microtissues. Samples were pressed using a tungsten beam, measuring the point of applied force from the base. To determine the effect of cells within the scaffold, samples were displaced 20 μm and the force measured as previously described. Forces of the aligned tissue was calculated using equation 3 and 4, using the modulus of the cellular scaffolds.

Contributions:

Chapter 3, in part, is currently being prepared for submission for publication of the material. Liu J, Ma X, Dewan S, Lawrence N, Miller K Whang G, You S, Chung P, Chen S. Direct 3D BioPrinting of Cardiac Microtissues Mimicking Native Myocardium. The dissertation author was the primary investigator and primary author of this material.

Figures

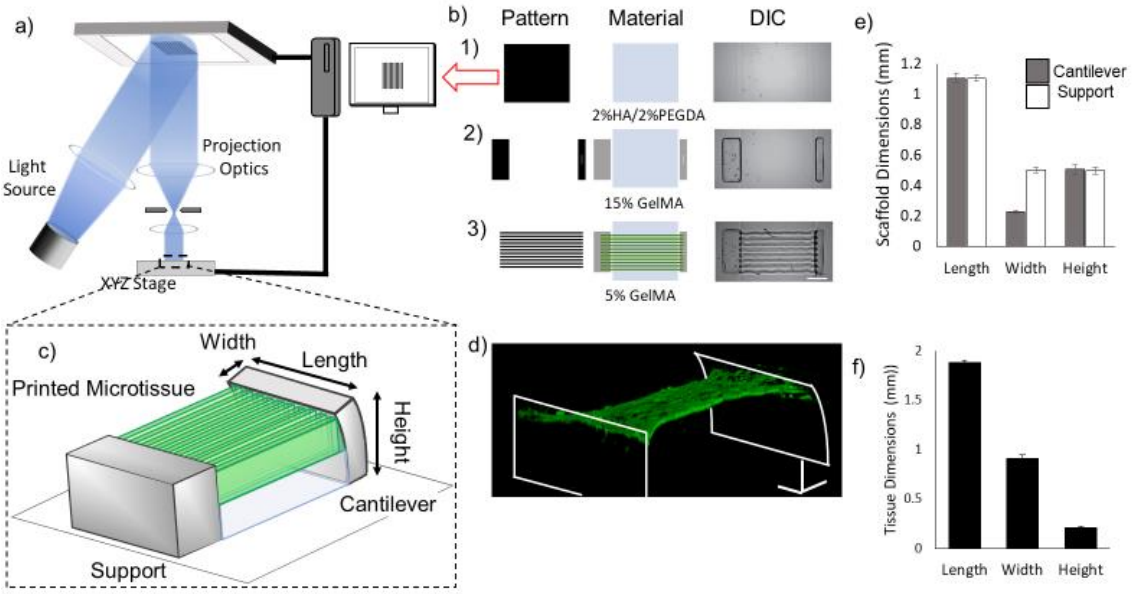

Figure 3.1: µCOP printing of a 3D cardiac tissue. a) Schematic of the µCOP printing system b) Mask-set and print order of 1) 2%HA/2% PEGDA 2) 15% GelMA 3) 5% GelMA/NMVC with DIC images (scale bar 250 µm) c) 3D schematic of full 3D tissue-measuring scaffold d) Dimensions of the supporting 15% GelMA pillars (scale bar is 200 µm) e) DIC images of scaffolds over 30 days, f) Confocal 3D reconstruction of NMVC cardiac tissue stained for actin (red) and nuclei (blue) across pillars

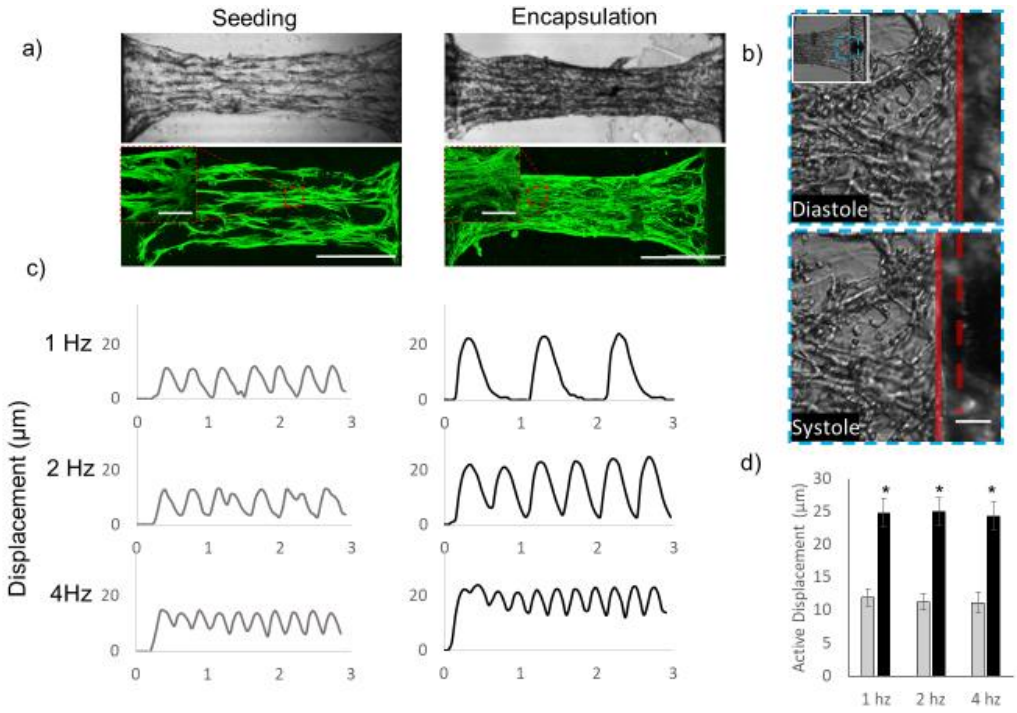

Figure 3.2: Comparison of the displacement of seeded and encapsulated NMVCMs tissues. a) DIC and fluorescent images of α-actinin stained for both scaffolds with seeded NMVCMs and encapsulated NMVCMs within the patterned gel at day 10 (scale bar is 500 µm, inlay is 25 µm) b) DIC image of the pillar showing its position at diastole (dotted red line) and at systole (solid red line), c) Displacement traces of seeded (left) and encapsulated (right) samples at various stimulating frequencies, d) and a summary of max displacement of seeded (gray) and encapsulated (black) samples (n=5, SEM, $p<0.005$)

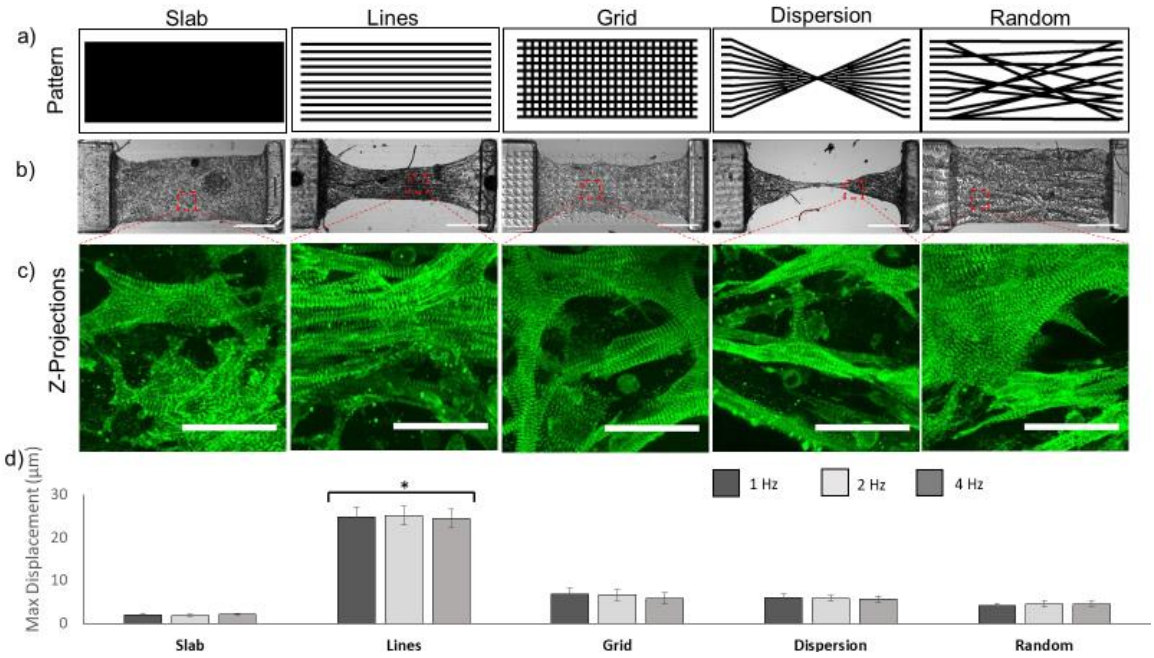

Figure 3.3: Micropatterning of cardiac tissue affects displacement. a) Masks of various complex patterns including (from left to right) slab, line, grid, dispersion, and random patterning. b) DIC images showing each patterned tissue at day 10 (scale bar is 500 µm) c) Fluorescent images of NMVCMS stained for α-actinin for each scaffold type showing alignment of sarcomeres (scale bar is 25 µm) d) Summary of max displacement for various patterned tissues at 1, 2, and 4 hz.

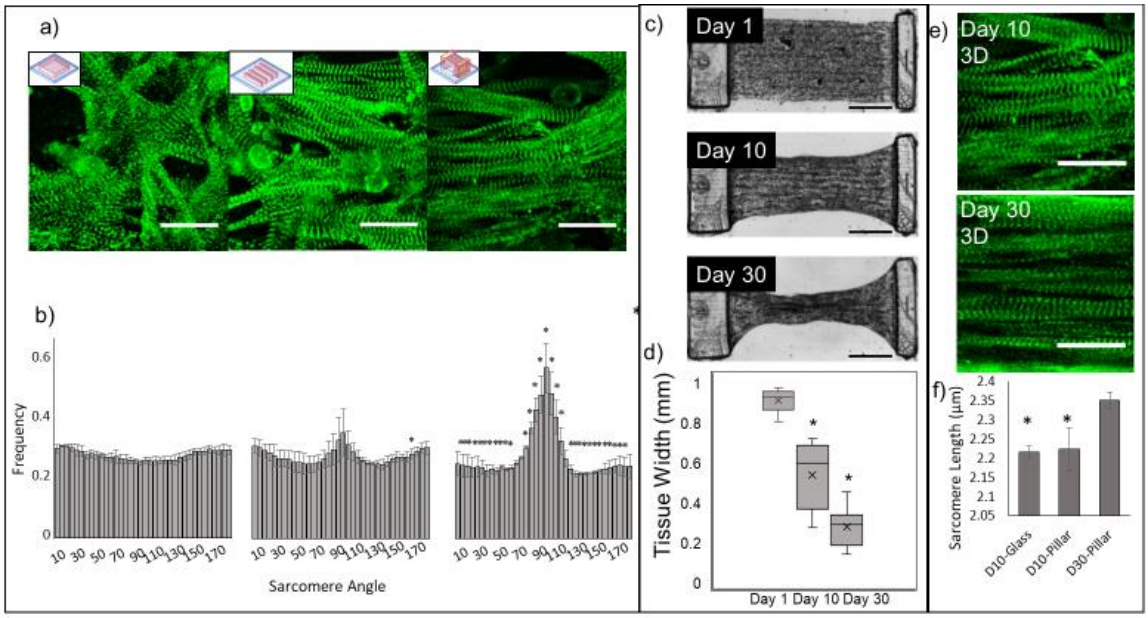

Figure 3.4: Characterization of sarcomere alignment, maturity, and tissue patterning. a) Representative images of α-actinin on day 10 of NMVCMs patterned in slab on glass, lines, on glass, and lines on between the 3D scaffold (left to right, scale bar 25 μm) and b) their respective sarcomere angle distributions Significance (one-tailed $p<0.05$ for day 10 lines and two-tailed $p<0.05$ for day 10 on scaffold) is denoted with asterisks when compared to slab. c) DIC images of full scaffolds and the compaction the tissue experiences over 30 days (scale bar is 100 μm). d) The tissue widths at the midpoint at day 1, 10 and 30 (SEM, paired two-tailed t-test, $p<0.001$, $n=14$). e) α-actinin stain of day 10 and day 30 samples (scale bar is 25 μm) and the average sarcomere lengths of NMVCMs aligned on glass at day 10, on the 3D scaffold at day 10, and the 3D scaffold on day 30 (SEM, $n=3$, $p<0.05$).

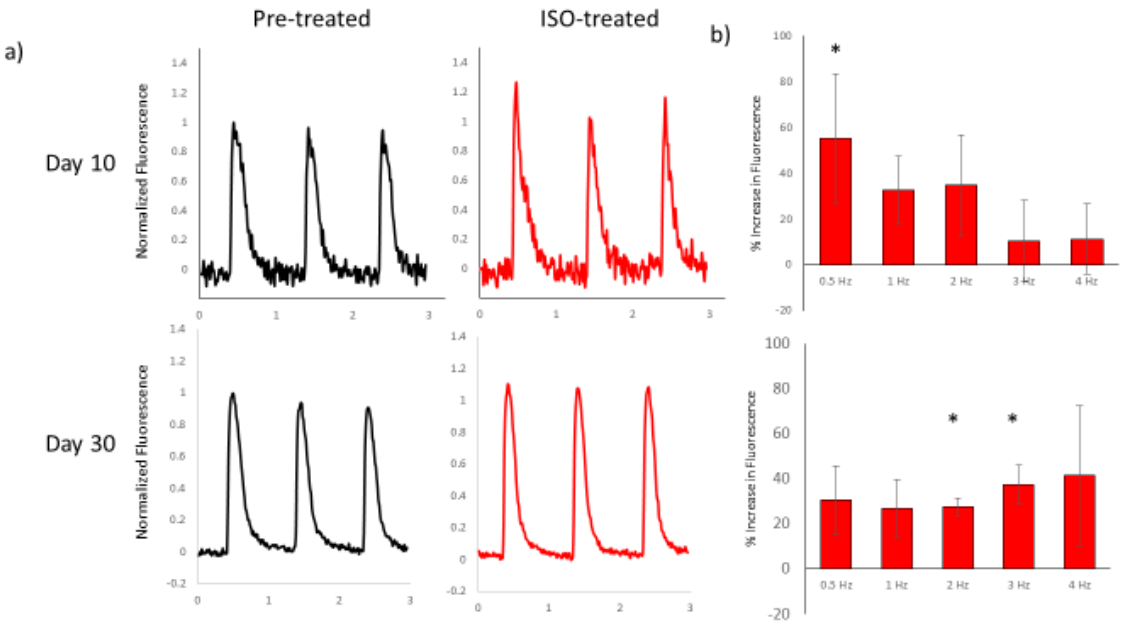

Figure 3.5: Calcium staining of NMVCM tissues. a) representative normalize fluorescence traces ΔF/Fo traces of day 10 (top) and day 30 (bottom) before (black) and after 100 nM ISO treatment (red). b) % increase in ΔF/Fo (asterisks denote significance) for day 10 (SEM, n=5 $p<0.05$) and day 30 sample (SEM, n=3 $p<0.05$)

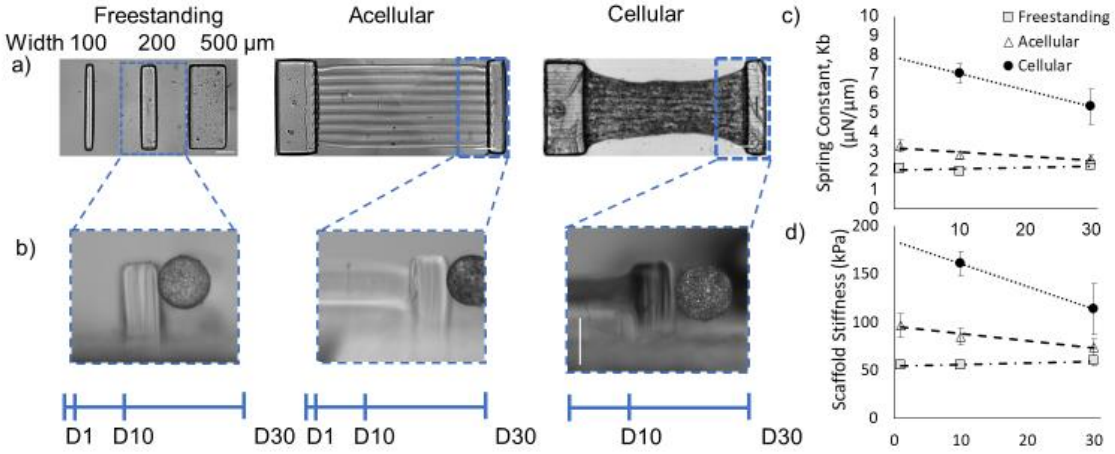

Figure 3.6: Mechanical testing of NMVCM tissue. a) Mechanical testing of free standing cantilevers, acellular scaffolds and cellular scaffolds, b) representative images the microsquisher pressing on each scaffold (scale bar is 500 µm) c) the spring constants of 200 µm pillars for free standing, acellular, and cellular scaffolds over 30 days. d) The calculated stiffness of each each 200 µm pillar scaffold over 30 days.

References:

[1] P.P. Sengupta, J. Korinek, M. Belohlavek, J. Narula, M.A. Vannan, A. Jahangir, B.K. Khandheria, Left Ventricular Structure and Function, J. Am. Coll. Cardiol. 48 (2006) 1988–2001.

[2] D.-H. Kim, E.A. Lipke, P. Kim, R. Cheong, S. Thompson, M. Delannoy, K.-Y. Suh, L. Tung, A. Levchenko, Nanoscale cues regulate the structure and function of macroscopic cardiac tissue constructs, Proc. Natl. Acad. Sci. 107 (2010) 565–570.

[3] X. Zong, H. Bien, C.-Y. Chung, L. Yin, D. Fang, B.S. Hsiao, B. Chu, E. Entcheva, Electrospun fine-textured scaffolds for heart tissue constructs, Biomaterials. 26 (2005) 5330–5338.

[4] P.W. Alford, A.W. Feinberg, S.P. Sheehy, K.K. Parker, Biohybrid thin films for measuring contractility in engineered cardiovascular muscle, 2010.

[5] Z. Ma, S. Koo, M.A. Finnegan, P. Loskill, N. Huebsch, N.C. Marks, B.R. Conklin, C.P. Grigoropoulos, K.E. Healy, Three-dimensional filamentous human diseased cardiac tissue model, Biomaterials. 35 (2014) 1367–1377.

[6] I.C. Turnbull, I. Karakikes, G.W. Serrao, P. Backeris, J.J. Lee, C. Xie, G. Senyei, R.E. Gordon, R.A. Li, F.G. Akar, R.J. Hajjar, J.S. Hulot, K.D. Costa, Advancing functional engineered cardiac tissues toward a preclinical model of human myocardium, FASEB J. 28 (2014) 644–654.

[7] A.C.C. van Spreeuwel, N.A.M. Bax, A.J. Bastiaens, J. Foolen, S. Loerakker, M. Borochin, D.W.J. van der Schaft, C.S. Chen, F.P.T. Baaijens, C.V.C. Bouten, The influence of matrix (an)isotropy on cardiomyocyte contraction in engineered cardiac microtissues, Integr. Biol. 6 (2014) 422–429.

[8] T. Boudou, W.R. Legant, A. Mu, M.A. Borochin, N. Thavandiran, M. Radisic, P.W. Zandstra, J.A. Epstein, K.B. Margulies, C.S. Chen, A Microfabricated Platform to Measure and Manipulate the Mechanics of Engineered Cardiac Microtissues, Tissue Eng. Part A. 18 (2012) 910–919.

[9] A. Agarwal, Y. Farouz, A.P. Nesmith, L.F. Deravi, M.L. McCain, K.K. Parker, Micropatterning Alginate Substrates for In Vitro Cardiovascular Muscle on a Chip, Adv. Funct. Mater. 23 (2013) 3738–3746.

[10] A. Grosberg, P.W. Alford, M.L. McCain, K.K. Parker, Ensembles of engineered cardiac tissues for physiological and pharmacological study: Heart on a chip, Lab Chip. 11 (2011) 4165.

[11] D. Zhang, I.Y. Shadrin, J. Lam, H.-Q. Xian, H.R. Snodgrass, N. Bursac, Biomaterials, Biomaterials. 34 (2013) 5813–5820.

[12] S.R. Shin, S.M. Jung, M. Zalabany, K. Kim, P. Zorlutuna, S.B. Kim, M. Nikkhah,

M. Khabiry, M. Azize, J. Kong, K.T. Wan, T. Palacios, M.R. Dokmeci, H. Bae, X.S. Tang, A. Khademhosseini, Carbon-nanotube-embedded hydrogel sheets for engineering cardiac constructs and bioactuators, ACS Nano. 7 (2013) 2369–2380.

[13] S.I. Fraley, Y. Feng, R. Krishnamurthy, D.-H. Kim, A. Celedon, G.D. Longmore, D. Wirtz, A distinctive role for focal adhesion proteins in three-dimensional cell motility, Nat. Cell Biol. 12 (2010) 598–604.

[14] E. Cukierman, R. Pankov, K.M. Yamada, Cell interactions with three-dimensional matrices, Curr. Opin. Cell Biol. 14 (2002) 633–639.

[15] X. Ma, X. Qu, W. Zhu, Y.-S. Li, S. Yuan, H. Zhang, J. Liu, P. Wang, C.S.E. Lai, F. Zanella, G.-S. Feng, F. Sheikh, S. Chien, S. Chen, Deterministically patterned biomimetic human iPSC-derived hepatic model via rapid 3D bioprinting, Proc. Natl. Acad. Sci. 113 (2016) 2206–2211.

[16] C.P. Soares, V. Midlej, M.E.W. de Oliveira, M. Benchimol, M.L. Costa, C. Mermelstein, 2D and 3D-Organized Cardiac Cells Shows Differences in Cellular Morphology, Adhesion Junctions, Presence of Myofibrils and Protein Expression, PLoS One. 7 (2012) e38147.

[17] S. V Murphy, A. Atala, 3D bioprinting of tissues and organs., Nat. Biotechnol. 32 (2014) 773–785.

[18] A. Atala, F.K. Kasper, A.G. Mikos, Engineering Complex Tissues, Sci. Transl. Med. 4 (2012) 160rv12--160rv12.

[19] A.P. Zhang, X. Qu, P. Soman, K.C. Hribar, J.W. Lee, S. Chen, S. He, Rapid fabrication of complex 3D extracellular microenvironments by dynamic optical projection stereolithography, Adv. Mater. 24 (2012) 4266–4270.

[20] P. Soman, P.H. Chung, A.P. Zhang, S. Chen, Digital microfabrication of user-defined 3D microstructures in cell-laden hydrogels, Biotechnol. Bioeng. 110 (2013) 3038–3047.

[21] J. Liu, H.H. Hwang, P. Wang, G. Whang, S. Chen, Direct 3D-printing of cell-laden constructs in microfluidic architectures, Lab Chip. 16 (2016) 1430–1438.

[22] W.R. Legant, A. Pathak, M.T. Yang, V.S. Deshpande, R.M. McMeeking, C.S. Chen, Microfabricated tissue gauges to measure and manipulate forces from 3D microtissues, Proc. Natl. Acad. Sci. 106 (2009) 10097–10102.

[23] A.J.S. Ribeiro, Y.-S. Ang, J.-D. Fu, R.N. Rivas, T.M.A. Mohamed, G.C. Higgs, D. Srivastava, B.L. Pruitt, Contractility of single cardiomyocytes differentiated from pluripotent stem cells depends on physiological shape and substrate stiffness., Proc. Natl. Acad. Sci. U. S. A. 112 (2015) 12705–10.

[24] S.S. Nunes, J.W. Miklas, J. Liu, R. Aschar-Sobbi, Y. Xiao, B. Zhang, J. Jiang, S.

Massé, M. Gagliardi, A. Hsieh, N. Thavandiran, M.A. Laflamme, K. Nanthakumar, G.J. Gross, P.H. Backx, G. Keller, M. Radisic, Biowire: a platform for maturation of human pluripotent stem cell–derived cardiomyocytes, Nat. Methods. 10 (2013) 781–787.

[25] D. Zhang, I.Y. Shadrin, J. Lam, H.-Q.Q. Xian, H.R. Snodgrass, N. Bursac, Tissue-engineered cardiac patch for advanced functional maturation of human ESC-derived cardiomyocytes, Biomaterials. 34 (2013) 5813–5820.

[26] H. Aubin, J.W. Nichol, C.B. Hutson, H. Bae, A.L. Sieminski, D.M. Cropek, P. Akhyari, A. Khademhosseini, Directed 3D cell alignment and elongation in microengineered hydrogels, Biomaterials. 31 (2010) 6941–6951.

[27] B.D. Fairbanks, M.P. Schwartz, C.N. Bowman, K.S. Anseth, Photoinitiated polymerization of PEG-diacrylate with lithium phenyl-2, 4, 6-trimethylbenzoylphosphinate: polymerization rate and cytocompatibility, Biomaterials. 30 (2009) 6702–6707.

[28] A.S. Maharjan, D. Pilling, R.H. Gomer, High and low molecular weight hyaluronic acid differentially regulate human fibrocyte differentiation., PLoS One. 6 (2011) e26078.

[29] F. Pati, J. Jang, D.-H. Ha, S. Won Kim, J.-W. Rhie, J.-H. Shim, D.-H. Kim, D.-W. Cho, Printing three-dimensional tissue analogues with decellularized extracellular matrix bioink, Nat. Commun. 5 (2014) 3935.

[30] L. Gao, M.E. Kupfer, J.P. Jung, L. Yang, P. Zhang, Y. Da Sie, Q. Tran, V. Ajeti, B.T. Freeman, V.G. Fast, P.J. Campagnola, B.M. Ogle, J. Zhang, Myocardial tissue engineering with cells derived from human-induced pluripotent stem cells and a native-like, high-resolution, 3-dimensionally printed scaffold, Circ. Res. 120 (2017) 1318–1325.

[31] N. Tsybouleva, L. Zhang, S. Chen, R. Patel, S. Lutucuta, S. Nemoto, G. DeFreitas, M. Entman, B.A. Carabello, R. Roberts, A.J. Marian, Aldosterone, through novel signaling proteins, is a fundamental molecular bridge between the genetic defect and the cardiac phenotype of hypertrophic cardiomyopathy., Circulation. 109 (2004) 1284–91.

[32] H.E. ter Keurs, W.H. Rijnsburger, R. van Heuningen, M.J. Nagelsmit, Tension development and sarcomere length in rat cardiac trabeculae. Evidence of length-dependent activation., Circ. Res. 46 (1980) 703–14.

[33] A.W. Feinberg, C.M. Ripplinger, P. Van Der Meer, S.P. Sheehy, I. Domian, K.R. Chien, K.K. Parker, Functional differences in engineered myocardium from embryonic stem cell-derived versus neonatal cardiomyocytes, Stem Cell Reports. 1 (2013) 387–396.

[34] D. Zhang, I.Y. Shadrin, J. Lam, H.-Q. Xian, H.R. Snodgrass, N. Bursac, Tissue-

engineered cardiac patch for advanced functional maturation of human ESC-derived cardiomyocytes., Biomaterials. 34 (2013) 5813–20.

[35] S. Pok, O.M. Benavides, P. Hallal, J.G. Jacot, Use of Myocardial Matrix in a Chitosan-Based Full-Thickness Heart Patch, Tissue Eng. Part A. 20 (2014) 1877–1887.

[36] M.N. Hirt, J. Boeddinghaus, A. Mitchell, S. Schaaf, C. Börnchen, C. Müller, H. Schulz, N. Hubner, J. Stenzig, A. Stoehr, C. Neuber, A. Eder, P.K. Luther, A. Hansen, T. Eschenhagen, Functional improvement and maturation of rat and human engineered heart tissue by chronic electrical stimulation, J. Mol. Cell. Cardiol. 74 (2014) 151–161.

[37] R. Gauvin, Y.C. Chen, J.W. Lee, P. Soman, P. Zorlutuna, J.W. Nichol, H. Bae, S. Chen, A. Khademhosseini, Microfabrication of complex porous tissue engineering scaffolds using 3D projection stereolithography, Biomaterials. 33 (2012) 3824–3834.

[38] J.W. Nichol, S.T. Koshy, H. Bae, C.M. Hwang, S. Yamanlar, A. Khademhosseini, Cell-laden microengineered gelatin methacrylate hydrogels, Biomaterials. 31 (2010) 5536–5544.

[39] S. Suri, L.-H. Han, W. Zhang, A. Singh, S. Chen, C.E. Schmidt, Solid freeform fabrication of designer scaffolds of hyaluronic acid for nerve tissue engineering., Biomed. Microdevices. 13 (2011) 983–93.

[40] E. Carrera, G. Giunta, M. Petrolo, Beam Structures, John Wiley & Sons, Ltd, Chichester, UK, 2011.

[41] Z.Q. Liu, Scale space approach to directional analysis of images., Appl. Opt. 30 (1991) 1369–1373.

Chapter 4: 3D Printing of human-derived stem cell cardiomyocytes for drug screening and *in vivo* studies.

Abstract:

The need for physiologically relevant 3D human scaffolds is of great need for both short-term, the development of drug testing platforms to screen new drugs across different genetic backgrounds, and longer term, the replacement of damaged or non-functional cardiac tissue after injury or infarction. In this study, I have designed and printed a variety of scaffolds for both *in vitro* diagnostics and *in vivo* implantation. For human stem cell-derived cardiomyocyte *in vitro* studies, two scaffolds were tested, one millimeter-scale scaffold previously described in chapter 3, a millimeter-scale cantilever scaffold, and an array of micron-scale cantilever scaffolds. Finally, direct printing of human embryonic stem cell derived cardiomyocytes were patterned into gelatin-based hydrogel materials to determine the ability of μCOP to serve as a means of rapidly generating transplantable scaffolds for future tissue repair.

Introduction:

Cardiovascular disease (CVD) is well recognized as the leading cause of death worldwide, attributing 32% of global deaths to CVD[104]. The majority of deaths are attributed to ischemic heart disease (IHD). Current treatments of IHD can only delay the progression of the disease. Thus, there is significant need to develop new strategies to replace injured or damaged myocardium. Over the past decades, human embryonic stem cells (hESCs) have offered opportunities of repairing damaged organ such as heart[105],

especially for the patients suffering loss of functional cardiomyocytes. hESCs have been extensively studied and their robust differentiation towards cardiomyocyte lineages (hESC-CMs) have been well established [14,106]. More recently the discovery of human induced pluripotent stem cell (hiPSCs) [107] and their differentiation to cardiomyocytes [108] has been of great interest to investigate disease[109,110] and the effects of drugs on different populations [109,111]. Although the strategies for generating cardiomyocytes from stem cells, maturation eliciting physiological response and how to improve the survival of the engraftments remains a concern[112]. Potential strategies include alignment [51] and co-culture with endothelial cells [113]. However, stem-cell derived cardiomyocytes are still in state of research where obtaining quality cells is both time consuming and resource intensive to differentiate with limited ability to proliferate once differentiated, a means of creating several 3D microtissues that elicit physiological responses is necessary.

Three-Dimensional (3D) Printing has been more recently used to produce cell-laden 3D tissues [59,64]. Digital Light-based 3D bioprinting has emerged as the next-generation of 3D printing technology, offering superior speed, resolution, flexibility and scalability[60,63,114], producing millimeter-scale 3D architectures with micron-resolution. Modified, naturally-based polymers, including gelatin[115] and hyaluronic acid [102] and synthetic PEGDA [114] can be photo-crosslinked using this light-based methods, exposing a whole area, rather than a single point, to produce a scaffold.

In this chapter, I will focus on the adaptation of the µCOP system towards a humanized model, along with alterations in printing scale for various *in vitro* and *in vivo* studies. The system was optimized to encapsulate hESC-CMs into GelMA hydrogels,

validating the previous direct-print method in chapter 3. Next, a set of microwells and micropillars were printed that will allow eight simultaneous human cardiac microtissues to form. Finally, hESC-CMs will be encapsulated in line and slab patterns and implanted into an animal model to determine if patterned cells improve survivability of the scaffold.

Results

3D direct printing of embryonic stem cell-derived cardiomyocyte in patterned hydrogel

hESC-CMs were successfully encapsulated in patterned 5% GelMA slabs and line patterns (see figure 1a). To ensure cell-cell contact of ESC-CMs within the gel, cell concentrations were increased to 40 million cells/mL from 30 million cells/mL with NMVCMs. Scaffolds were treated with a pro-survival cocktail with 20% FBS and incubated for 10 minutes at 37^{o}C and the PSC replaced to neutralize any remaining trypsin from cell dissociation. At lower concentration i.e. 10% FBS, or without replacing the media once, the scaffolds would be digested. Individual hESC-CMs were observed to beat as early as 24 hours after replacing the PSC with RPMI + B27 Supplement with insulin (RB+). Cells encapsulated in 5% GelMA slabs maintain ball-like aggregates at day 7, whereas patterned hESC-CMs elongate along the parallel lines, however there are still cell aggregates. Videos of patterned and slab constructs can be seen in supplementary videos 11 and 12. Isotropic slabs stained with calcein AM and ethidium homodimer show high viability (figure 1b), at 90.5 ± 0.5% viability (SEM, n=3) at day 3. Confocal images show hESC-CMs encapsulated in 5% GelMA lines and slab express α-actinin (green, figure 2b). Expression of α-actinin show cardiomyocyte-like cells, when merged with

actin show a significant portion of cells do not express both, suggesting that although they have a beating phenotype, are not mature.

I attempted to use hESC-CMs with a genetically encoded calcium indicator, green fluorescent protein, calmodulin, and myosin light chain kinase, M13 peptide sequence (GcaMP3) as an easier way of monitoring hESC-CMs when encapsulated in slab pattern and line patterns. GCaMP-hESC-CMs required an increased exposure time from 45 seconds to 60 seconds at the same cell density. DIC images and fluorescence images (in figure 2a) showing changes in brightness between diastole and systole are shown. Fluorescence traces (figure 2b) of a day 21 sample of encapsulated GcaMP-hESC-CMs treated with isoproterenol (ISO) increasing the average time between spontaneous beats from 2.72 ± 0.37 s (SD, n=3) to 1.93 ± 0.057 (SD, n=5) after treatment with 500 nM ISO and 1.96± 0.051 s (SD, n=5) with 1 μM ISO. Normalized fluorescence increased by 18± 6% after treatment with 500 nM ISO and 40 ± 5% when treated with 1 μM ISO. Therefore, these GCaMP-hESC-CMs could be a potential tool for calcium handling.

Cantilever scaffolds for 3D patterned hESC-CM tissue measurements

The scaffold designed in chapter 3 was printed using the μCOP system. However, since hESC-CMs are immature, the amount of force that they can generate is much smaller. Instead of 15% GelMA pillars, 10% GelMA pillars were printed with hESC-CMs encapsulated between in a line pattern. A sample of hESC-CMs cultured for 21 days is shown in figure 3a. The Young's Modulus of the pillar was measured on day 14 with the Cellscale Microsquisher to be 64±6 kPa (SEM, n=3), significantly lower than 15% GelMA scaffolds at 85 ± 9 kPa . The ESC-CM tissue displaced the small cantilever and a

representative displacement and force trace is shown in figure 3b. Using the acellular mechanical stiffness measurement, the average force produced by 3D printed hESC-CMs across the 3D scaffold was 6.5± 0.5 μN (SEM, N=4).

Green Fluorescent Protein/Calmodulin/M13 Peptide (GCaMP)-hESC-CMs were also printed across the cantilever system in a parallel pattern. These samples required an increase in exposure time of 60 seconds due to the expression of GCaMP. These samples were cultured for 21 days and spontaneous beats across the scaffold were recorded showing an increase in fluorescence between diastole and systole (figure 4d) with the corresponding normalized fluorescence trace show in figure 4e. Videos of spontaneous beats can be seen in supplementary video 13 (DIC) and supplementary video 14 (GCaMP). From edge traces, the pillar displaced up to 3.86 μm to a calculated maximum force of 6.8 μN (figure 4e). Thus, the designed human cardiac tissue model could be used to measure force and calcium simultaneously.

Micro-scale cantilever-based scaffolds for drug screening with iPSC-CM

I designed and printed an array of 500 μm tall micro-cantilevers in a well structure (see figure 5a) that can fit within a 96 well plate (figure 5b). The mask used for Micron-scale force measuring platform shown in figure 6c. The platform consists of 8 wells, with two asymmetric pillars in each. As previously mentioned in Chapter 1, the μCOP system allows the user to specifically designate when each pixel is turned on based of the color of the digital pattern, giving the user a significant amount of control when designing this mask. Areas marked in gray were turned on for first for 3 layers to create a base layer of PEGDA. This will help prevent cells from adhering to the floor of the well.

Next, the asymmetric pillars (in blue) are turned on for 10 layers from the bottom. Finally, the borders forming the wells (in black) are turned on and off in an alternating fashion for 50 layers. The red and green segments of the smaller pillar can be added to increase Young's Modulus for cell types with stronger active or passive forces.

This mask was highly refined to produce these small 3D-printed force gauges, with the smaller pillar measuring 40 μm wide, 100 μm long, and 500 μm tall. By turning on and off the black borders, over the course of the print prevents the polymerization of prepolymer solution within the well. Two images of wells printed without (top) and with (bottom) flipping the mirrors on and off are shown in figure 5c. To the right are the same wells cut with a razor, the cut marked with a red arrow. For the sample without the alternating pattern, a cut across the well can be observed. Although the well is transparent, this defect forms because it is fully polymerized, preventing cells from falling within the well. However, when the alternating pattern is used, the well is left open for cells to fill the volume.

iPSC-CMs mixed in a neutralized solution of rat tail collagen I and fibronectin are centrifuged into the wells, surrounding the micropillars (figure 5d). At day 3 the iPSC-CMs begin to remodel however are still in a very loose configuration. After 7 days, band of iPSC-CMs, wrapped around the pillars forming a microtissue and deflection of the micropillar can be observed. Two configurations, altering the distance between the two pillars were attempted (100 μm and 225 μm interpillar distance). iPSC-CMs stained for nuclei and α-actinin show that they were able to remodel around both scaffolds, however, iPSC-CMs seeded in 100 μm scaffolds had limited volume between the two pillars and the cells crossed over the center. iPSC-CMs seeded between 225 μm had improved

alignment. To test the mechanical properties of the micropillars a set of two pillars were printed longitudinally as the pillars in rows would interfere with the Microsquisher beam. The spring constant of the micropillars with iPSC-CMs seeded was 0.42 ±0.4 µN/µm and the modulus was calculated to be 2.74± 1.32 MPa.

Validation of the 3D micropillar array as a potential *in vitro* drug screening platform

iPSC-CMs were treated with one of three known drugs, Levosimendan (LEVO), Omecamtiv mecarbil (OM), and isoproterenol (ISO). The paired displacement and force traces are shown in red (figure 6a). The force produced by microtissues (figure 6b) were calculated by measuring the dimensions of the micropillars (figure 6c), which were 52.6± 1.68 and 111.9± 3.63 µm (SD, n=5). Microtissues treated with 1 µM LEVO increased from 0.93± 0.24 µN to 1.51 ± 0.46 µN (SEM, n=5, $p<0.05$). iPSC-CM microtissues recorded forces treated with 200 nM OM increased from 1.67± 0.66 µN to 2.70 ± 1.3 µN (SEM, n=5). Lastly the force measured iPSC-CM microtissues treated with 100 nM ISO increased from 3.16± 1.51 µN to 4.39 ± 2.30 µN (SEM, n=5, $p<0.01$). The increase in force of paired samples treated with LEVO was 57 ± 14%, with OM, 43 ± 13%, and with ISO, 29 ± 7 %. These initial tests suggest that the micropillar scaffold is a potential platform for drug screening.

3D-patterned hESC-CM patch exhibits higher viability *in vivo*. 5% GelMA line and slab patterns with encapsulated hESC-CMs were cultured for 7 days after printing for this *in vivo* experiment. Lines and slab patches were implanted into the fat

pad of non-obese diabetic, severe combined immunodeficiency (NOD/SCID) mice (n=6). Two weeks after implantation, patches were harvested and cryo-sectioned for immunofluorescence staining. To inspect the viability of hESC-CMs encapsulated in 5% GelMA lines and slab 5% GelMA hydrogels, Nkx2-5 positive staining revealed the survival cardiomyocytes on day 7 and day 14. Notably, from figure 7a we observed patterned exhibited stronger Nkx2-5 staining. These results strongly suggest that patterning can improve the viability of printed cells but also enhance the interaction of patches and host tissue. The relative fluorescence of NKX2.5 expressed by pattern was greater than 2x that of slab (figure 7b, SEM, n=6, $p<0.05$).

hESC-CMs and human vascular endothelial cells (HUVECs) were selectively printed in a 3-step print with 5% GelMA and 2.5% GelMA/1% HA with the HUVECs printed in a 100 μm wide line for every 200 μm of hESC-CMs printed. After 1 day, the 2.5% GelMA/1% HA lines would swell and compact the hESC-CMs between them. A video of a patterned multimaterial, multi-cell scaffold cultured for 14 days can be seen in supplementary video 15. Samples of thick tissues with or without HUVECs in lines were implanted in a subcutaneous pocket of a NOD/SCID mice (n=3) to observe their potential integration with host tissue, however the implanted scaffolds could not be found 7 days post implantation.

Discussion:

In this chapter, I focused on the 3D printing of human hESC-CMs and hiPSC-CMs. The discovery hESCs[116] and more recently iPSCs[107] and their respective differentiation protocols[106,108] have however they are still very immature. As in the

previous chapter, the ability to pattern and culture cells long term using encapsulated 3D hydrogels could be a significant tool in improving maturity of hESC-CMs and hiPSC-CMs and observing disease progression. Very few groups have utilized 3D printing to produce functional cardiac tissue, Currently, hESC-CMs printed on glass coverslips still have low expression of α-actinin (figure 1b) although a beating phenotype was observed (supplementary video 11). The morphology of hESC-CMs were not fully extended like previously seen for tissues printed with NMVCMs. Degradation of the scaffold was observed, much greater than with NMVCMs, suggesting the potential for a larger percentage of non-myocyte cells or immature cells within the culture that may be an imbalance of synthesis and degrading of the ECM proteins.

Preliminary data shown in this dissertation is the first instance of GCaMP-hESC-CMs being used in a 3D tissue setting [117,118]. The ability to detect electrical but not mechanical force, or visa versa maybe be especially useful for *in vitro* disease modeling or potentially serious side effects of drugs. For example, abnormal elevation of intracellular calcium has been reported in hiPSC-CMs derived from patients with hypertrophic cardiomyopathy with a *MYH7* mutation [18]. Several groups have adapted simple cantilever systems at the mm- scale producing 7 and 55 μN [80,119] of force. Adjusting for respective volumes, the prints hESC-CM tissue forces produced from this system are comparable. Thus, being able to pair the GcaMP sensor with the 3D printed cantilever system may be a powerful tool in determining how the calcium flux affects mechanical contractility and alternative mechanisms of disease development. Furthermore, using this system could find new methods of treating disease.

There have been efforts to upscale iPSC-CMs [120] to meet the need for a scalable system for differentiation and cardiomyocyte production by culturing embryoid bodies within spinner flasks. However, this system is still labor and resource intensive, with optimization required for each cell line. Thus, for most research groups, quantities of cells are still limited. With that in mind, it is highly desirable to developing a system that can have multiple replicates within a 96-well plate to maximize the number of samples produced from a batch of differentiated cardiomyocytes. Therefore, the set of micro-cantilevers where printed using the μCOP system may be able to reduce the number of cells required to validate drug responses to aligned human cardiomyocytes tissues. Of the engineered heart tissues within this scale, the Chen group at Boston University also creates PDMS molds with micropillar arrays [31] with tissues at the similar scale. hiPSC-CMs been used on their system[75], producing a force near 6 μN. Their tissue scaffold dimensions fall within the range of 400 x 200 x 100 μm (L x W x H), significantly larger than the microtissue dimensions presented in this micropillar array 225 x 100 x 100 μm (L x W x H).

The three drugs tested using the micropillar array, namely ISO, LEVO, and OM showed inotropic effects. Currently, 2D culture of iPSC-CMs leads to a false negative response to LEVO [121] and OM [122,123]. However, when treated within this 3D culture system, both drugs showed a positive inotropic effect (figure 7a) providing evidence that 3D culture may improve maturity and response to known drugs compared to 2D methods. As it stands the pillars may be too stiff at 2.7 MPa. Originally adapted from NMVCM culture, the micropillars may need to become thinner to allow the pillar to bend more, increasing the measuring resolution. This may be especially beneficial to

lower forces produced from negative inotropes drug treatment (i.e. verapamil, flecainide). By simply adjusting the mask dimensions the μCOP system would be able to achieve this.

At its current state, this 3D-printed drug screening platform is imaged using a 20x objective, allowing only one sample to be observed at a time. It can be cumbersome to image multiple samples in its current state. Compared to other micropillar[75] and thin film platforms[11], these can easily be translated to commonly used tissue culture plates and do not require extensive clean room experience. These samples could be printed directly within a glass-bottom 96-well plate using the μCOP printer and pairing this with an automated imaging system e.g. the Sony SI8000 Cell Motion Imaging System or other high-content analyzers. This could greatly increase throughput and determine the efficacy of this 3D platform to an array of drugs.

Finally, in this dissertation, I have attempted to use the μCOP system to print scaffolds large enough to graft within an animal model. In previous studies, there was no evidence of arrhythmia caused by engrafted hESC-CMs in in mice[124], rats [125], and guinea pigs [126]. However, more recently were found to produce arrhythmic events in non-human primates [127]. It has been hypothesized that this could be caused by reentrant loops or due to graft automaticity. Due to the increased size of the monkey heart, the grafts were larger and the immature hESC-CMs may slow conduction thus potentially creating a reentrant loop. Therefore, by looking towards patterning to improve conductivity and maturation [46] may be key in improving graft integration and restoration of function. The *in vivo* work presented in this dissertation is minimal, however the studies performed are an important step in moving 3D-printed scaffolds

towards determining their efficacy. By implanting in the fat pad, angiogenesis is minimal [128], thus the continued expression of NKX2.5 in patterned samples (figure 6b), although an early-stage marker, is promising. Further analysis of maturity is required by analyzing maturity markers like α-actinin and connexin-43.

I have prepared some multilayer prints creating a thick (750 μm) spatially patterned scaffolds, co-culturing hESC-CMs and HUVECs. Robust beating could be observed *in vitro* on day 14 (supplementary video 15). Our lab has previously shown that by spatially patterning cells, the appearance of lumen-like structures and red blood cells within the scaffold along with integration of mouse-specific lectin within the scaffold [59]. Unfortunately, these were disappeared subcutaneously. There will be continued work with collaborators to study the survivability and integration of these multi-step print using μCOP with host tissue and it's potential to improve organ function after injury.

Ultimately, μCOP and aligned 3D-printed cardiac tissue may be a powerful tool in drug discovery, drug safety, and potentially tissue regeneration. Already this work can show an improvement in function *in vitro* and potentially *in vivo* models. Patient- to-patient variation in pluripotency potential and batch-to-batch and variation of differentiated cells [129,130] are currently major hurdles in translating stem cell technologies for drug discovery models and tissue regeneration and restoration of function. Further work in maturing these tissues will be required via long-term culture and the investigation of spatial patterning of multi-cellular (cardiac fibroblast, endothelial, cardiomyocytes) tissues may aid in this.

Methods:

Differentiation of hESC-CMs Cardiomyocytes

Before differentiation, hESCs were dissociated into single cells by TrypLE and seeded onto the human ES qualified Matrigel substrate coated 6-well plates. When ESCs reached 90%-100% confluence, cardiomyocyte differentiation was initiated according to the protocol reported before with some modifications [106]. Briefly, hESCs were cultured in Hepes-buffered RPMI 1640 (Gibco) supplemented with 10 μM CHIR99021 and 2% (vol/vol) B27 minus insulin supplement. The following day medium was changed to HEPES-buffered RPMI 1640 supplemented with 2%(vol/vol) B27 minus insulin (RB-) supplement only. On day 3, the medium was changed to HEPES-buffered RPMI 1640 supplemented with 5 μM IWP4, 2%(vol/vol) B27 minus insulin supplement. On day 5, medium replaced with RB- media. From day 7 on, cells were maintained in HEPES-buffered RPMI 1640 supplemented with 2% (vol/vol) B27 supplement with insulin. Medium was changed every 48 hours. A separate H7 cell line was created with knock-in expression of GCaMP3 following previously recorded methods[131].

Integration-free Human Induced Pluripotent Stem Cells (iPSCs) Generation and Culture

The generation method of human iPSCs was carried out as previously reported [132]. Briefly, human perinatal foreskin fibroblasts and human adult dermal fibroblasts were purchased and maintained in DMEM supplemented with 10% Fetal Bovine and Antibiotics/Antimycotic in a 37°C, 5%CO_2 incubator. Cells were passaged at a ratio of 1:6 every 3-5 days by 0.25% Trypsin-EDTA before reprogramming. To prepare for

reprogramming, fibroblasts were seeded at a density of 2 x 10^5 cells/well in 6-well plates, and allowed to attach and spread for 48h. Reprogramming was performed following the instructions in a Sendai virus-based Cyto Tune kit for the delivery of four factors Oct4, Sox2, Klf4 and c-Myc.

Following successful reprogramming, Matrigel® Growth Factor Reduced (GFR) Basement Membrane Matrix was used as the substrate for the maintenance of the iPSCs culture in xeno-free and feeder-free Essential 8™ medium following the manufacturer's instructions. Cells were split at a ratio of 1:8 every 3-4 days by before experiments.

In vitro hiPSC Cardiac Differentiation

Before the initiation of cardiac differentiation, human iPSCs were dissociated into single cells by using Accutase and plated onto hESC-qualified Matrigel substrate (Corning) coated 12-well plates. The seeded plates were incubated at 37^{o}C with 5% CO_2. The seeding density was controlled to achieve 80% to 90% confluency within the following three days.

The cardiac differentiation was carried out using PSC cardiomyocyte differentiation kit. Briefly, human iPSCs were incubated in cardiomyocyte differentiation medium A for the first two days, followed by another two-day incubation in cardiomyocyte differentiation medium B at 37^{o}C, ambient O_2 with 5% CO_2. Subsequent incubation in cardiomyocyte maintenance medium for 8 days with medium change every other day was carried out. Spontaneous contraction of cell was observed starting day 8 to 9 of differentiation. Cardiomyocyte purification was carried out on day 12 of differentiation by incubating cells for 6 days in RPMI1640 medium without glucose, which was supplemented with 4mM lactate. Medium change was performed every other

day during purification process. Following six-day incubation in medium without glucose, cells were incubated for another 7 to 10 days in RB+ media.

Prepolymer solution preparation

Gelatin methacrylate (GelMA) was prepared per previously described methods [63]. Synthesized GelMA was frozen and lyophilized and stored at -80^{o}C until needed. Lithium 2,4,6 bisphenolphosphinate (LAP) was prepared via Michaelis-Arbuzov reaction method [84]. Hyaluronic acid glycidyl methacrylate (HAGM) was prepared via modified methods [102] 1g of HA (200 kDa) was dissolved in a 100 mL solution of 50:50 acetone:water stirring overnight. 1.8 mL of TEA was added dropwise and allowed to mix thoroughly following 1.8 mL of glycidyl methacrylate added dropwise. The solution reacted overnight and then transferred to 3500 kDa dialysis tubing and dialyzed for 48 hours, replacing the water 3 times a day. Dialyzed solution was frozen and lyophilized. Prepolymer solutions prepared for these projects included 10% GelMA/0.2%LAP in DPBS, 5% GelMA/2% HA/0.2% LAP, 2% PEGDA MW 700/2% HAGM/0.2% LAP and stored at 4^{o}C in the dark.

µCOP encapsulation of hESC-CMs in hydrogel

hESC-CMs were mixed 1:1 with a 10% GelMA/0.2% LAP to a final concentration of 40 million cells per mL in 5% GelMA/0.1% LAP. The cell mixture was placed between two 250 um spacers and a 3-(Trimethoxysilyl)propyl methacrylate (TMSPM)-treated coverslip. The sample is loaded on the µCOP printer and exposed to a digital mask for 40s. Non-crosslinked solution was rinsed away, and the samples were placed in a 24- well plate with PSC for 10 min at 37 ^{o}C, PSC replaced and cultured. PSC

consists of 100 mM benzyloxycarbonyl-Val-Ala-Asp(O-methyl)-fluoromethyl ketone (ZVAD), 50 nM cell-permeant TAT peptide, Bcl-XL BH4, 200 nM cyclosporine A, 100 ng/mL IGF-1, and 50 mM pinacidil with 20% FBS to neutralize trypsin from the cell preparation. After 24-hours, samples were replaced with RPMI 1640 with 2% B27 supplement with insulin (RB+). Media was replaced every two days until implantation or fixation.

3D printing of a scaffold for human millimeter-scale tissue measurements

Using the same line pattern as previously described in chapter 4, a 2 x 1 mm scaffold of encapsulated hESC-CMs were printed between two 500 µm tall pillars. However, in this case the 15% GelMA pillars were replaced with 10% GelMA and exposed for 29 seconds, per exposure time determined from chapter 2. hESC-CMs were washed in PSC for 10 minutes at 37^{o}C and the PSC was replaced for culture over 24 hrs. Media was replaced the following day with RB+ replaced every 48 hrs. Videos were taken as a series of TIFF images at 10x with 2 x 2 binning at 42 frames a second.

µCOP printing of micropillar array

A prepolymer solution of 40% PEGDA (MW:700)/0.2% LAP/0.2% 2-hydroxy-4-methoxybenzophenone-5-sulfonic acid (HMBS)/0.002% TEMPO and allowed to equilibrate for 48 hours at 4^{o}C. The solution was placed between a microscope slide and a methacrylated coverslip with 500 µm PDMS spacers. The base of the well is exposed for the first 3 of 50 layers, the micropillars for the first 10 of 50 layers, and the borders are alternated between on and off states for the whole 50 layers, totaling 25 layers. The entire

scaffold is exposed for 17 seconds, removed, placed in a 24-well plate, and rinsed in DPBS. Scaffolds were stored in 1% (v/v) normacin in DPBS and UV sterilized under the BSC hood for 30 minutes. Scaffolds were stored overnight and can be seeded up to week after printing.

iPSC-CMs were mixed 1:1 with a solution of 3 mg/mL collagen and 2 mg/mL fibrinogen and with a pipette tip, a 10 uL drop was placed on top of the scaffold. The samples were then centrifuged using an Eppendorf plate centrifuge for 3 min at 150 RCF. The interpillar distance was optimized by adjusting the distance in pixels on the mask. The mask used

Passive force caused by fibroblast overgrowth past day 3 could cause the micro-cantilever to break. To relieve some of the passive stress, samples were treated with 0.8 mg/mL collagenase for 5 min at 37^{o}C prior to measurements. Samples were measured on day 7 using an 20x objective on an Olympus inverted microscope with an Ionoptix MyoCam system. Using the provided Ionoptix Ionwizard software package live edge tracking of the micropillars based off changes in grayscale was used. High frequency noise was filtered using the provided filter and the traces were exported as TXT files for further analysis. Samples were stimulated across platinum electrodes placed within Tyrode's solution with 1.5 mM $CaCl_2$ using a Grass stimulator (70V, 0.3-1Hz stimulation). After control recordings were made, the Tyrode's solution was replaced with Tyrode's with 1 μM OM, 200 nM LEVO, or 100 nM ISO. Samples were incubated for 2 minutes before continuing recordings.

Maximum displacement of traces was measured using a custom MATLAB script that allowed users to first down-sampled the acquisition, split traces by stimulation

frequency, and then analyze the peak height of traces. Z-stack were acquired on an Invitrogen EVOS imaging system to determine the tissue height. The force was calculated using the Euler-Beam equation from Chapter 2.

In vivo implantation of 3D printed tissue

Nonobese diabetic (NOD)/Severe combined immunodeficiency (SCID) mice (Jackson Lab) were used for *in vivo* experiments. Briefly, mice were anesthetized by intraperitoneally injected a combination of Ketamin (8mg/ml) and Xylazin (1.2mg/ml). Then a low abdominal midline incision was made, and the fat pad was taken out. A small pocket was made by the scissors where the printed patch was gently placed [133]. Finally, the tissue was secured by Gelfoam™ (Pfizer). 2 weeks after implantation, mice were sacrificed, and the slab and patterned scaffolds were taken out for further evaluation.

Immunofluorescence preparation and imaging

*In vitro and in vivo s*amples excised on day 7 and day 14 after implantation and fixed in 4% paraphformaldehyde (PFA) in PBS for 15 minutes. Samples were rinsed three times and incubated in PBS for 5 minutes. Samples were then permeabilized with 0.3% Triton-X 100 in 5% bovine serum albumin (BSA) in PBS, and counterstained for either human NKX2-5(1:100) and α-actinin(1:100) or just α-actinin(1:100). Samples were washed three times with PBS and counterstained with two secondary antibodies, serially,488 nm anti-donkey anti-mouse (1:200) and 647 nm anti-donkey anti-rabbit (1:200) in a 0.1% Triton-X, 1% BSA in PBS solution with Hoescht nuclear stain

(1:2000). Samples stained with just α-actinin were also stained with 647-phalloidin (1:200). Confocal microscopy images were obtained using a Leica SP5 microscope.

Contributions:

Chapter 4, in part, contains material being prepared for submission for the publication of the material. Ma X, Liu J, Dewan S, Lawrence N, Miller K, Chen S. 3D Printed microcantilevers for human cardiac drug screening. The dissertation author was the secondary investigator and secondary author of this material. Chapter 4, in part, also is currently being prepared for submission for publication of the material. Liu J, Liu J, He J, Ma X, Chen Q, Lawrence N, Zhu W, Xu Y, Chen S. Rapid Printing of Human Cardiomyocytes in 3D Hydrogel. The dissertation author was the primary investigator and primary author of this material.

Figures

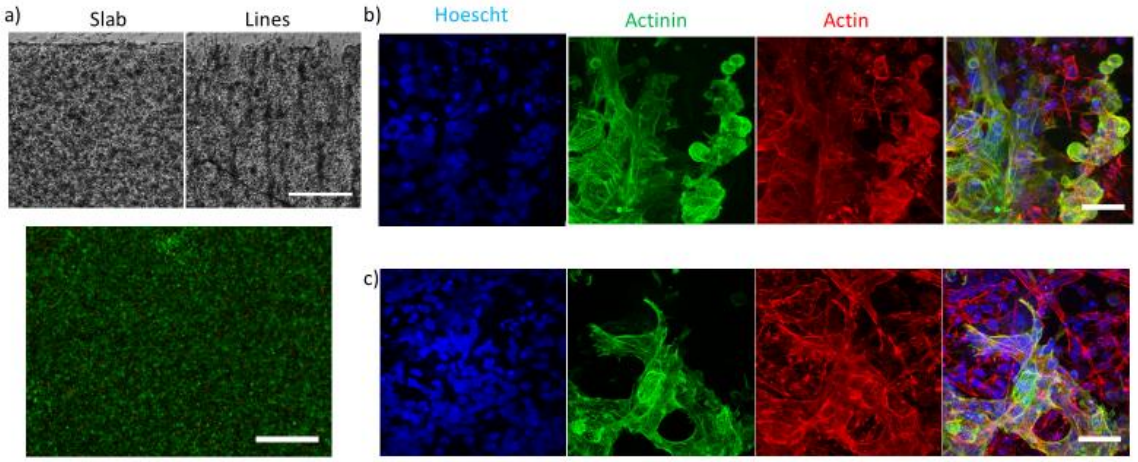

Figure 4.1: µCOP printing of hESC-CMs in GelMA hydrogels (scale bar is 125 µm) . a) DIC images of patterned hESC-CMs in slab and line patterns. b) Live/dead images of hESC-CMs (scale bar is 500). c) Z-projections of encapsulated hESC-CMs in line (top) and slab (bottom) pattern. Samples were stained for nuclei (blue), α-actinin(green), and actin(red). Scale bar is 50 µm.

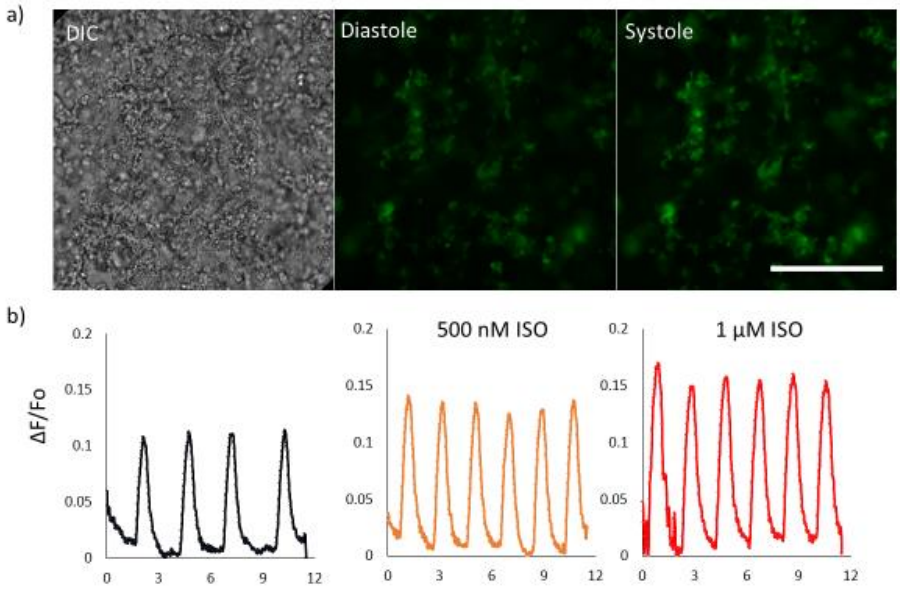

Figure 4.2: Encapsulation of GCaMP- modified hESCMs. a) A DIC and fluorescent image of GCAMP-hESCMs printed in a line patten. b) Normalized fluorescence of the scaffold after treatment with 500 nM and 1 µm ISO. Scale bar is 250 µm.

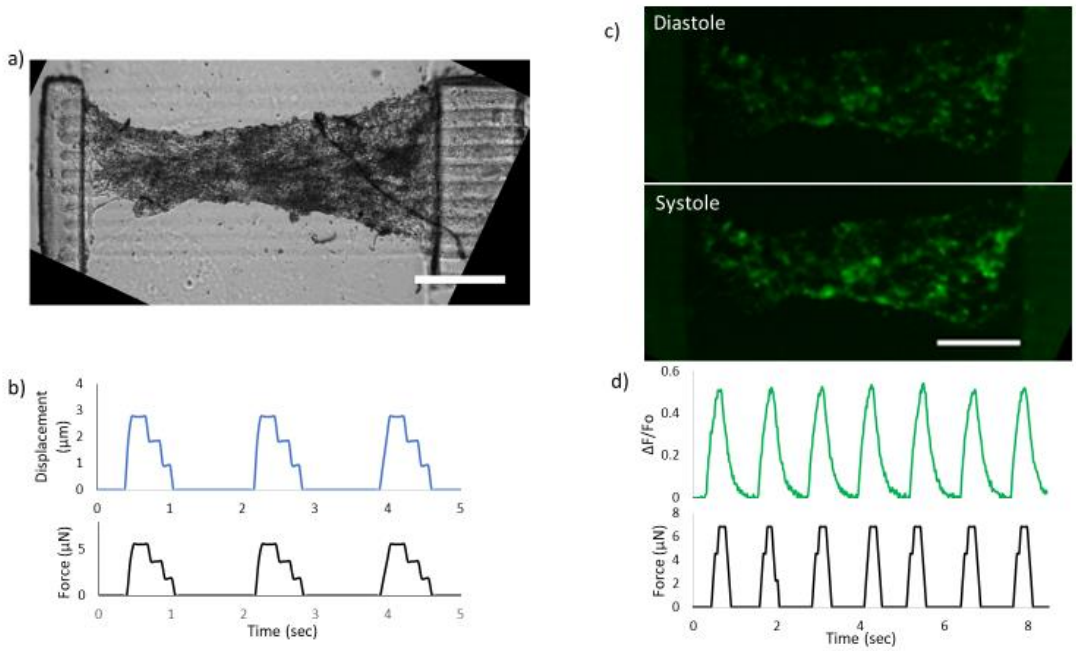

Figure 4.3: 3D-printed force gauge to measure hESC-CMs force generation. a) Cultured hESC-CMs encapsulated in a line pattern. b) edge traces from a video recording of the pillar displacing as the tissue contracts and the calculated force. c) Fluorescent images of GCaMP-hESC-CMs printed between forces gauges during diastole (top) and systole (bottom) and d) the normalized fluorescence and force traces for the scaffold. Scale bars are 500 µm.

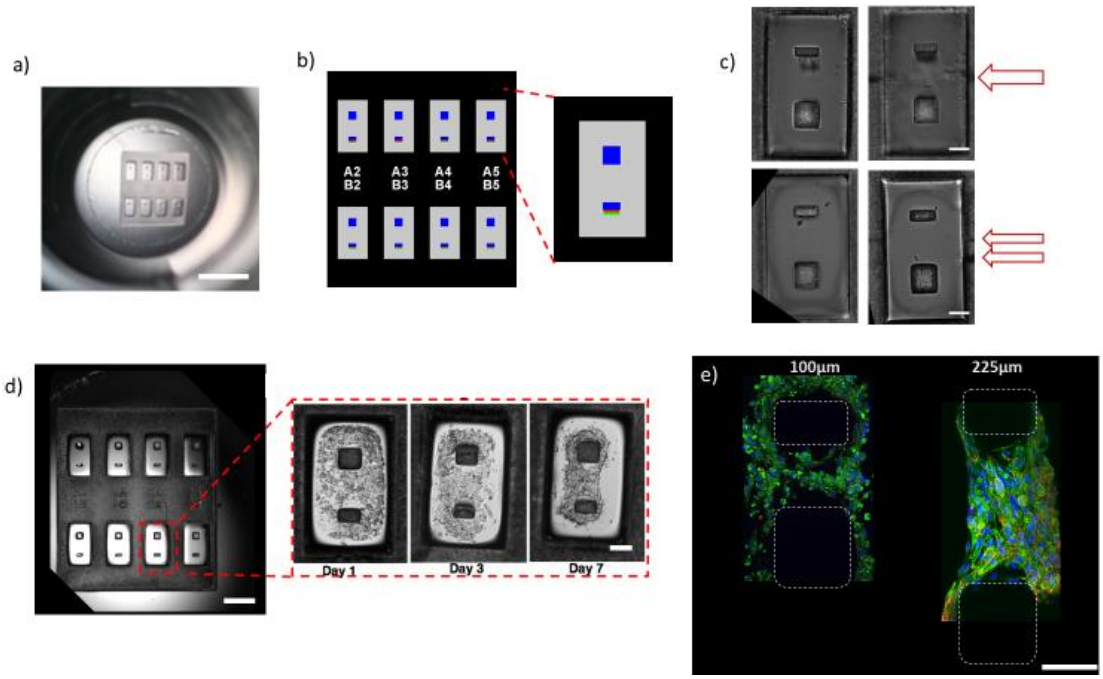

Figure 4.4: Micropillar scaffolds for higher throughput screening (scale bar is 2 mm). a) An 8-well scaffold within a 96-well plate, with printed micropillars. b) The RGB pattern used to print the scaffold with an inlay showing greater detail of a single well. C) Micropillar prints without (top) and with (bottom) alternating printing with before (left) and after cutting (right), marked with red arrows. A cut across the entire scaffold can be seen on the top microwell, whereas it is clean on the bottom scaffold. d) Image of the entire scaffold with hiPSC-CM remodeling over 7 days shown in the inlay(scale bar is 250 µm, inlay 125 µm). (scale bar is 125 µm). e) hiPSC-CMs seeded in both wells with pillars100 µm and 225 µm away from each other. Cells are counterstained for nuclei (blue), α-actinin (green), and connexin-43 (red) (scale bar is 125 µm).

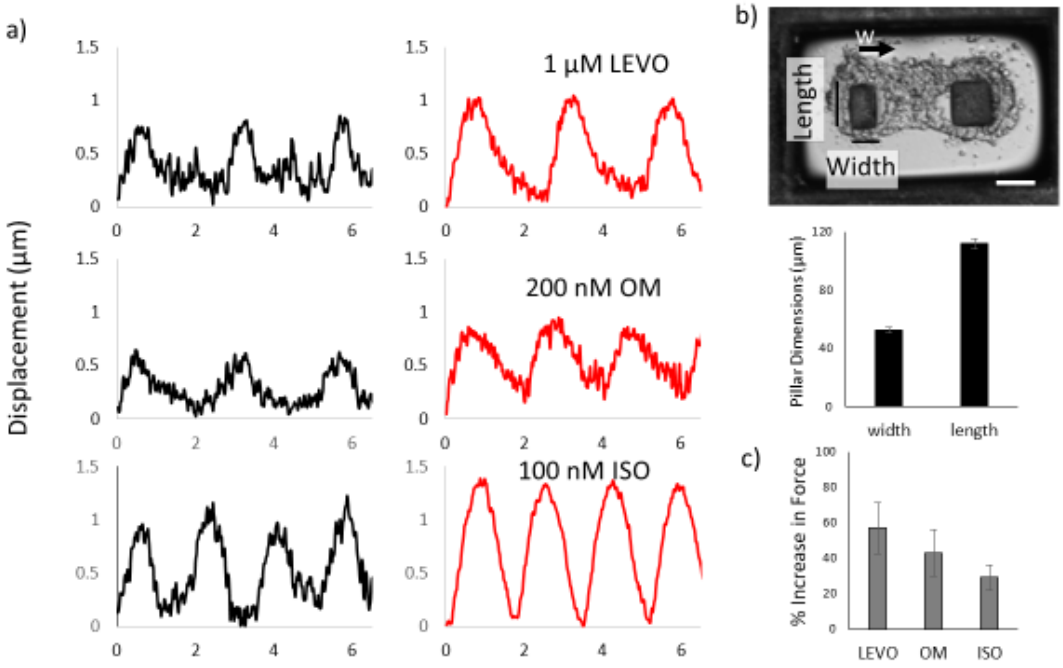

Figure 4.5: Functional maturity based on response to small molecules. a) Displacement traces of pillars before (left, black) and after drug treatment (right, red). b) Pillar dimensions corresponding to the pillar geometry. Scale bar is 125 µm. c) Percent increase in force produced by paired samples (SEM, n=5).

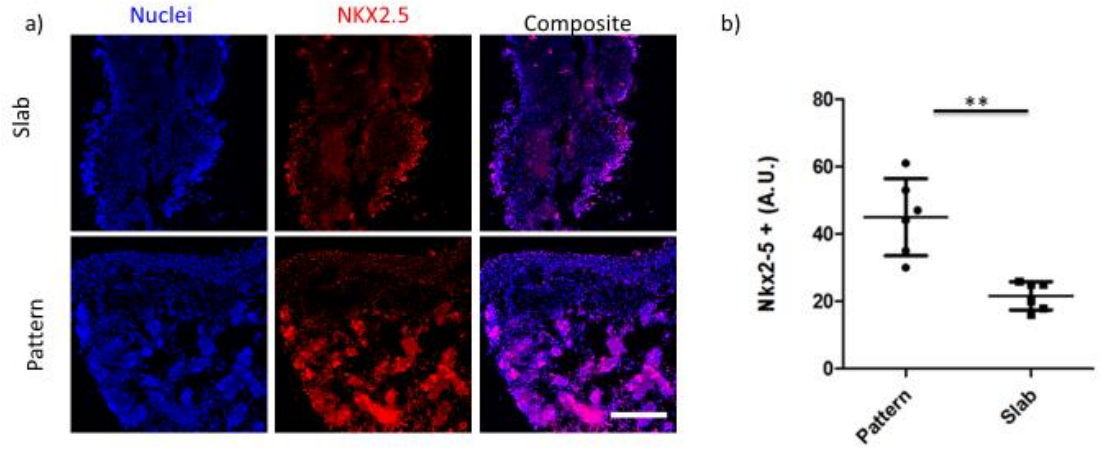

Figure 4.6: Implantation of 3D-printed scaffolds in fat pad of mice. a) Confocal images of scaffold sections stained for nuclei (blue) and transcription factor NKX2.5 (red). Scale bar is 250 µm. b) Average fluorescence of NKX2.5 in regions stained by nuclear stain (SD $p<0.05$, $n=5$).

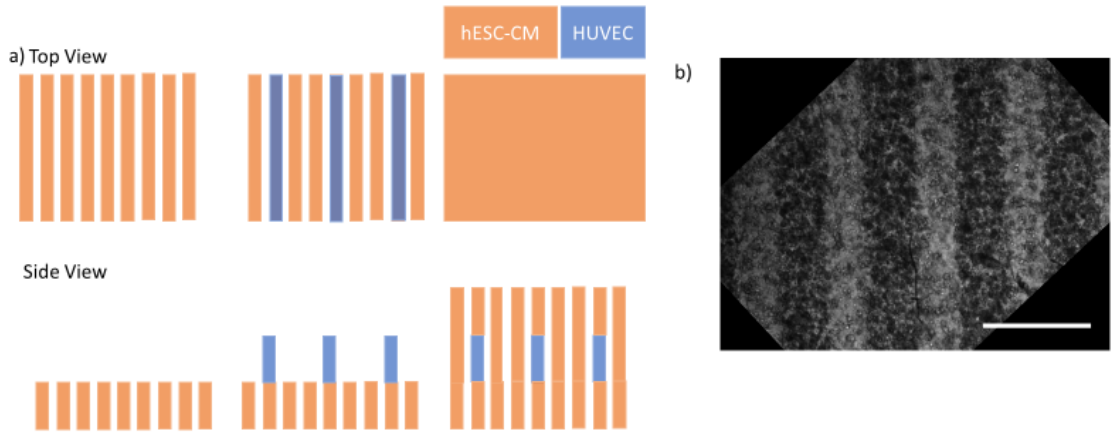

Figure 4.7: Multistep print of a thick spatially, spatially patterned tissue consisting of localized HUVECs and hESC-CMs. a) A schematic of the proposed scaffold print, consisting of a 250 µm tall set of parallel lines (50 µm wide, 50 µm spacing) made of 5% GelMA with 40 million hESC-CMs/mL (left). The second print consists of 250 µm tall 50 µm wide lines comprised of 2.5% GelMA/1%HA and 10 million HUVECs/mL. Finally, the same print as the first, however, in some instances the lines go below second layer and crosslink with the first. b) DIC image of spatially patterned HUVECs and hESC-CMs for vascularization and host integration studies.

References:

[1] G.A. Roth, M.D. Huffman, A.E. Moran, V. Feigin, G.A. Mensah, M. Naghavi, et al., Global and regional patterns in cardiovascular mortality from 1990 to 2013, Circulation. 132 (2015) 1667–1678. doi:10.1161/CIRCULATIONAHA.114.008720.

[2] V.F.M. Segers, R.T. Lee, Stem-cell therapy for cardiac disease, Nature. 451 (2008) 937–942. doi:10.1038/nature06800.

[3] H. Song, S.K. Chung, Y. Xu, Modeling Disease in Human ESCs Using an Efficient BAC-Based Homologous Recombination System, Cell Stem Cell. 6 (2010) 80–89. doi:10.1016/j.stem.2009.11.016.

[4] X. Lian, C. Hsiao, G. Wilson, K. Zhu, L.B. Hazeltine, S.M. Azarin, et al., Cozzarelli Prize Winner: Robust cardiomyocyte differentiation from human pluripotent stem cells via temporal modulation of canonical Wnt signaling, Proc. Natl. Acad. Sci. 109 (2012) E1848–E1857. doi:10.1073/pnas.1200250109.

[5] K. Takahashi, S. Yamanaka, Induction of Pluripotent Stem Cells from Mouse Embryonic and Adult Fibroblast Cultures by Defined Factors, Cell. 126 (2006) 663–676. doi:10.1016/j.cell.2006.07.024.

[6] K. Takahashi, K. Tanabe, M. Ohnuki, M. Narita, T. Ichisaka, K. Tomoda, et al., Induction of Pluripotent Stem Cells from Adult Human Fibroblasts by Defined Factors, Cell. 131 (2007) 861–872. doi:10.1016/j.cell.2007.11.019.

[7] I.Y. Chen, E. Matsa, J.C. Wu, Induced pluripotent stem cells: at the heart of cardiovascular precision medicine, Nat. Rev. Cardiol. 13 (2016) 333–349. doi:10.1038/nrcardio.2016.36.

[8] N. Sun, M. Yazawa, J. Liu, L. Han, V. Sanchez-Freire, O.J. Abilez, et al., Patient-Specific Induced Pluripotent Stem Cells as a Model for Familial Dilated Cardiomyopathy, Sci. Transl. Med. 4 (2012) 130ra47-130ra47. doi:10.1126/scitranslmed.3003552.

[9] E. Matsa, P.W. Burridge, K.-H. Yu, J.H. Ahrens, V. Termglinchan, H. Wu, et al., Transcriptome Profiling of Patient-Specific Human iPSC-Cardiomyocytes Predicts Individual Drug Safety and Efficacy Responses In Vitro, Cell Stem Cell. 19 (2016) 311–325. doi:10.1016/j.stem.2016.07.006.

[10] D.J. Mooney, H. Vandenburgh, Cell Delivery Mechanisms for Tissue Repair, Cell Stem Cell. 2 (2008) 205–213. doi:10.1016/j.stem.2008.02.005.

[11] L. Gao, M.E. Kupfer, J.P. Jung, L. Yang, P. Zhang, Y. Da Sie, et al., Myocardial tissue engineering with cells derived from human-induced pluripotent stem cells and a native-like, high-resolution, 3-dimensionally printed scaffold, Circ. Res. 120 (2017) 1318–1325. doi:10.1161/CIRCRESAHA.116.310277.

[12] H. Sekine, T. Shimizu, K. Hobo, S. Sekiya, J. Yang, M. Yamato, et al., Endothelial cell coculture within tissue-engineered cardiomyocyte sheets enhances neovascularization and improves cardiac function of ischemic hearts, Circulation. 118 (2008) S145–S152.

[13] X. Ma, X. Qu, W. Zhu, Y.-S. Li, S. Yuan, H. Zhang, et al., Deterministically patterned biomimetic human iPSC-derived hepatic model via rapid 3D bioprinting, Proc. Natl. Acad. Sci. 113 (2016) 2206–2211. doi:10.1073/pnas.1524510113.

[14] W. Zhu, X. Qu, J. Zhu, X. Ma, S. Patel, J. Liu, et al., Direct 3D bioprinting of prevascularized tissue constructs with complex microarchitecture, Biomaterials. 124 (2017) 106–115. doi:10.1016/j.biomaterials.2017.01.042.

[15] P. Soman, P.H. Chung, A.P. Zhang, S. Chen, Digital microfabrication of user-defined 3D microstructures in cell-laden hydrogels, Biotechnol. Bioeng. 110 (2013) 3038–3047. doi:10.1002/bit.24957.

[16] J. Liu, H.H. Hwang, P. Wang, G. Whang, S. Chen, Direct 3D-printing of cell-laden constructs in microfluidic architectures, Lab Chip. 16 (2016) 1430–1438. doi:10.1039/C6LC00144K.

[17] T.Q. Huang, X. Qu, J. Liu, S. Chen, 3D printing of biomimetic microstructures for cancer cell migration, Biomed. Microdevices. 16 (2014) 127–132.

[18] D. Loessner, C. Meinert, E. Kaemmerer, L.C. Martine, K. Yue, P.A. Levett, et al., Functionalization, preparation and use of cell-laden gelatin methacryloyl-based hydrogels as modular tissue culture platforms., Nat. Protoc. 11 (2016). doi:10.1038/nprot.2016.037.

[19] S. Suri, L.-H. Han, W. Zhang, A. Singh, S. Chen, C.E. Schmidt, Solid freeform fabrication of designer scaffolds of hyaluronic acid for nerve tissue engineering, Biomed. Microdevices. 13 (2011) 983–993. doi:10.1007/s10544-011-9568-9.

[20] J.A. Thomson, Embryonic Stem Cell Lines Derived from Human Blastocysts, Science (80-.). 282 (1998) 1145–1147. doi:10.1126/science.282.5391.1145.

[21] M. Maddah, J.D. Heidmann, M.A. Mandegar, C.D. Walker, S. Bolouki, B.R. Conklin, et al., A non-invasive platform for functional characterization of stem-cell-derived cardiomyocytes with applications in cardiotoxicity testing., Stem Cell Reports. 4 (2015) 621–31. doi:10.1016/j.stemcr.2015.02.007.

[22] N. Huebsch, P. Loskill, M.A. Mandegar, N.C. Marks, A.S. Sheehan, Z. Ma, et al., Automated Video-Based Analysis of Contractility and Calcium Flux in Human-Induced Pluripotent Stem Cell-Derived Cardiomyocytes Cultured over Different Spatial Scales, Tissue Eng. Part C Methods. 21 (2015) 467–479. doi:10.1089/ten.tec.2014.0283.

[23] F. Lan, A.S. Lee, P. Liang, V. Sanchez-Freire, P.K. Nguyen, L. Wang, et al.,

Abnormal calcium handling properties underlie familial hypertrophic cardiomyopathy pathology in patient-specific induced pluripotent stem cells., Cell Stem Cell. 12 (2013) 101–13. doi:10.1016/j.stem.2012.10.010.

[24] G. Kensah, A.R. Lara, J. Dahlmann, R. Zweigerdt, K. Schwanke, J. Hegermann, et al., Murine and human pluripotent stem cell-derived cardiac bodies form contractile myocardial tissue in vitro, Eur. Heart J. 34 (2013) 1134–1146. doi:10.1093/eurheartj/ehs349.

[25] Y. Morimoto, S. Mori, F. Sakai, S. Takeuchi, Human induced pluripotent stem cell-derived fiber-shaped cardiac tissue on a chip, Lab Chip. 16 (2016) 2295–2301. doi:10.1039/C6LC00422A.

[26] V. Chan, D.M. Neal, S.G.M. Uzel, H. Kim, R. Bashir, H.H. Asada, Fabrication and characterization of optogenetic, multi-strip cardiac muscles, Lab Chip. 15 (2015) 2258–2268. doi:10.1039/C5LC00222B.

[27] W.R. Legant, A. Pathak, M.T. Yang, V.S. Deshpande, R.M. McMeeking, C.S. Chen, Microfabricated tissue gauges to measure and manipulate forces from 3D microtissues, Proc. Natl. Acad. Sci. 106 (2009) 10097–10102. doi:10.1073/pnas.0900174106.

[28] J.T. Hinson, A. Chopra, N. Nafissi, W.J. Polacheck, C.C. Benson, S. Swist, et al., HEART DISEASE. Titin mutations in iPS cells define sarcomere insufficiency as a cause of dilated cardiomyopathy., Science. 349 (2015) 982–6. doi:10.1126/science.aaa5458.

[29] C.W. Scott, X. Zhang, N. Abi-Gerges, S.D. Lamore, Y.A. Abassi, M.F. Peters, An impedance-based cellular assay using human iPSC-derived cardiomyocytes to quantify modulators of cardiac contractility, Toxicol. Sci. 142 (2014) 331–338. doi:10.1093/toxsci/kfu186.

[30] A.J.S. Ribeiro, O. Schwab, M.A. Mandegar, Y.S. Ang, B.R. Conklin, D. Srivastava, et al., Multi-imaging method to assay the contractile mechanical output of micropatterned human iPSC-derived cardiac myocytes, Circ. Res. 120 (2017) 1572–1583. doi:10.1161/CIRCRESAHA.116.310363.

[31] L. Butler, C. Cros, K.L. Oldman, A.R. Harmer, A. Pointon, C.E. Pollard, et al., Enhanced characterization of contractility in cardiomyocytes during early drug safety assessment, Toxicol. Sci. 145 (2015) 396–406. doi:10.1093/toxsci/kfv062.

[32] A. Grosberg, P.W. Alford, M.L. McCain, K.K. Parker, Ensembles of engineered cardiac tissues for physiological and pharmacological study: Heart on a chip, Lab Chip. 11 (2011) 4165. doi:10.1039/c1lc20557a.

[33] T.E. Robey, M.K. Saiget, H. Reinecke, C.E. Murry, Systems Approaches to Preventing Transplanted Cell Death in Cardiac Repair, J Mol Cell Cardiol. 45 (2008) 567–581. doi:10.1016/j.yjmcc.2008.03.009.

[34] S. Fernandes, A. V. Naumova, W.Z. Zhu, M.A. Laflamme, J. Gold, C.E. Murry, Human embryonic stem cell-derived cardiomyocytes engraft but do not alter cardiac remodeling after chronic infarction in rats, J. Mol. Cell. Cardiol. 49 (2010) 941–949. doi:10.1016/j.yjmcc.2010.09.008.

[35] Y. Shiba, S. Fernandes, W.-Z. Zhu, D. Filice, V. Muskheli, J. Kim, et al., Human ES-cell-derived cardiomyocytes electrically couple and suppress arrhythmias in injured hearts, Nature. 489 (2012). doi:10.1038/nature11317.

[36] J.J.H. Chong, X. Yang, C.W. Don, E. Minami, Y.W. Liu, J.J. Weyers, et al., Human embryonic-stem-cell-derived cardiomyocytes regenerate non-human primate hearts, Nature. 510 (2014) 273–277. doi:10.1038/nature13233.

[37] D. Zhang, I.Y. Shadrin, J. Lam, H.-Q. Xian, H.R. Snodgrass, N. Bursac, Tissue-engineered cardiac patch for advanced functional maturation of human ESC-derived cardiomyocytes., Biomaterials. 34 (2013) 5813–20. doi:10.1016/j.biomaterials.2013.04.026.

[38] S. Corvera, O. Gealekman, Adipose tissue angiogenesis: Impact on obesity and type-2 diabetes, Biochim. Biophys. Acta - Mol. Basis Dis. 1842 (2014) 463–472. doi:10.1016/j.bbadis.2013.06.003.

[39] A. Kyttälä, R. Moraghebi, C. Valensisi, J. Kettunen, C. Andrus, K.K. Pasumarthy, et al., Genetic Variability Overrides the Impact of Parental Cell Type and Determines iPSC Differentiation Potential, Stem Cell Reports. 6 (2016) 200–212. doi:10.1016/j.stemcr.2015.12.009.

[40] M. Nishizawa, K. Chonabayashi, M. Nomura, A. Tanaka, M. Nakamura, A. Inagaki, et al., Epigenetic Variation between Human Induced Pluripotent Stem Cell Lines Is an Indicator of Differentiation Capacity, Cell Stem Cell. 19 (2016) 341–354. doi:10.1016/j.stem.2016.06.019.

[41] H. Masumoto, T. Ikuno, M. Takeda, H. Fukushima, A. Marui, S. Katayama, et al., Human iPS cell-engineered cardiac tissue sheets with cardiomyocytes and vascular cells for cardiac regeneration, Sci. Rep. 4 (2014). doi:10.1038/srep06716.

[42] L. Borges-Pereira, B.R.K.L. Campos, C.R.S. Garcia, The GCaMP3 - A GFP-based calcium sensor for imaging calcium dynamics in the human malaria parasite Plasmodium falciparum, MethodsX. 1 (2014) e151–e154. doi:10.1016/j.mex.2014.08.005.

[43] K.C. Hribar, D. Finlay, X. Ma, X. Qu, M.G. Ondeck, P.H. Chung, et al., Nonlinear 3D projection printing of concave hydrogel microstructures for long-term multicellular spheroid and embryoid body culture, Lab Chip. 15 (2015) 2412–2418. doi:10.1039/C5LC00159E.

[44] B.D. Fairbanks, M.P. Schwartz, C.N. Bowman, K.S. Anseth, Photoinitiated polymerization of PEG-diacrylate with lithium phenyl-2, 4, 6-

trimethylbenzoylphosphinate: polymerization rate and cytocompatibility, Biomaterials. 30 (2009) 6702–6707.

[45] S. Suri, L.-H. Han, W. Zhang, A. Singh, S. Chen, C.E. Schmidt, Solid freeform fabrication of designer scaffolds of hyaluronic acid for nerve tissue engineering., Biomed. Microdevices. 13 (2011) 983–93. doi:10.1007/s10544-011-9568-9.

[46] B. Kocatürk, H.H. Versteeg, Orthotopic Injection of Breast Cancer Cells into the Mammary Fat Pad of Mice to Study Tumor Growth., J. Vis. Exp. (2015) 1–8. doi:10.3791/51967.

Chapter 5: Discussion

To date, there are several groups interested in developing cardiac tissue models that better capture the adult phenotype [1–5]; however, more recently the adaptation of these systems towards hESC [6] and hiPSC [5,7–9] culture has been the focus of the cardiac tissue engineering field. The work presented in this dissertation has been the adaptation of the light-based 3D printing method, μCOP, to produce functioning mouse (chapter 2 and 3) and human (chapter 4) cardiac tissue models, in attempts to extend the fields of 3D bioprinting and cardiac tissue engineering. I determined the optimal printing conditions and materials to encapsulate and help direct NMVCM elongation, designed and characterized a 3D-printed mechanical tester, and investigated the effects of micropatterning on tissue contraction, producing a NMVCM model with high force and adapting this system towards human cells. Furthermore, I developed a higher-throughput system that was able to replicate the inotropic effects of LEVO and OM, never previously shown in 2D culture [10,11]. Lastly, I developed a method of printing a thick cardiac tissue with patterned endothelial cells to aid in promoting host integration. These methods are foundational and can be continuously improved and adapted to further mature the cardiac tissue engineering field.

Practical limitations

As mentioned in the first chapter, every material and every concentration must be optimized before use. Further optimization is required per cell type and cell concentrations greater than 10 million cells per mL. Preliminary work presented in this dissertation looking at how changes in simple 2.5D (2D images projected in a volume)

lines and proximity of patterns to one another may affect the overall print time, μm to pixel ratio, and print "quality." It would be of significant help to the 3D bioprinting community to model, in depth, the printing parameters to consider, when printing GelMA. Another point of consideration is the potential use of a hybrid of synthetic and natural materials to increase the stiffness of low concentration GelMA. For 15% GelMA prints, if not warmed at 37^{o}C, the solution will gel within minutes, from a user stand point this is not ideal when having to print multiple samples and the solution must be constantly heated. This constant heating increases the rate of evaporation and every time the solution is exposed to the atmosphere, there is water loss. This is minimal, but over hours it can become significant. Aliquots of gelled solution should be made to prevent this. However, to potentially keep the material liquid at room temperature, while maintaining the binding moieties of GelMA, one could make synthetic/natural hybrid material to match the stiffness of the scaffolds, while keeping the GelMA solution below 7.5% (gels within 10 minutes). Alternatively, a recent study synthesized GelMA using cold water fish gelatin allowed fabrication of 15% GelMA at room temperature [12]. Although the mechanical properties are significantly lower, this could be of interest to reduce variability for projects.

Looking forward, the *in vitro* models that I have proposed, namely the mm-based GelMA cantilever and the PEGDA microcantilevers, remade for each experiment. A materials system and 3D scaffold that could be robust enough for multiple prints, with no significant degradation of mechanical properties of the cantilevers is ideal. Although it is possible to do most encapsulation studies with one person, the studies performed in this dissertation usually required the aid of a second person. Reducing the overall printing to

just cell encapsulation would greatly reduce labor and could increase scientific throughput. Although reverting to clean room techniques poses its own difficulties, the work presented in this dissertation provides adequate dimensions and mechanical properties to target producing a mechanical tester where microarchitectures can be printed on using μCOP later and reused after enzymatic degradation.

Another major challenge is that 3D-printed tissues are not particularly thick (a few mm's); in spite of this, the protein-based materials pose a great obstacle in light penetration during microscopy, limiting our ability to fully analyze our scaffolds. Cryo- and paraffin sectioning are labor intensive, and it is very challenging to maintain the scaffold structure when sectioning. Recently, the development of CLARITY [13] has greatly improved whole-organ imaging. By fixing and locking proteins in place while removing the cell membrane, researchers are less limited by light penetration. Adapting this technique may be of interest to aid in imaging, perhaps also enzymatically degrading the biomaterials used.

Finally, a major challenge and limitation was cell source. For both hESC-CM and hiPSC-CM batch to batch variability is still a major problem when it comes to 3D printing. As challenging as trying to incorporate and elucidate the effects of encapsulating within specific patterns can be, the variation in differentiation and cell quality makes interpreting results more challenging and increases the number of experiments required to ensure that similar quality cells are being compared.

Future Perspectives

As previously mentioned, variations in human stem cell pluripotency and cell differentiation [14,15] is still a major challenge to overcome as the field progresses. As stem cell differentiation is highly dependent on physical forces, and cell-cell and cell-ECM contact, a potential use of the μCOP system could be prepatterning hESC or hiPSCs prior to differentiation to potentially improve cell-cell communication and initiate directionality earlier on[16]. Combining patterning of stem cells with electrical stimuli [17] and cyclic stretch [18,19] could potentially improve differentiation and maturation as well. Furthermore, μCOP could be utilized to alter mechanical properties via secondary exposure (increase stiffness) or photolabile materials [20–22] (decrease stiffness), and/or selectively remove geometries. Regardless, as there are concerted efforts in academia and industry in developing more robust methods of reverting to pluripotency and differentiation, the limitations of reproduce ability and batch-to-batch variation will hopefully be resolved.

The developed methods within this dissertation have the potential of utilizing current technologies to continue to develop and improve. Beyond mono- and co-culture models, replicating native myocardium in cell composition and distribution should be pursued. Furthermore, there has not been any 3D *in vitro* cardiac mouse disease models to date that can analyze force production at a tissue level. A functional cardiac tissue model that can be cultured over a significant period would be a powerful tool to monitor disease progression and development and aid in exploring how the disease manifests at the tissue level. The mechanisms underlying arrhythmia and other cardiomyopathies in patients are still not well understood, thus implementing various patterning strategies

(encapsulation in various patterns, secondary exposure to stiffen localized areas or produced local reactive oxygen species, patterning of a gradient of cell-types across a scaffold, to name a few) using μCOP may further our understanding of disease mechanisms. Gene editing tools such as transcription activator-like effector nucleases (TALENs) and Clustered Regularly Interspaced Short Pallindromic Repeats- associated protein-9 nuclease (CRISPR-Cas9), a new method of precisely targeting genetic changes in living cells [23], have both recently been implemented to develop models for cardiomyopathies [3,24] and electrophysiological disorders[25]. These TALENs and CRISPR-Cas9 gene editing tools could easily be implemented in cultured cells. The modified cells could be a powerful tool moving forward in validating gene modifiers of disease and could be used for both mouse and human models [26].

Developing an in-well printing system to current standard labware (24 and 96-well plates) will greatly increase throughput. Furthermore, by potentially printing in parallel with multiple DMDs, throughput would increase even further. The push towards high-throughput 3D printing will require advances in imaging technology. In general, with the increase in sample size and the push towards 3D, sensitivity and speed of imaging systems will have to increase, along with the costs of the systems decreasing to make these advances accessible.

The current static culture presented in this dissertation is still unreliable in creating functional vasculature. Pairing 3D-printed tissues with microfluidic devices to induce shear stress on endothelial cells could greatly improve vessel formation [27] and host integration for *in vivo* models. Microfluidic methods could be implemented to further improve the ability of users to pattern heterogenous tissues. By digitally

patterning the infusion of various cells into a “printing chamber”, coupled with the DMD patterning the solution, multicomponent and multicell prints could be realized. As it stands, there are currently newer DMDs that have twice the resolution in x and y, i.e. 3840 x 2160, thus allowing μCOP printing to increase the footprint to cm^2 without the loss of pixel resolution. An array of DMD’s or a method of continuously scanning across a solution could greatly increase the footprint of a 3D cardiac patch towards human scale.

Safety and efficacy will be a major bottleneck in the future both for stem cell usage [28] , for *in* vivo patches and the application of cardiac *in vitro* scaffolds to disease modelling and drug discovery is limited. Significant work is required to refine 3D printing technologies and to continuously validate the efficacy in printed tissues at biochemical to physiological levels. It is my hope that the methods developed in this dissertation may add to the available tools in the pursuit to understand cardiac function, disease progression, and the discovery of new therapies.

References:

[1] W.J. de Lange, L.F. Hegge, A.C. Grimes, C.W. Tong, T.M. Brost, R.L. Moss, et al., Neonatal Mouse-Derived Engineered Cardiac Tissue: A Novel Model System for Studying Genetic Heart Disease, Circ. Res. 109 (2011) 8–19. doi:10.1161/CIRCRESAHA.111.242354.

[2] D. Zhang, I.Y. Shadrin, J. Lam, H.Q. Xian, H.R. Snodgrass, N. Bursac, Tissue-engineered cardiac patch for advanced functional maturation of human ESC-derived cardiomyocytes, Biomaterials. 34 (2013) 5813–5820. doi:10.1016/j.biomaterials.2013.04.026.

[3] J.T. Hinson, A. Chopra, N. Nafissi, W.J. Polacheck, C.C. Benson, S. Swist, et al., HEART DISEASE. Titin mutations in iPS cells define sarcomere insufficiency as a cause of dilated cardiomyopathy., Science. 349 (2015) 982–6. doi:10.1126/science.aaa5458.

[4] S.S. Nunes, J.W. Miklas, J. Liu, R. Aschar-Sobbi, Y. Xiao, B. Zhang, et al., Biowire: a platform for maturation of human pluripotent stem cell–derived cardiomyocytes, Nat. Methods. 10 (2013) 781–787. doi:10.1038/nmeth.2524.

[5] J.U. Lind, T.A. Busbee, A.D. Valentine, F.S. Pasqualini, H. Yuan, M. Yadid, et al., Instrumented cardiac microphysiological devices via multimaterial three-dimensional printing., Nat. Mater. 16 (2016) 303–308. doi:10.1038/nmat4782.

[6] D. Zhang, I.Y. Shadrin, J. Lam, H.-Q. Xian, H.R. Snodgrass, N. Bursac, Tissue-engineered cardiac patch for advanced functional maturation of human ESC-derived cardiomyocytes., Biomaterials. 34 (2013) 5813–20. doi:10.1016/j.biomaterials.2013.04.026.

[7] N. Huebsch, P. Loskill, N. Deveshwar, C.I. Spencer, L.M. Judge, M.A. Mandegar, et al., Miniaturized iPS-Cell-Derived Cardiac Muscles for Physiologically Relevant Drug Response Analyses, Sci. Rep. 6 (2016) 24726. doi:10.1038/srep24726.

[8] L. Gao, M.E. Kupfer, J.P. Jung, L. Yang, P. Zhang, Y. Da Sie, et al., Myocardial tissue engineering with cells derived from human-induced pluripotent stem cells and a native-like, high-resolution, 3-dimensionally printed scaffold, Circ. Res. 120 (2017) 1318–1325. doi:10.1161/CIRCRESAHA.116.310277.

[9] J. Jang, H.J. Park, S.W. Kim, H. Kim, J.Y. Park, S.J. Na, et al., 3D printed complex tissue construct using stem cell-laden decellularized extracellular matrix bioinks for cardiac repair, Biomaterials. 112 (2017) 264–274. doi:10.1016/j.biomaterials.2016.10.026.

[10] L. Butler, C. Cros, K.L. Oldman, A.R. Harmer, A. Pointon, C.E. Pollard, et al., Enhanced characterization of contractility in cardiomyocytes during early drug safety assessment, Toxicol. Sci. 145 (2015) 396–406. doi:10.1093/toxsci/kfv062.

[11] L.C. Liu, B. Dorhout, P. van der Meer, J.R. Teerlink, A.A. Voors, Expert Opinion on Investigational Drugs Omecamtiv mecarbil: a new cardiac myosin activator for the treatment of heart failure Omecamtiv mecarbil: a new cardiac myosin activator for the treatment of heart failure, Expert Opin. Investig. Drugs Expert Opin. Investig. Drugs. 25 (2016). doi:10.1517/13543784.2016.1123248doi.org/10.1517/13543784.2016.1123248.

[12] H.J. Yoon, S.R. Shin, J.M. Cha, S.H. Lee, J.H. Kim, J.T. Do, et al., Cold water fish gelatin methacryloyl hydrogel for tissue engineering application, PLoS One. 11 (2016) e0163902. doi:10.1371/journal.pone.0163902.

[13] K. Chung, K. Deisseroth, CLARITY for mapping the nervous system, Nat. Methods. 10 (2013) 508–513. doi:10.1038/nmeth.2481.

[14] M. Nishizawa, K. Chonabayashi, M. Nomura, A. Tanaka, M. Nakamura, A. Inagaki, et al., Epigenetic Variation between Human Induced Pluripotent Stem Cell Lines Is an Indicator of Differentiation Capacity, Cell Stem Cell. 19 (2016) 341–354. doi:10.1016/j.stem.2016.06.019.

[15] A. Kyttälä, R. Moraghebi, C. Valensisi, J. Kettunen, C. Andrus, K.K. Pasumarthy, et al., Genetic Variability Overrides the Impact of Parental Cell Type and Determines iPSC Differentiation Potential, Stem Cell Reports. 6 (2016) 200–212. doi:10.1016/j.stemcr.2015.12.009.

[16] K.C. Clause, L.J. Liu, K. Tobita, Directed Stem Cell Differentiation: The Role of Physical Forces, Cell Commun. Adhes. 17 (2010) 48–54. doi:10.3109/15419061.2010.492535.

[17] M. Radisic, H. Park, H. Shing, T. Consi, F.J. Schoen, R. Langer, et al., Functional assembly of engineered myocardium by electrical stimulation of cardiac myocytes cultured on scaffolds, Proc. Natl. Acad. Sci. 101 (2004) 18129–18134. doi:10.1073/pnas.0407817101.

[18] C.-R. Wan, S. Chung, R.D. Kamm, Differentiation of Embryonic Stem Cells into Cardiomyocytes in a Compliant Microfluidic System, (2011). doi:10.1007/s10439-011-0275-8.

[19] V.F. Shimko, W.C. Claycomb, Effect of Mechanical Loading on Three-Dimensional Cultures of Embryonic Stem Cell-Derived Cardiomyocytes, Tissue Eng. Part A. 14 (2008) 49–58. doi:10.1089/ten.a.2007.0092.

[20] Y. Luo, M.S. Shoichet, A photolabile hydrogel for guided three-dimensional cell growth and migration, Nat. Mater. 3 (2004) 249–253. doi:10.1038/nmat1092.

[21] C.M. Kirschner, K.S. Anseth, In situ control of cell substrate microtopographies using photolabile hydrogels, Small. 9 (2013) 578–584. doi:10.1002/smll.201201841.

[22] V.X. Truong, F. Li, J.S. Forsythe, Photolabile Hydrogels Responsive to Broad Spectrum Visible Light for Selective Cell Release, ACS Appl. Mater. Interfaces. 9 (2017) 32441–32445. doi:10.1021/acsami.7b11517.

[23] R. Barrangou, C. Fremaux, H. Deveau, M. Richards, P. Boyaval, S. Moineau, et al., CRISPR Provides Acquired Resistance Against Viruses in Prokaryotes, Science (80-.). 315 (2007) 1709–1712. doi:10.1126/science.1138140.

[24] G. Wang, M.L. McCain, L. Yang, A. He, F.S. Pasqualini, A. Agarwal, et al., Modeling the mitochondrial cardiomyopathy of Barth syndrome with induced pluripotent stem cell and heart-on-chip technologies, Nat. Med. 20 (2014) 616–623. doi:10.1038/nm.3545.

[25] Y. Wang, P. Liang, F. Lan, H. Wu, L. Lisowski, M. Gu, et al., Genome Editing of Isogenic Human Induced Pluripotent Stem Cells Recapitulates Long QT Phenotype for Drug Testing, (n.d.). doi:10.1016/j.jacc.2014.04.057.

[26] M.N. Hirt, A. Hansen, T. Eschenhagen, Cardiac tissue engineering: state of the art., Circ. Res. 114 (2014) 354–367. doi:10.1161/CIRCRESAHA.114.300522.

[27] P.A. Galie, D.-H.T. Nguyen, C.K. Choi, D.M. Cohen, P.A. Janmey, C.S. Chen, Fluid shear stress threshold regulates angiogenic sprouting, Proc. Natl. Acad. Sci. 111 (2014) 7968–7973. doi:10.1073/pnas.1310842111.

[28] I. Gutierrez-Aranda, V. Ramos-Mejia, C. Bueno, M. Munoz-Lopez, P.J. Real, A.M. Cia, et al., Human Induced Pluripotent Stem Cells Develop Teratoma More Efficiently and Faster Than Human Embryonic Stem Cells Regardless the Site of Injection, (n.d.). doi:10.1002/stem.471.